Chapter 9
Часть 9

POSTER PRESENTATIONS

ПОСТЕРНЫЕ ДОКЛАДЫ

TABLE of CONTENTS
СОДЕРЖАНИЕ

THE MECHANISM OF FORMATION OF CONDENSED COMBUSTION PRODUCTS AT BURNING OF ALUMINUM-BASED SOLID PROPELLANTS

V.A. Babuk, N.L. Budnyi, and A.A. Nizyaev
Baltic state technical university «VOENMEH»
1, First Krasnoarmeyskaya Str., St.-Petersburg, 190005, Russia
E-mail: Babuk@peterlink.ru

Abstract
The physical mechanisms of formation and evolution of fine and coarse fractions of condensed combustion products are considered at burning aluminum-based solid propellants.

Introduction

Aluminum is a necessary component of high-energetic solid propellants. A peculiarity of its usage is the formation of condensed combustion products (CCP). This is a direct consequence of relatively high temperature of Al_2O_3 evaporation (dissociation). Properties of CCP (sizes, mass fraction, chemical composition, structure) have a significant influence on solid motor operation. These properties determine the losses of specific impulse, slag accumulation rate, regularities of CCP interactions with elements of combustion chamber, optical properties of combustion products, motor operation stability.

In the present work, the physical mechanisms of CCP formation inside a combustion chamber are considered. The work is based on existent experimental data analysis as well as numerical study of a set of the phenomena associated with CCP formation.

In the present time, it is universally recognized that CCP consist of two fractions in sizes. Particles of the fine fraction have a size ~ 1 μm while particles sizes of the coarse fraction can reach ~ 100 μm and even ~ 1000 μm.

Below the physical nature of the both fractions particles formation is consistently considered.

1. The Coarse fraction of CCP

The coarse fraction is represented by *agglomerates* which are the product of enlargement of condensed substances within the surface layer of burning propellant. The agglomerates consist on metal and its oxide as well as can include gaseous cavities and can differ in structure. Within the multiphase flow of combustion products, the evolution of agglomerates is carried out. The evolution represents the set of physical and chemical phenomena caused by the presence of interfacial and interfractional interactions with the participation of agglomerates. As a result of the evolution, a coarse fraction of final CCP is formed. Thus, properties of this fraction are determined by realization of the processes of agglomeration and agglomerates evolution.

1.1. Agglomeration process

The presence of specific structure named the *skeleton layer* (SL) within the surface layer of burning propellant have a fundamental importance for agglomerates formation [1]. The skeleton layer provides the coherency of initial particles of metal within the surface layer and possibility of retention of high-temperature particles on surfaces of burning propellant, i.e. possibility of realization of process of agglomeration.

Properties of SL predetermine the properties of forming agglomerates. The fraction of initial metal in propellant that forms SL corresponds to the fraction of initial metal used to form agglomerates [2]. Physical and chemical transformations of agglomerating metal within SL and on

its surface determine the parameters of chemical composition and structure of formed agglomerates [2]. The agglomerates sizes are determined by the detachment conditions of agglomerating particles from the surface of SL. The detachment conditions are determined by the behavior of liquid particles on wettable surface and depend on properties of SL heterogeneities as well as dynamism of the burning process [3]. In a number of cases, the oxidizer particles appear as heterogeneities which have a determining influence on the agglomerating particles detachment. In these cases, so called *pocket* mechanism of agglomeration takes place. The pocket mechanism was firstly described in works [4, 5]. Variety of SL and agglomerates properties is caused by the variety of propellant formulation factors and burning conditions. The sizes of agglomerates, mass fraction, parameters of chemical composition and structure can significantly differ [6].

1.2. Agglomerates evolution process

This process includes a set of the phenomena [7]: burning of Al in gas-phase mode with formation of *smoke oxide particles* (SOP); chemical interaction between condensed Al and Al_2O_3 resulting in formation of gaseous products; agglomerates structure changes; coagulation of agglomerates and SOP; agglomerates movement within the flow. The main features of these phenomena are the following. In typical conditions of the environment of combustion products of propellant, burning of metal of agglomerates is carried out in *diffusion mode*. Possibility of the interaction between condensed Al and Al_2O_3 and its rate depend on *thermal state* of the agglomerate. Agglomerate structure corresponds to the state of *mechanical equilibrium* of Al and Al_2O_3 drops as well as gaseous cavities.

2. The fine fraction of CCP

The fine fraction is represented by SOP which is formed above the burning propellant surface (no more than 4 mm). Then these particles participate in the evolution process within multiphase flow of combustion products.

2.1. Formation of SOP near the burning propellant surface

There are two mechanisms of the SOP formation [8]. The first mechanism takes place at combustion of non-agglomerated metal. The second mechanism occurs at agglomerating particles burning on the surface of SL. Below the regularities of these phenomena are considered.

The first stage of non-agglomerated metal burning as well as any Al particles burning is heterogeneous burning. This stage is finalized by the boiling of Al. Further, the different scenarios are possible. If the particle maintains its integrity and its size is large enough, the burning process continues in the gas-phase mode. In this case, oxide is formed in gaseous phase and the ions are apparently taking a role of condensation nuclei [9]. The sizes of forming particles are ~ 100–300 nm. On the contrary, if the fragmentation of the particle occurs at its boiling, the prolongation of heterogeneous burning of Al becomes probable. It is connected with a set of factors: intensification of mass- and heat transfer between the particle and environments [10-13], transition from continuous flow mode to the transient and free-molecular mode [14]. For the some intermediate size of the particle, the Al burning occurs in the diffusion-kinetic mode. At this mode, the oxide formation takes place in the gaseous phase as well as on the particle surface. Thus at the burning of non-agglomerated Al, the SOP sizes are largely determined by the processes taking place at Al boiling (presence or absence of a fragmentation and the fragmentation degree).

At the burning of agglomerating particles Al in the gas-phase mode, the SOP formation takes place during heterogeneous condensation. The carbon soot particles act as condensation nuclei [15]. The forming SOP sizes depend on the agglomerating particles size, flow conditions as well as mass fraction and sizes of the carbon soot particles.

2.2. Formation of the SOP at multiphase flow evolution

The two phenomena can be distinguished at SOP evolution [16]. The first phenomenon is the deposition of a coarse fraction of the SOP on the agglomerates. The second phenomenon consists of participation of the SOP in oxide condensation within a gas-phase burning zone of agglomerates. Whereas the first phenomenon leads to reduction in the SOP sizes, the second phenomenon results in the SOP enlargement.

Conclusion

The described mechanism of CCP formation can be used as a basis for creation of mathematical models of considered processes.

References

1. Babuk V.A., Vasilyev V.A., and Sviridov V.V. Formation of Condensed Combustion Products at the Burning Surface of Solid Rocket Propellant. Solid Propellant Chemistry, Combustion, and Motor Interior Ballistics, edited by V. Yang, T. B. Brill, and W. Z. Ren, Vol. 185, Progress in Astronautics and Aeronautics, AIAA, Reston, VA, 2000, pp. 749-776.

2. Babuk V.A., Ivonenko A.N., Nizyaev A.A. Calculation of the characteristics of agglomerates during combustion of high-energy composite solid propellants. Combust., Expl., Shock Waves, 51 (5), 2015, pp. 549–559.

3. Babuk V.A., I. N. Dolotkazin, and V.V. Sviridov. Simulation of Agglomerate Dispersion in Combustion of Aluminized Solid Propellants. Combust., Expl., Shock Waves, 2003, 39 (2), pp. 195–203.

4. Grigor'ev V.G., Kutsenogii K.P., Zarko V.E. Model of Aluminum Agglomeration during the Combustion of a Composite Propellant. Combust., Expl., Shock Waves, 17 (4), 1981, pp. 356–363.

5. Cohen N.S. A Pocket Model for Aluminum Agglomeration in Composite Propellants. AIAA Journal, 21 (5), 1983, pp. 720–725.

6. Babuk V.A. Formulation Factors and Properties of Condensed Combustion Products. Chemical Rocket Propulsion. A Comprehensive Survey of Energetic Materials, Springer, 2017, Chapter 13. pp. 319-341,

7. Babuk V.A., Vasilyev V.A. Model of Aluminium Agglomerate Evolution in Combustion Products of Solid Rocket Propellant, J. Propul. Power, 18 (4), 2002, pp. 814–824.

8. Babuk V.A. Problems in Studying Formation of Smoke Oxide Particles in Combustion of Aluminized Solid Propellants. Combust., Expl., Shock Waves, 43 (1), 2007, pp. 38-45.

9. Vovchuk Ya.I., Poletaev N.I., Florko A.V., I.S. Al'tman, A.N. Zolotko. Synthesis of nanooxides in two-phase laminar flames. Combust., Expl., Shock Waves, 32 (3), 1996, pp. 262–269.

10. Bazyn T., Krier H., Glumac N.. Evidence for the transition from diffusion-limit in aluminum particle combustion. Proceedings of the Combustion Institute, 31, 2007, pp. 2021-2028.

11. Bucher P., Yetter R.A., Dryer F.L. Flame structure measurement of single, isolated aluminum particles burning in air. Twenty-Sixth Symposium (International) on Combustion. The Combustion Institute, 1996, pp. 1899–1908.

12. Sundaram D. S., Puri P., Yang V. A general theory of ignition and combustion of nano- and micron-sized aluminum particles. Combust. Flame, 169, 2016, pp. 94–109.

13. Sundaram D. S., Yang V., Zarko V. E. Combustion of nano aluminum particles (Review). Combust., Expl., Shock Waves, 51 (2), 2015, pp. 173–196.

14. Mohan S., Trunov M.A., Dreizin E.L. On Possibility of vapor-phase combustion for fine aluminum particles. Combust. Flame, 156, 2009, pp. 2213–2216.

15. Babuk V.A., Budnyi N.L. Modeling of Oxide Formation During Burning of Agglomerate Metal. Khimicheskaya Fizika I Mezoskopiya, 17 (1), 2015, pp. 39–50.

16. Babuk V.A., Budnyi N.L. Modeling of Smoke Oxide Particles Evolution in Flow of Combustion Products of Aluminized Solid Propellant. Khimicheskaya Fizika I Mezoskopiya, 19 (1), 2017, pp. 5–19.

EFFECT OF Cr_2O_3 ON BURNING CHARACTERISTICS OF GAS GENERATORS BASED ON AN/MgAl

[1,2]K. Kamunur, [1,2]J.M. Jandosov, [1,2]R.G. Abdulkarimova, [3]Keiichi Hori.
[1,2]Zh.K. Yelemessova, [1,2]Z.A. Mansurov
[1]Al-Farabi Kazakh National University, Almaty, Kazakhstan
[2]Institute of Combustion Problems, Almaty, Kazakhstan
[3]Japan Aerospace Exploration Agency (JAXA), Sagamihara, Japan
e-mail: kamunur.k@mail.ru

Abstract
In this study, the burning characteristics of AN/MgAl-based gas generators with addition of Cr_2O_3 as a burning catalyst were investigated. Addition of Cr_2O_3 increases the burning rate and improves ignition at low pressure and the use of mechanical alloy MgAl as an fuel allowed gas generators to ignite at low temperatures.

Keywords: AN/MgAl-based gas generator, catalytic combustion, burning rate, high-pressure chamber, high speed video recorder.

Introduction

Recently, gas generators based on AN which is used as an oxidizer have gained popularity. Gas generators based on AN have disadvantages such as: low burning rate, slow ignition and low energy. In many investigations, the authors meted that addition of transition metal oxides into the composition of composite nitrogen fuels based on AN improved the characteristics of combustion [1-2]. The use of mechanical alloy MgAl (50/50) as fuel for improvement of burning characteristics of AN-based gas generator results in the improvement of gas generator characteristics and increases flexibility. The melting and ignition points of MgAl alloy are lower than those of pure metals [3]. These properties of MgAl alloy improve the disadvantages of the gas generator on the basis of ammonium nitrate [4-5].

In the study, the burning characteristics of AN/MgAl-based gas generator with addition of Cr_2O_3 under the conditions of catalytic combustion were investigated. The burning rate was determined. The mechanism of catalytic combustion was studied with the help of surface observation.

Experimental

The burning rate of a gas generator was determined by burning of AN/MgAl/Cr_2O_3 in the combustion chamber under pressure. The combustion chamber is filled with nitrogen. Ignition of the samples is initiated with the help of electric current via nichrome threads. The scheme of the process is shown in figure1.

Results and discussion

The burning rates of AN/MgAl/Cr_2O_3 – based gas generators were determined at the values of pressure equal to 1MPa, 3MPa and 5MPa. The mixtures in different mass ratios were prepared with the help of compaction in a press form the diameter of which was equal to 6mm and the height – to

10mm at the pressure of 20MPa. The prepared samples were ignited in the combustion chamber by application of electric current via a spiral. To determine the burning rate, a high speed video recorder PHOTRON of 1000 pictures a second and resolution of 640x488 pixels was used.

Figure2 The effect of metal oxides on burning of gas generator based on AN-70%/MgAl-30%/Cr_2O_3 – 5% in the combustion camera at the pressure of 1MPa, 3MPa and 5MPa.
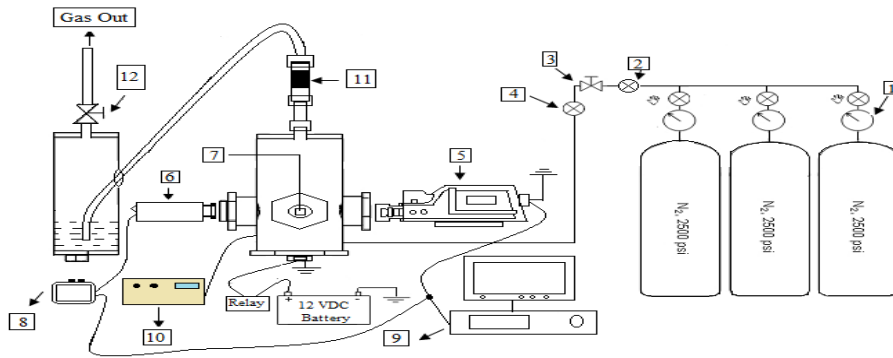
1 – Regulators, 2 – Romote Fill Valve, 3 – Fill Flow Rate Control, 4 – Monometer, 5 – high speed video recorder, 6 – Camera, 7 – light Source, 8 – Screen Monitor, 9 – PC, 10 – Pressure Control system, 11 – filter, 12 – Vent Flow Rate Control

Figure1. The scheme of the combustion camera under pressure

(AN + MgAl + Cr_2O_3, 1MPa, the burning time – 788msec, h = 7.29мм)

(AN + MgAl + Cr_2O_3, 3MPa, the burning time – 1028msec, h = 11.38мм)

(AN + MgAl + Cr_2O_3 , 5MPa, the burning time – 480msec, h = 11.31мм)
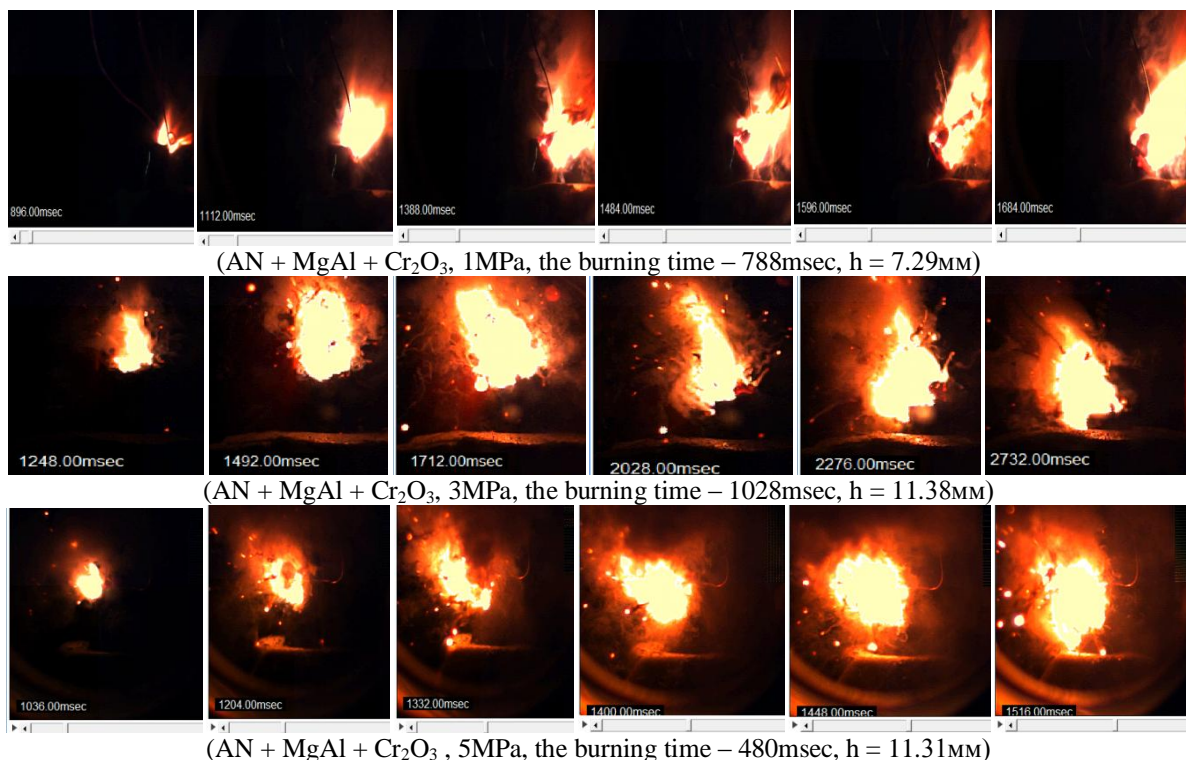
Figure2. The cinegram of AN/MgAl/Cr_2O_3 – based gas generator burning at 1MPa, 3MPa and 5MPa.

It is seen that the burning rate of AN/MgAl/Cr_2O_3 – based gas generator increases linearly with the increase in the pressure in the camera. In comparison with AN/MgAl, AN/MgAl/Cr_2O_3 burnt at low pressures, Cr_2O_3 exerted a catalytic effect on the burning rate by increasing it.

The results of the carried out experiments showed that the burning rate was high and the samples burnt completely. Besides, addition of Cr_2O_3 into the system increased the burning rate and made the burning possible at low values of pressure. The reactions of sample burning are highly exothermic reactions with evolution of heat, light and formation of gas containing substances in a great amount.

Figure3 shows the burning rates of the samples based on AN/MgAl and AN/MgAl/Cr_2O_3 at different pressures of nitrogen atmosphere. Addition of Cr_2O_3 significantly influenced the burning rates and ignition abilities of the systems at low pressure.

1 – AN-70%/MgAl-30%; 2 – AN-70%/MgAl-30%/Cr_2O_3-5%
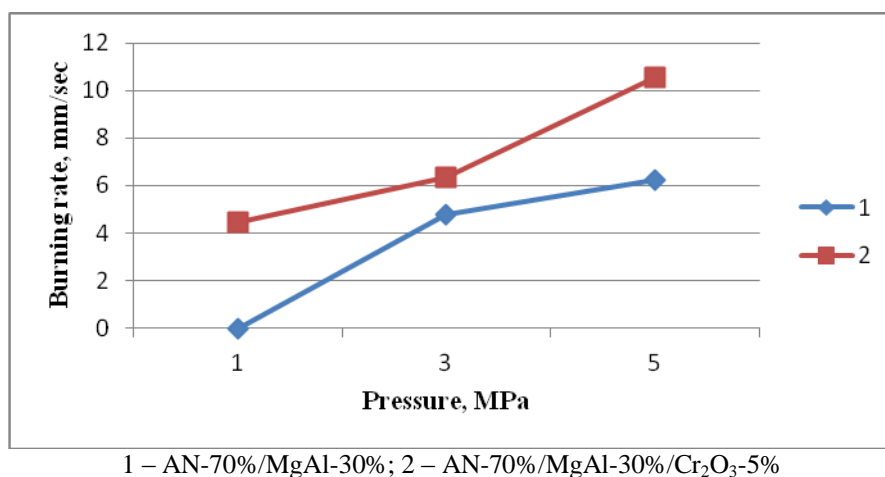
Figure3. The dependence of the burning rate on the pressure of nitrogen

The analysis of the obtained results showed that the use of metal alloys as fuel, when compared to pure metals, has a number of advantages: high energy, low ignition temperature and low density. Therefore, the used of gas generators on the basis of ammonium nitrate is considered to be promising. However, this investigation was carried out at low values of pressure. Further investigations should be carried out at high values of pressure and at different ratios of metal alloy and ammonium nitrate.

Conclusion

According to the results of the carried out investigations, the experiment were performed which showed that in the combustion chamber at nitrogen pressure equal to 1MPa, 3MPa and 5MPa, addition of chromium oxide into AN/MgAl– based gas generator allowed the gas generator on the basis of AN/MgAl to ignite at low pressure and led to the liner increase of the burning rate with the increase in the pressure of nitrogen up to 10.5mm/sec addition of Cr2O3 into the composition of gas generator based on AN/MgAl had a high catalytic action.

References

1. Makoto Kohga &Tomoki Naya, "Thermal Decomposition Behaviors and Burning Characteristics of AN/RDX-Based Composite Propellants Supplemented with MnO_2 and Fe_2O_3", Journal of Energetic Materials, Volume33, 2015 – Issue 4, pp. 288-304.

2. H. Murata, Y. Azuma, T. Tohara et al., "The effect of magnalium(Mg-Al alloy) on combustion characteristics of ammonium nitrate-based solid propellant," Science and Technology of Energetic Materials, vol. 61, no. 2, pp. 58–66, 2000.

3. Shoshin, Y.L., R.S. Mudryy, and E.L. Dreizin, Preparation and characterization of energetic Al-Mg mechanical alloy powders. Combustion and Flame, 2002. 128(3): p. 259-269.

4. Камунур К., Жандосов Ж.М., Абдулкаримова Р.Г., Кейщй Хори, Атаманов М.К., Мансуров З.А., Влияние Cr_2O_3 на характеристики горения композитных твердых газогенераторна основе AN/MgAl // Горение и плазмохимия,2016, том 14, №3, с.189-194.

5. Hiroto Habu and Keiichi Hori, "The burning rate characteristics of magnalium (Mg/Al)-AP based solid propellant", Journal Science and Technology of Energetic Materials, Vol.67, №.6, (2006), pp. 187-192.

DEVELOPMENT AND PRODUCTION OF GRANULAR CARBON SORBENTS FOR SORPTION OF TOXIC GASES

M.R.Kerimkulova[1], A.R.Kerimkulova [1,2], S.Azat[1,2], Z.A.Mansurov[1,2], I.S. Berezovskaya[3], L. Fernandez Velasco[3], P.Lodewyckx[3]

[1]Institute of combustion problems, Almaty, Kazakhstan
[2]al-Farabi Kazakh National University, Almaty, Kazakhstan
[3]Royal military Academy, Brussels, Belgium
E-mail: biomak111@mail.ru

Annotation

As used lignosulfonate industrial waste, which is obtained in the processing timber. The selected optimum granulation regime in different proportions of the binder and flour rice husks. As a result of the research, a technology for obtaining granular sorbents was developed. It was found that the ratio of rice husk (RH) to binder is 3: 1, the carbonization temperature 800^0C. A study of the microstructure of the obtained samples showed that the binder has a dense surface and has only a small number of pores of round shape, mostly of large size.

Keywords: rice husks, carbonization

Introduction

The problem of air pollution - one of the greatest global challenges faced by humanity. Risk of air pollution - not only in the fact that clean air fall harmful substances harmful to living organisms, but also causes contamination of the Earth's climate change. Nevertheless, humanity continues to burn fossil fuels and destroying forests. Air pollution occurs as a result of other human activities. Fuel combustion in thermal power plants is accompanied by the release of sulfur dioxide. With car exhaust gases emitted into the atmosphere of nitrogen oxides [1,2].

At the present stage, for the majority of industrial cleaning and suction air emissions of harmful substances is one of the basic measures to protect the air basin. A feature of most industrial emissions is to have them in addition to solid and liquid particles (dust, fumes and mists) a large amount of harmful gaseous components. Clean gas flows from such impurities and requires specific equipment corresponding theoretical knowledge for the development of gas purification technology. Among the methods of neutralization of industrial emissions increasingly becomes important adsorption way to almost completely remove the impurities from gas streams. In use solid adsorbents as high surface area materials formed into pellets (spheres, tablets, cylinders, etc.), or are in finely divided form [3].

In this connection, the production and consumption of the carbon materials has steadily increased. In particular, the global consumption of carbon materials is about 1.1 million tons per year and continues to grow at 9% per year [4]. Thus a major amount of activated carbon (80-85%) is produced from non-renewable resources. Large range of carbon materials obtained on the basis of large-tonnage waste of chemical and mechanical processing of wood: sawdust, bark, logging waste and technical lignins [5].

Experimental part
1. Development of synthesis technology and production of granular sorption materials
In this work, a synthesis technology and the preparation of granular sorption materials from waste products by extrusion, granulation on a screw granulator was developed. As a waste, lignosulfonate (LS) and rice husk flour were used.

To prepare granular carbon sorbents, the raw materials were prepared. To do this, rice husks were grinded on the planetary mill "Activator 4M", when using metal balls with a diameter of 5 mm, in an amount of 300 pieces; The grinding time is 3 minutes. Further, at a ratio of 2: 1, 3: 1 and 4: 1, with the addition of water (40 ml per 100 g) from flour and lignosulfonate, a plastic mass was obtained. Further, from which granules were obtained using a screw granulator. The resulting granules were dried at room temperature for 6-12 hours. The carbonization of the samples was carried out under strictly controlled isothermal conditions, in a rotating reactor in an inert gas-argon medium, which was continuously supplied to the reactor at a rate of 50 cm^3/min.
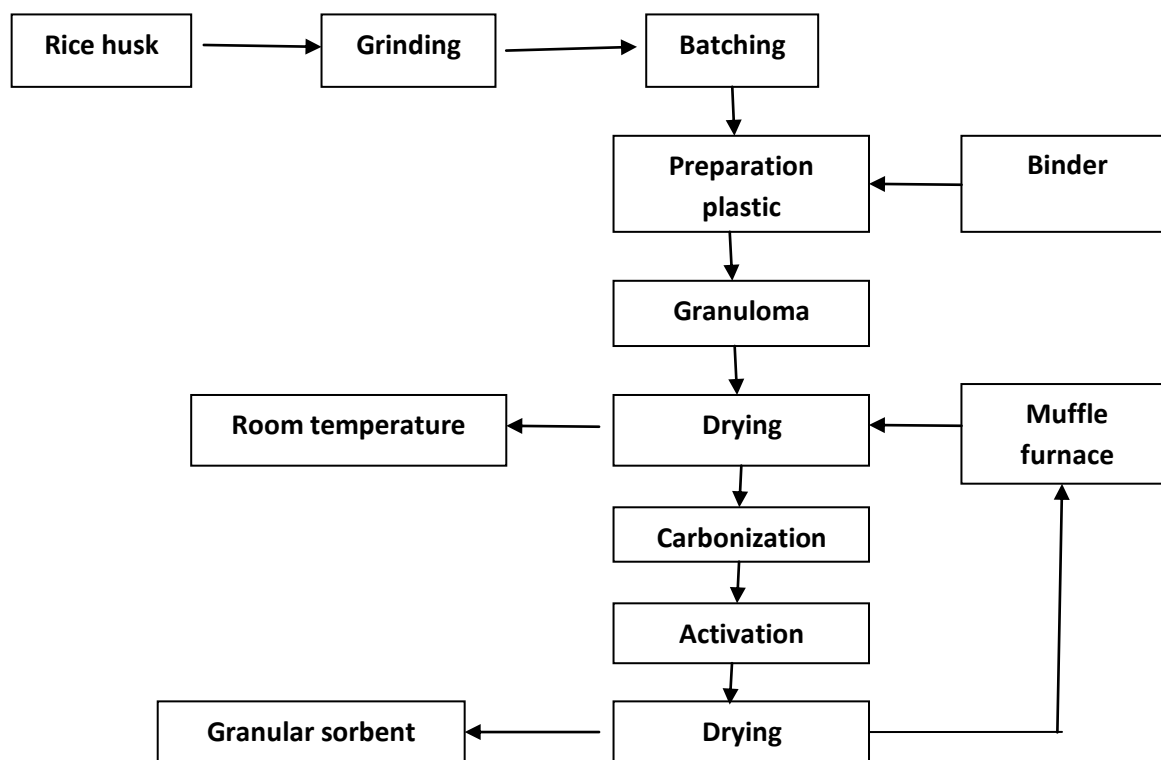
Figure 1 - Scheme for the production of granular carbon sorbents

Carbonization was carried out at temperatures of 750 and 800 °C. In order to improve the sorption characteristics, the granules obtained were activated using chemical reagents. The scheme of the process for obtaining granular sorbents is shown in Figure 1.

The influence of the amount of binder on the yield and the properties of the sorbents obtained was investigated in the work. For the study, samples were prepared in which the ratio of the binder and flour of the RH was changed in accordance with the data given in Table 1.

According to the data obtained on the Sorbtometer-M analyzer, the specific surface area of the resulting samples after activation was in the range 146-883 m^2/g.

To determine the optimum ratio of sorbent and binder in the composition of the final product, the values of the yield and the specific surface of the samples were compared. From Table 1 it follows that the ratio of RH and binder is 3: 1, the carbonization temperature is 800 ^{0}C. The general view of the obtained carbon sorbent granules is shown in Fig. 2.

Table 1 - Characteristics of the obtained granular samples

Ratio RH/ LS	t, °C	m_0, g	m_1,g	m_2,g	Exit, %	S^1s, m^2/g	S^2 s, m^2/g	Volume porosity, cm^3/g	Sorption activity by methylene blue mg/g
67:33 (2:1)	800 (1h30min)	58,12	11,48/10	4,35	37,9	198	684	0,272	368
67:33 (2:1)	750 (1h30min)	40,39	12,31/11,6	7,03	57,1	78	146	0,065	363
80:20 (4:1)	800 (1h30min)	25,81	8,25	4,33	52,5	204	336	0,147	365
75:25 (3:1)	800 (1h30min)	45,56	12,11	6,78	55,9	205	883	0,337	373
75:25 (3:1)	800 (1h50min)	51,55	12,73	5,14	40,4	239	803	0,344	373

Figure 2 - Granular carbon sorbent from RH and lignosulfonate

As a result of the research, the technology of obtaining granular sorbents was developed. It was found that the ratio of RH to binder 3: 1 is optimal, the carbonation temperature is 800 ^{0}C.

2. Investigation of the physico-chemical characteristics of the obtained granulated sorption materials

The physico-chemical characteristics of the obtained granular sorption materials were studied by electron microscopy, low-temperature adsorption of nitrogen, adsorption of carbon dioxide.

To determine the pore size, the density functional method DFT was used. The BET method was used to determine the specific surface area of the adsorbents.

The morphology and surface relief of the investigated samples of the carbon sorbent was studied by electron microscopy using the electron microscope JSM-6510 LA. To obtain contrasting electronic microimages, the study surfaces were conducted at a voltage of 15-20 kV and in a current strength of 10-30 mA.

It can be seen from the obtained micrographs that the bonding material has a dense surface and has only a small number of pores of round shape, mostly of large size (Figure 3A). It can be seen from Fig. 3B that the starting material (RH) is firmly fixed in the matrix of the binder, lignosulfonate. Further, the activation of these pellets from rice husk and lignosulfonate promotes

the formation of more pores of small size and the development of the sponge structure of the sorbents.

The device used in this study made it possible to work on the elemental composition of the granular sorbent before and after activation. The research was carried out on a modern JED-2300 EDS energy-dispersive spectrometer by JEOL, Japan, which is an additional device for the scanning electron microscope type JSM-6510 LA, the same firm. These studies are presented in Figure 4.

A)binder material – lignosulfonate

A) granules from RH and LS before carbonization

B) granules after activation
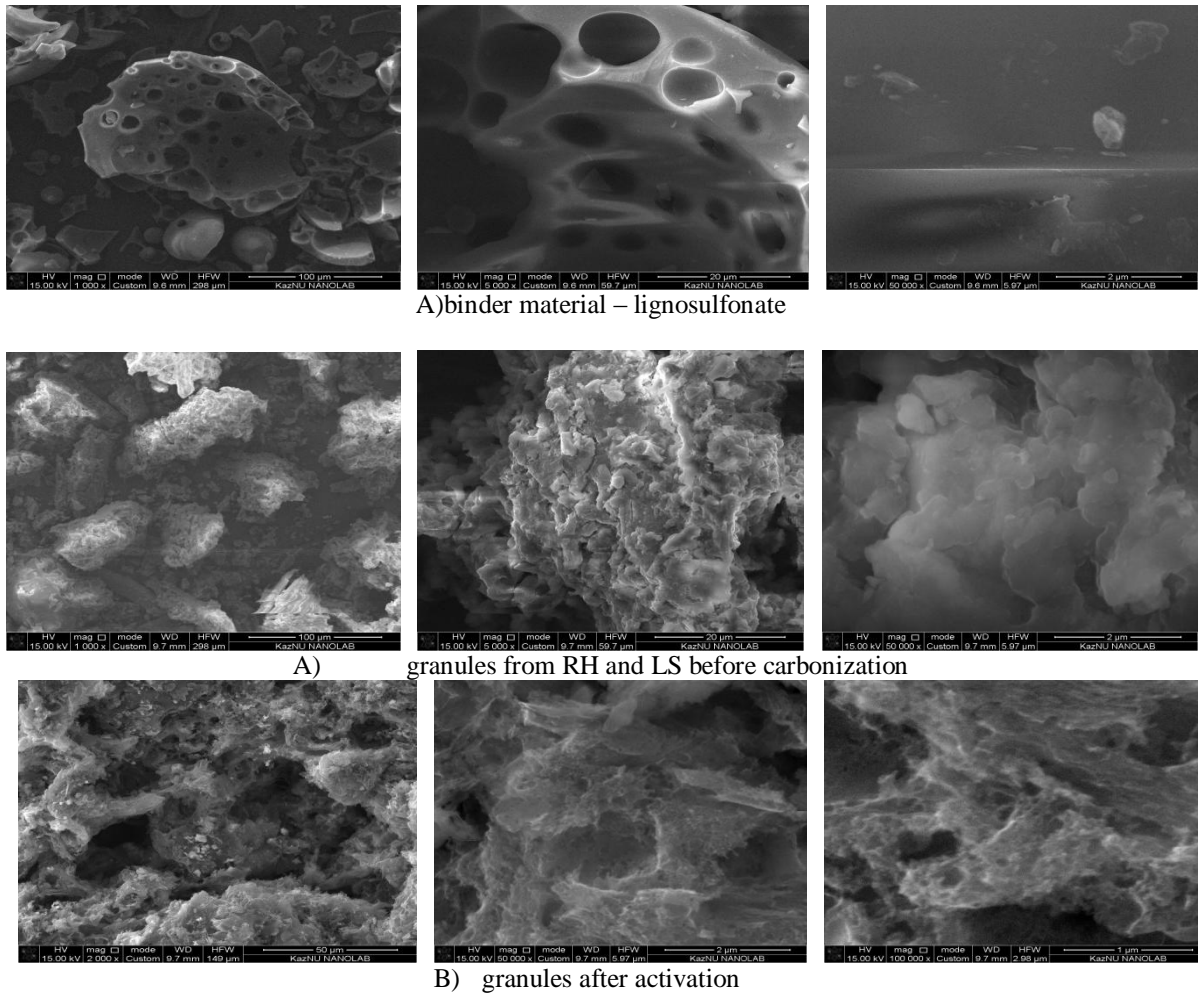
Figure 3 - Electronic micrographs
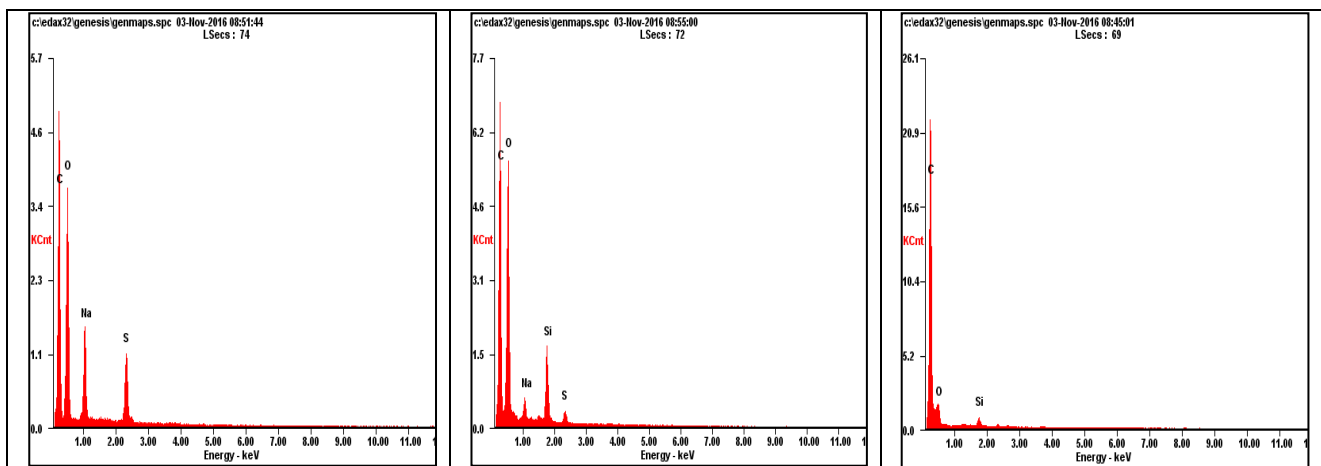
Element	Wt%	At%
CK	55.19	63.57
OK	38.28	33.10
NaK	1.47	0.89
SiK	4.20	2.07
SK	0.87	0.37
Matrix	Correction	ZAF

Element	Wt%	At%
CK	56.00	65.16
OK	33.35	29.14
NaK	6.13	3.73
SK	4.53	1.97
Matrix	Correction	ZAF

Element	Wt%	At%
CK	86.96	90.23
OK	11.87	9.25
SiK	1.17	0.52
Matrix	Correction	ZAF

A	B	C

A) binder material - lignosulfonate; B) granules from RH and LS before carbonization; C) granules after activation

Figure 4 - Elemental composition

As can be seen from figure 4 (A, B, C), as a result of activation, there is a significant decrease in the amount of oxygen. At the same time, there is a simultaneous decrease in the content of sodium and sulfur to zero, which volatilize during the carbonization process, which has a beneficial effect on the quality of the carbonized material. The analysis made it possible to show that an increase in the carbon content of the activated samples occurs as compared to the initial samples of granular sorbents.

Conclusion

- As a result of the research, the technology for obtaining granular sorbents was developed. It was found that the ratio of RH to binder 3: 1 is optimal, the carbonation temperature is 800 ^{0}C.

- Investigation of the microstructure of the obtained samples showed that the binder material has a dense surface and has only a small number of pores of round shape, mainly of large size, and the starting material (PI) is firmly fixed in the matrix of the binder, lignosulfonate. And the further activation of these pellets from rice husk and lignosulfonate contributed to the formation of more small pores and the development of the spongy structure of the sorbents.

References

1. Faisal I. Khan., Aloke Kr. Ghoshal. Removal of Volatile Organic Compounds from polluted air // Journal of Loss Prevention in the Process Industries. -2000. - Vol. 13. - P. 527–545.

2. Gang Wang, Baojuan Dou, Zhongshen Zhang, Junhui Wang, Haier Liu, Zhengping Hao. Adsorption of benzene, cyclohexane and hexane on ordered mesoporous carbon // Journal of Environmental Sciences. - 2015. - Vol. 30 - P. 65–73.

3. Mambetova M.Zh., Kerimkulova A.R., Mansurov Z.A., Berezovskaya I.S. Ochistka i sorbsiya toksichnyh gasov// Himichesky zhurnal Kazahstana – 3(55)2016 – P.162-172.

4. Gang Wang, Baojuan Dou, Zhongshen Zhang, Junhui Wang, Haier Liu, Zhengping Hao. Adsorption of benzene, cyclohexane and hexane on ordered mesoporous carbon // Journal of Environmental Sciences. - 2015. - Vol. 30 - P. 65–73.

5. Azat S., Rosa Busquets, Pavlenko V.V., Kerimkulova A.R., Raymond L.D., Whitby, Mansurov Z.A. Applications of activated carbon sorbents based on greek walnut. Applied Mechanics and Materials vol.467(2014) pp.49-51.

EXPERIMENTAL INVESTIGATION OF INFLUENCE OF WATER MIST ON BLAST OVERPRESSURE IN SHOCK TUBE

E. Mataradze, N. Chikhradze, I. Akhvlediani, N. Bochorishvili, Z. Malvenisvili
G. Tsulukidze Mining Institute, 7, E. Mindeli Str., Tbilisi 0186, Georgia

Abstract
Explosion protection technologies are based on the formation of a shock wave mitigation barrier between the protection site and the explosion site. Contemporary protective systems use water mist as an extinguishing barrier. To achieve high effectiveness of the protective system, proper selection of water mist characteristics is important. The main factors defining shock wave attenuation in water mist include droplet size distribution, water concentration in the mist, droplet velocity and geometric properties of mist. This paper examines the process of attenuation of shock waves in mist with droplets ranging from 25 to 360 microns under different conditions of water mist location: Blast Chamber-Water Mist-Air and Blast Chamber-Air-Water Mist-Air. Experiments were conducted at the Mining Institute with the use of a shock tube to study the processes of explosion suppression by a water mist barrier.
Keywords: Blast overpressures; Water mist, Shock tube; Blast energy attenuation.

1. Introduction

Blast suppression mechanisms using water mist have been addressed by G. Thomas, Van Winderden, K. Kailasanath, and R. Ananth et al [1,2,3,4]. It has been noted that water mist with fine sprays is efficient for the mitigation of explosions. Research has shown that shock energy extraction by water mist takes place during the process of aerodynamic droplet break-up and vaporization of child droplets. The main purpose of the existing studies is to determine the effect of droplet size distribution and concentration of water on blast overpressure attenuation in water mist. Significant knowledge has been accumulated in this area, however there still are some gaps that need to be addressed in order to improve the design of protective devices. More specifically, the effect of the water barrier location on the suppression impact remains understudied.

2. Experimental setup

A shock tube was designed to study the effects of water concentration, water drop diameter, location and length of the water mist on blast attenuation. It enables to study the effects of solid explosive, fuel-air and gas explosions. The shock tube consists of a blast chamber, a tube, a system for the dosed supply of fuel and water, sensors, data recording equipment, and a process control module. The shock tube is located in a tunnel (fig. 1), while the data recording equipment and the control module are located in the monitoring room placed at a 6m distance from the tunnel entry. The following are the basic characteristics of the blast chamber and separate tubes: Diameter of the blast chamber and tubes – 50 cm; Blast chamber length – 50 cm; Wall thickness – 8 mm, Number of separate tubes – 10; Total length of the shock tube – 10.5 m.

The shock tube has a system for the dosed supply of water, which is composed of pumps, pipelines, electric valves and nozzles, and other hydraulic elements needed for water mist creation. Twelve nozzles model BETE P120 are fixed in each of the first and second tube segments (i.e. twenty-four in total) after the blast chamber.

3. Results of the experiments

The objective of the study was to investigate shock wave attenuation in water mist in the following conditions:

- Explosive charge location - blast chamber of the shock tube;
- Type of explosive and mass of charge: hexogen, 5 gram
- Droplet size distribution in mist: 25-360 μm;
- Flow rate: 0.9 L/s;
- Length of mist in the shock tube section: 1m
- Concentration of water in mist: $4.5 \ L \cdot m^{-3} \cdot sec^{-1}$

In different cycles of experiments water mist was generated in section #1 (Fig. 1-a, Blast Chamber-Water Mist-Air) and section #2 (Fig.1-b, Blast Chamber-Air-Water Mist-Air).
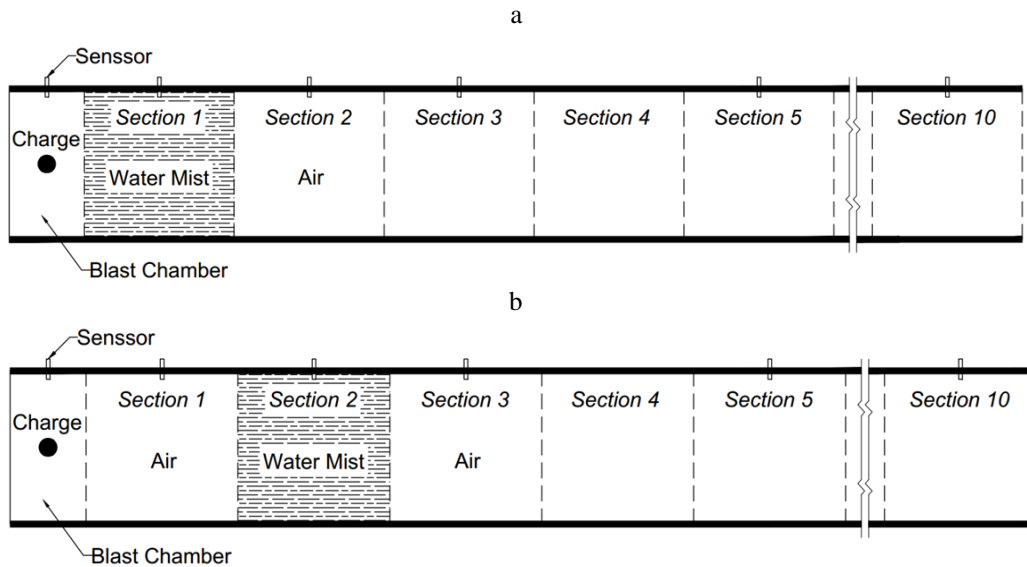
Fig. 1. Scheme of the experiments. a) Blast Chamber-Water Mist in section #1-Air, b) Blast Chamber-Water Mist in section #2 -Air

Attenuation of shock waves in mist was estimated using overpressure reduction coefficient:
$K = (\Delta P_a - \Delta P_m)/ \Delta P_a$. Where ΔP_a and ΔPm is overpressure without mist and with mistat the same distance from the charge. The values of overpressures measured during the experiments without mist and with mist are given in Fig. 2.
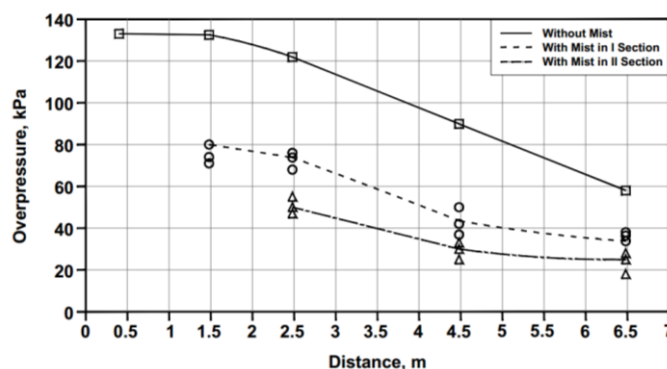
Fig. 2. Dependence of maximum overpressures on the water mist location

5. Conclusions

Shock wave overpressure reduction coefficient K was studied in the shock tube under two different locations of water mist: a) when water mist is created in direct contact with blast chamber and b) the blast chamber and the mist are separated by air space. It is established that in conditions

when the air space distance between the blast chamber and the mist is 1 meter, overpressure reduction coefficient is 1,5-1,6 times higher than in conditions when water mist is created in direct contact with blast chamber. This can be explained by different mechanisms of energy suppression near the charge zone where overpressures develop under the effect of gaseous products of explosion and in the zone where shock waves are generated.

Acknowledgements

References

[1] Thomas G.O. On the Conditions Required for Explosion Mitigation by Water Sprays. Trans I Chem E: Part B - Process Safety and Environmental Protection Vol. 78 pp. 339-354

[2] Van Wingerden, K., Mitigation of Gas Explosions Using Water Deluge, Process Safety Progress, v. 19, pp. 173-178, 2000.

[3] Kailasanath K. and Schwer D. Shock Attenuation Using Water Mists. Naval Research Laboratory, Code 6410. Washington, DC 20375 (2007)

[4] Ananth R., Ladouceur H., Willauer H., Farley J. and Williams F. Effect of Water Mist on a Confined Blast (2009). www.nfpa.org/assets/files//PDF/Foundation%20proceedings/Ananth.pdf

GROWTH OF PZT THIN FILMS ON NI AND SI SUBSTRATE BY PLD

Mereke A., Umirzakov A., Beisenov R., Rakhmetov B., Muratov D.
LLP «Institute of Physics and Technology», 11 Ibrahimov str., FEZ PIT "Alatau", Almaty, Kazakhstan

Abstract
This paper presents a technique for obtaining a target of lead zirconate titanate (PZT) at a hot pressing plant and its subsequent deposition in a pulsed laser deposition apparatus (PLD) in an O_2 atmosphere at temperatures from 500°C to 750°C, 370 mJ UV laser energy in 60 minutes to obtain thin PZT films on Si100 and Ni substrate. The crystal structure of PZT films studied by XRD. Surface morphology grown films studied by AFM and SEM microscopy.

Introduction

Lead zirconate titanate compounds (PZT) are one of the most commonly used ferroelectric materials for research and industrial applications. Piezoelectric properties of PZT also make this material a potential candidate for a variety of MEMS applications. High residual polarization and dielectric constant, in addition to electro-optical and pyroelectric effects, allow using a variety of applications for materials based on PZT. PZT films also recently attracted a lot of attention in applications of devices when integrating with semiconductors. These applications require the deposition of high-quality PZT films on available semiconductor substrates. The various methods used to precipitate PZT include Sol-gel, Ink Jet Printing, Sputtering, Chemical Vapor Deposition (CVD), and Pulsed Laser Deposition (PLD). PLD is a universal deposition method that allows economical deposition of high-quality thin films from a variety of complex multicomponent oxide compounds that include PZT. PLD is based on the assumption of the evaporation of the target material in the plasma plume and its stoichiometric transfer to the substrate.

Experimental

The PZT target made by mixing grinding in a ball mill «SPEX8000» and further pressing in a hot-pressing plant at a temperature of 1500^0C for 4 hours powders PbO_2 and ZrO_2 TiO_2 with a purity of 99.99% in the ratio.

The obtained PZT ceramic target used to deposit PZT films on Si100 and Ni substrates in a pulsed laser deposition (PLD) setup. As a source of laser radiation applied excimer laser Lambda Physik KrF with $\lambda = 248$ nm and pulse frequency about 5-7 Hz. The main variable parameter during deposition was the heating temperature of the substrate. During deposition O_2 gas into the chamber 150 cm3/min flow. The pressure in a chamber with oxygen of 10^{-4} mTorr, an energy density of 370 mJ, and a deposition time of 60 minutes were constant. The target holder is rotatable by an electric drive for uniform deposition.

The crystal structure of synthesized PZT films was investigated by using X-ray diffractometer (XRD Dron-6). The surface morphology of the films were examined by atomic force microscopy AFM company «Solver M» and a scanning electron microscope «JEOL» company.

Results and discussions

Figure 1 shows an XRD film deposited on a nickel substrate using PLD technology. The structure of the PZT films at different deposition temperatures has the same polycrystalline structure with a peak value of 31.3 corresponding to the (110) plane and one more peak at 44.4, which corresponds to the (200) planes for all films. It was found that the interplanar distance corresponding to the highest peak is 2.8904 Å. Lattice constant of PZT films was calculated as 4.0876 Å, which is close to the corresponding bulk value (4.054 Å), indicating the presence of a minimum interfacial tension in the deposited film.
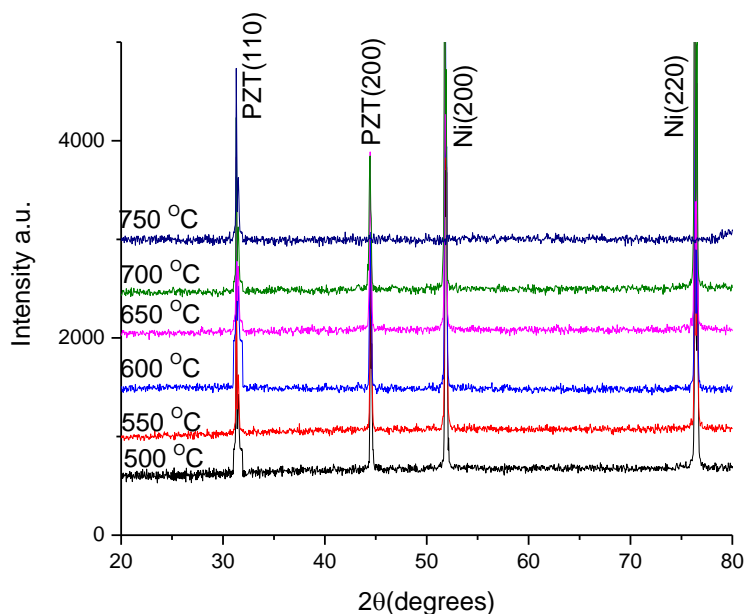
Figure 1 XRD pattern of the PZT thin film coated on and Ni substrate

Figure 2 shows the XRD of a PZT film deposited on a silicon substrate.From the figure it can also be concluded that the sample is a polycrystalline structure also with a peak value of 34.95, which corresponds to the plane (110), and another peak at 49.65 that corresponds to the plane (200).
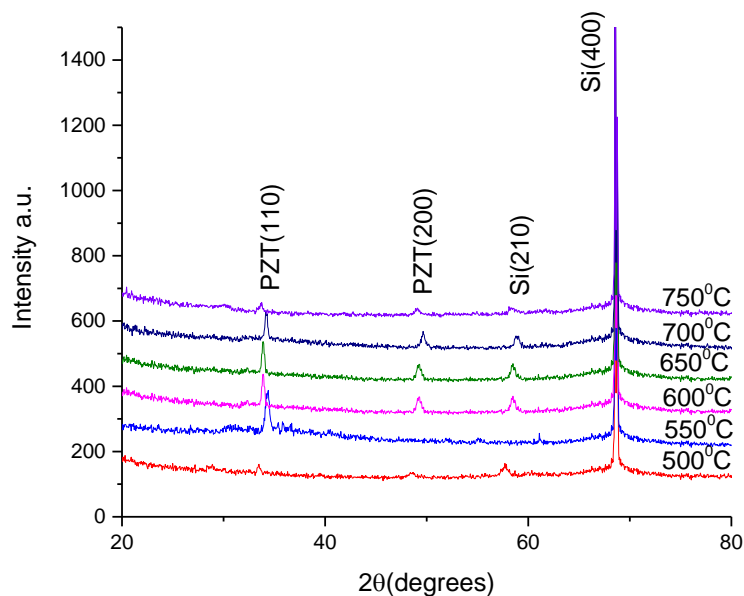
Figure 2 XRD pattern of the PZT thin film coated on and Si substrate

Figure 3 shows the morphology of the PZT surface deposited on a Si (100) substrate at temperatures of 500°C (a) and 750°C (b), 370 mJ laser energy, 7Hz frequency and 60min deposition time. Scanning was carried out in the region 1x1 μm. The surface relief shows the formation of semicircular spherical crystallites with an average diameter of 100 to 200nm. The maximum height of crystallites does not exceed 6 nm. In general, the surface is rather monotonous with sufficiently oriented formations. When the temperature is raised to 750°C, at the same time and energy parameters of the laser, smaller crystallite formations with a diameter of 20 to 80nm are observed. However, the structure of the formations has a more oriented structure with sharp peaks. The height of the crystallites is 30nm.
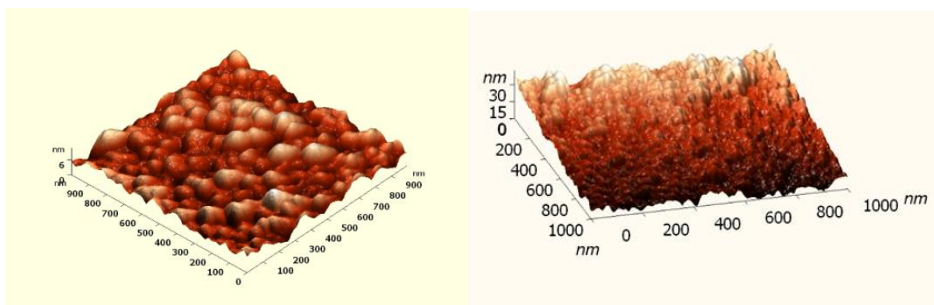
Figure 3 - Atomic force microscopy of the surface of a PZT film deposited on a Si (100) substrate at temperatures of 500 ° C (a) and 750 ° C (b), a laser energy of 370 mJ and a frequency of 7 Hz

Figure 4 shows the morphology of the PZT surface deposited on Ni substrate at temperatures of 500°C (a) and 750°C (b), laser energy 370 mJ, frequency 7 Hz and deposition time 60 min. The morphology of the PZT films deposited on the Ni substrate showed the formation of cone-like crystals with a rather monotonous and sufficiently oriented structure. The maximum crystal height at 500°C does not exceed 30 nm, with an average diameter of up to 200 nm. With an increase in the deposition temperature to 750°C, peaks of up to 10 nm and a diameter of up to 80 nm are observed to decrease. However, the structure of the formations has a more oriented structure.
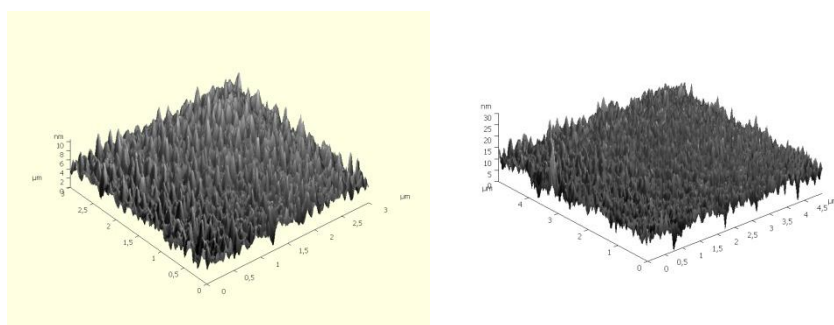
Figure 4 - Atomic force microscopy of the surface of a PZT film deposited on a Ni substrate at temperatures of 500 ° C (a) and 750 ° C (b), laser energy 370 mJ and a frequency of 7 Hz
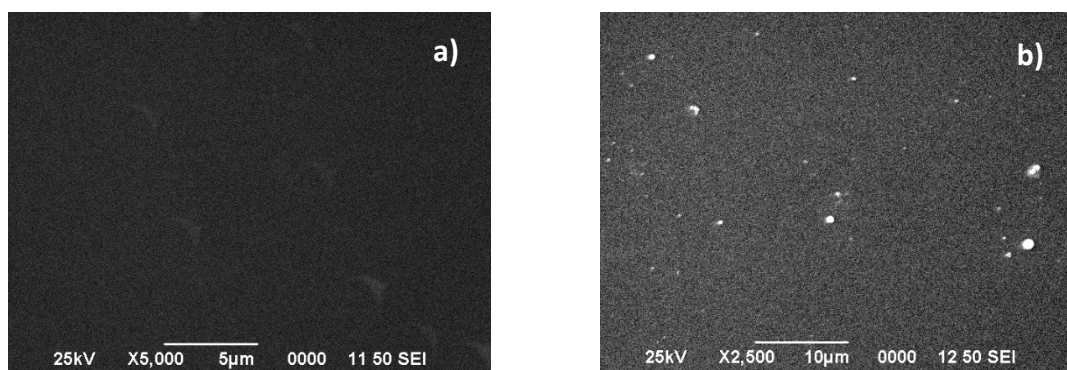
Figure 4-SEM image of the surface of PZT films deposited at 600 ° C
and energies (a) 370 mJ and (b) 600 mJ

From the SEM analysis of Figure 4, scanning the surface of deposited films, it was established that deposition with a lower energy of the laser forms a more uniform surface without contamination.

Conclusion

In the course of the work, thin PZT films were obtained on Ni and Si (100) substrates at different deposition temperatures. Precipitation was carried out by feeding O2 gas into a chamber of 150 cm3 / min. The pressure in a chamber with oxygen of 10-4 mTorr, an energy density of 370 mJ, and a deposition time of 60 minutes were constants. Studies of the crystal structure of the films and their morphology have been carried out, it has been found that the structure of the films is polycrystalline with a peak value of 31.3 corresponding to the (110) plane and another peak at 44.4, which corresponds to the (200) planes for all Si films and a peak value of 34.95 which corresponds to the (110) plane and another peak at 49.65 which corresponds to the (200) Ni plane. That is close to the corresponding volumetric value indicating a minimal interfacial tension in the deposited film.

The morphology of the films showed that the films have a structure with sufficiently monotonous and oriented formations with increasing temperature, a decrease in the dimensions of the peaks and diameters indicating a more oriented structure is observed.

The results obtained will subsequently be used to develop thin-film photocatalysts for the decomposition of water.

References

1. Javad R. Gatabia, Shafiqur Rahmana , Ana Amarob, Taylor Nashb, Juan Rojas-Ramirezb, R.K. Pandeyb, Ravi Droopadb, "Tuning electrical properties of PZT film deposited by Pulsed Laser Deposition" // Ceramics International 43 (2017) 6008–6012

2. Congbing Tana, Jinbin Wanga, Xiangli Zhonga, Jie Jianga, Xiong Zhanga, Yanhuai Dingd, Switchable photoelectrochemical response controlled by ferroelectric polarization in (101)-oriented Pb(Zr0.2Ti0.8)O3 thin film//, Materials & Design 129 (2017) 186–191

3. T. Patel, H. Khassaf, S. Vijayan, N. Bassiri-Gharb, M. Aindow, S.P. Alpay, R.J. Hebert, Metalorganic solution deposition of lead zirconate titanate films onto an additively manufactured Ni-based superalloy//, Acta Materialia 122 (2017) 352-358

4. Hwang D.W., Kim H.G., Kim J., Cha K.Y., Kim Y.G., Lee J.S. Photocatalytic Water Splitting over Highly Donor-Doped (110) Layered Perovskites // J. Catal. -2000. -Vol. P. 193.

5. Javad Gatabi, Kevin Lyon, Shafiqur Rahman, Manuel Caro, Juan Rojas-Ramirez, Joelson Cott-Garcia, Ravi Droopad, Byounghak Lee, "Functional materials integrated on III–V semiconductors", Microelectronics. Eng. 147 (2015) 117–121.

6. R. Wang, H. Kokawa, R. Maeda, "Epitaxial PZT Films Deposited by Pulsed Laser Deposition for MEMS Application", DTIP 2006, Stresa, Lago Maggiore, Italy, 2006.

7. I. Pintilie, L. Trinca, L. Trupina, I. Pasuk, L. Pintilie, Relation between domain structure and pyroelectric response in as-grown epitaxial Pb(Zr0.2Ti0.8)O3 thin films on substrates with different resistivity, Materials Research Bulletin, Volume 93,September 2017,Pages 201-207

8. S.A. Kukushkin, I.Yu, Tentilova, I.P. Pronin, "Mechanism of phase transformation of the pyrochlore phase into the perovskite phase in zirconate-lead titanate films on silicon substrates" // Solid-state physics, 2012, vol. 54, № 3.

SILUMIN MODIFIER EFFECT IN THE AL-B-O SYSTEM

V. Nekrasov[1], G. Ksandopulo[1], A. Baideldinova[1], L. Mukhina[1], Y. Ryabikin[2], Z. Azizov[1]
[1]Institute of Combustion Problems, Kazakhstan, Almaty
[2]Institutr of Nuclear physics Almaty, Kazakhstan
milabrega@yandex.ru

The goal of this study is testing of a ceramic material synthesized in the Al-B-O system in the course of the SHS-process as a powder modifier for silumin casting.

Introduction
Most of the up-to-date equipment currently used to manufacture parts of the internal combustion engines (ICE) is based on wide application of silumins. Their key advantages are small density, high foundry properties, cheap cost, as well as practically unlimited resource supply.

The silumin thermomechanical properties highly depend on a cast alloy structure, primarily on the size and morphology of its structural components.

The process of changing alloy's morphology and crushing of its structural components both at the macro- and microlevel is called modification.

Nowadays there exist numerous different ways of such modification [1]. The basic technique used now is impurity modification (by introduction of micro-additives).

The impurity modification theory is so far insufficiently developed as many of its arguments are contentious and practical application is ambiguous. As for its action mechanism the impurity modification is referred to two types:

1. Surfactants causing decrease in the growth rate of any crystal bodies emerging in cooled melts;

2. Small-size particles that are nucleating crystallization centers. Such particles are either pre-synthesized and then added to the melt (ex situ), or are synthesized in the melt using added components (in situ).

However, the impurity modification techniques have essential weak points manifested to certain extent, namely:

- Limited action duration;
- Re-modification;
- Hydrogenation; and
- Mutual incompatibility.

The key disadvantage is that currently applied technology does not allow for production of articles with a set of properties that can satisfy present requirements for them [2].

In this connection search for new approaches to silumin modification seems to be of high interest. One of such approaches proposes to apply materials produced during the SHS-processes under the centrifugally-accelerated metal clusters effect as modifiers. Such materials have a highly non-equilibrium structure sometimes associated with free valency (unpaired electrons). These high activity materials can render obvious positive effect on the course of the crystallization process and, consequently, modify the cast structure.

To produce a powder modifier there has been taken a sample consisting, according to the x-ray phase analysis (DRON 3.0; CuKα), of aluminum borate, namely $Al_{20}B_4O_{36}$ (31.2 % mass) and corundum (α-Al_2O_3), and $B(OH)_3$ being taken in trace quantities. According to the EPR data (Figure 1), this material contained unpaired electron in its structure (free valency) as an initial material.

The modifier powder of the particles sized about 5 mkm has been produced by material crushing and its subsequent pulverizing in the alundum tube filled with spirit. Such way of crushing allows for production of a powder that is not subject to any considerable impact on its surface structure.
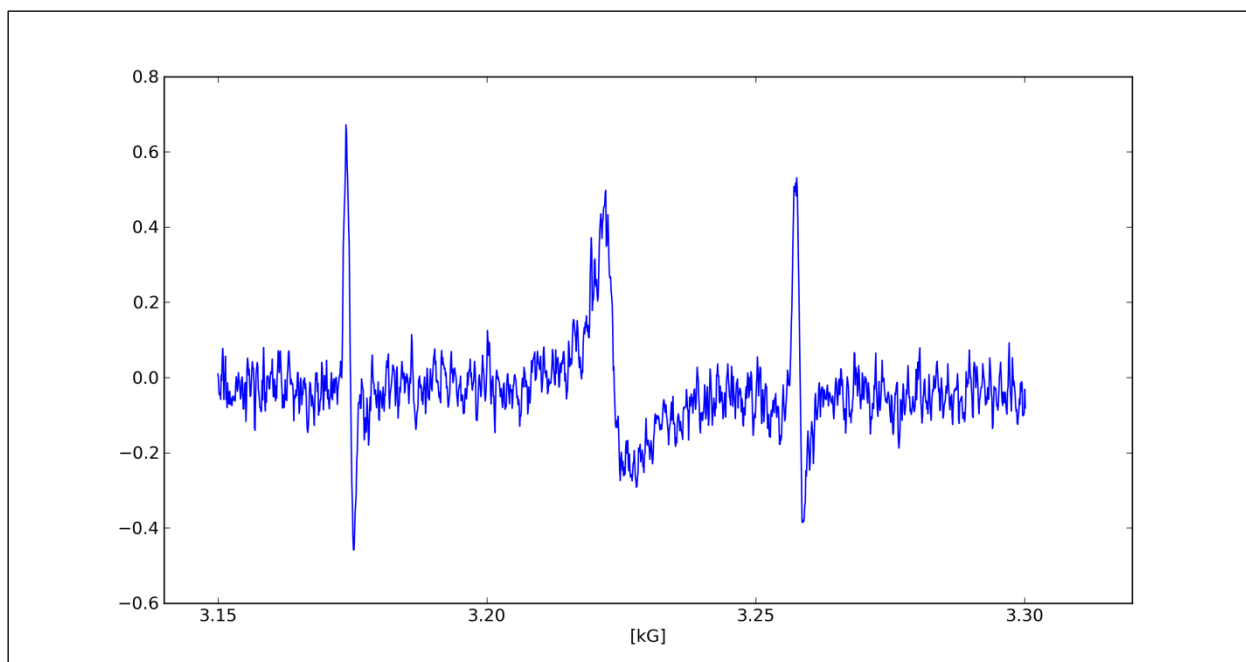
Figure 1 - EPR-spectrum of the modifier powder

Silumin with the silicon content 10.5 % (mass) has been subject to modification. Other impurity kinds have been found to correspond to AK12 alloy (i.e. were not worse).

A 150 g silumin test charge has been melted in the alundum crucible inside the muffle furnace. The 0.52 g modifier sample wrapped in aluminum foil has been embedded in the melt at 820 °C. Ten (10) seconds later the melt was subject to mixing within 20 sec by means of a specially designed mixing device. After mixing the melt has been left in the furnace for 5 minutes at 820°C, and then poured out into a steel casting form heated up to 100°C. Just for comparison: silumin has been cast in the same conditions but without a modifier.

Figure 2 illustrates two pictures of cast modified and non-modified silumin structures. Their comparison shows that addition of the modifier in the amount of 0.33 % (mass) results in radical change of the ingot structure.

Noteworthy that this modifier effect is not caused by any of the approved mechanisms. First of all, syngony and parameters of the crystal lattice of the corundum modifier components (trigonal; a = 0.476 nm, c = 1.292 nm) and aluminum borate (orthorombic; a = 0.769 nm, b = 1.401 nm, c = 0.567 nm) do not correspond to those of the α - aluminum phase (cubic; a = 404 nm) and the silicon β-phase (cubic; and = 0.543 nm). Hence there is not realized the Dankov principle (i.e. the principle of structural conformity between primordial crystallization centers and a crystallizing phase). Available references contain similar examples. Thus, [3] describes modifying properties of aluminum nitride though its crystal structure (hexagonal; a = 0.31 nm, c = 0.50 nm) does not correspond to the aluminum and silicon crystal lattices. On the other hand, the modifying effect cannot be caused just by boron that could get into the melt as a result of reaction (1)

$$B_2O_3 + 2Al \rightarrow 2B + Al_2O_3 \qquad (1)$$

since boron is not an independent modifier in the Al-Si binary system.

It is important that the highest possible boron content in the melt caused by the modifier addition does not exceed 0.012 % (mass). At such content boron is found in a solid solution in the course of the crystallization process.
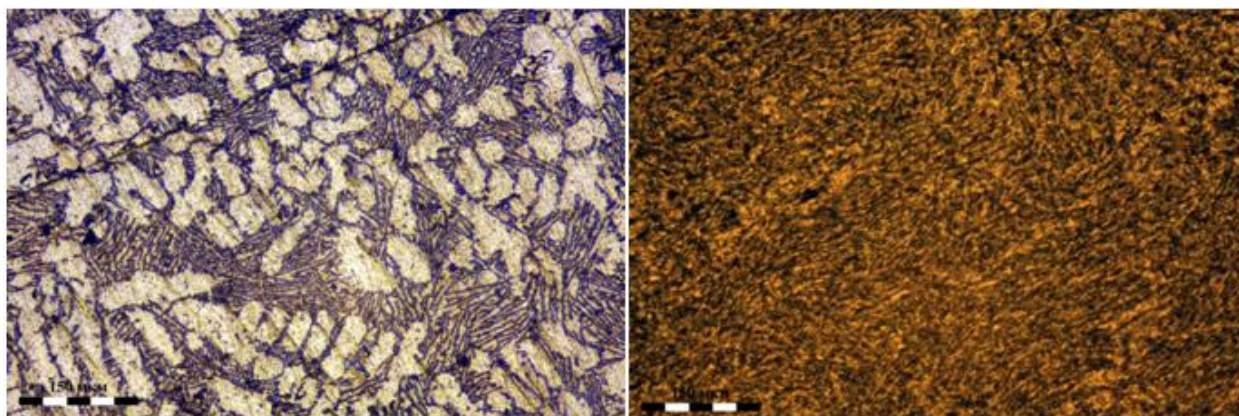
Figure 2 - Microscopic metallography of the modified and non-modified silumin ingots

Conclusion

During the SHS-process within the Al-B-O system there has been synthesized ceramic material with obvious modifying effect on eutectic silumin that cannot be explained just by the existing model representations (i.e. applied mechanisms).

Modifying effect of the material is presumably caused by its strong non-equilibrium associated with free valency (unpaired electrons).

References

[1] V.Y. Stetsenko, E. I. Marukovich Activation of processes of modifying of metals and alloys // Foundary № 11. – 2006 – Pages: 2-6.

[2] Y.P. Skorobogatko Modifying hypereutectic aluminum alloys with use of active additives (review) // Metal and casting of Ukraine № 9. – 2009 – Pages: 1-10.

[3] V. Manolov, A. Cherepanov, R. Lazareva, S. Konstsntiniva Influence of nanopowder inokulum on structure and property of alloy // Foundary № 4. – 2011- Pages: 17-20.

THE INFLUENCE OF FILM STRUCTURE ON AL/PTFE MULTILAYER FOIL LASER IGNITION

SUN Xiujuan, FU Qiubo
Institute of Chemical Materials, sunxj@caep.cn,
No.64 Mianshan Road, Mianyang City, Sichuan Province, PRC.

Abstract
Experiments were carried out to study response behaviors of Al/PTFE multilayer foils under single pulsed laser loading, results showed that finer structured foils went under more fierce reaction than coarser ones, and that pulsed width have a dominate influence on the effects.
Key words: Al/PTFE multilayer films, single pulsed laser, ignition

Introduction

Reactive energetic materials are typically mixed nano-partials or multilayer foils consist of two materials that react exothermically. If sufficient heat is generated via local stimulation, surrounding materials can be heated and caused to mix, generating a runaway reaction that can propagate throughout the entire foil. Examples of exothermic material system that exhibit self–propagating high temperature synthesis reactions include Al/Ni, Al/CuO, Al/PTFE. Al/PTFE multilayer films have higher energy densities than conventional organic explosives and other MIC composed of different fuels and oxidizers.

Laser ignition provides a unique opportunity to characterize ignition processes with a precise and reproducible energy source. There are researches about the laser induced reaction of several different combination of MIC, including Co/Al、Ni/Ti、Al/Pt, trying to reveal the influence of materials on the effect of laser ignition, and another paper reported experiments of nanosecond and femtosecond pulsed laser ignition of reactive Al/Pt[2] multilayer foils. This paper included our experiment on another kind of reactive multilayer foils, Al/PTFE, with pulsed laser, with the purpose of discovering how the multilayer structure influence the reaction.

Experiments

All multilayer films are grown on Si(100) substrates with thickness of 675um, the Al layers were deposited via direct current magnetron sputtering while the PTFE layers via RF magnetron sputtering. The base pressure of the grown chamber is $3\times10\text{-}4Pa$, and sputtering were performed with a process gas of Ar at 0.65a. Three general characteristics define the physical features of a film: the total thickness of the film, the bilayer thickness of the constituent layer, and the proportion between the constituent layers within one bilayer. We prepared three kinds of films with varied characteristics. The status of as-deposited film specimens are listed in table 1.

Table 1 Status of as deposited film specimens

	Bilayer numbers	Total thickness/um	Bilayer thickness/nm	Modulation ratio (from EDX results of section)
A	20	6.6	330(90+240)	1:2.1
B	30	5.1	170(50+120)	1:2.4
C	50	5.3	106(50+60)	1:1.1

The specimen were all capped with PTFE layer to prevent the Al layer from being oxidized, and such that the laser pulse encountered the same material since the as deposited PTFE layers are transparent and Al layers have much larger reflection coefficient.

The laser used for ignition experiments is a Nd:YAG laser with wavelength centered at 1064nm. The laser is operated in a single shot mode, at each test, the ignition determined for a particular foil by an audible "pop" or visible flash indicates that ignition has occurred. All pulsed laser loading were done in air at ambient conditions.

Discussion

Our experiments showed that pulsed laser loading can induce the Al/PTFE to start a reaction, with a bright spark and an audible "pop" sound, and release heat. The reaction that laser trigged did not spread continuously though, only contained in a small area forming a burn mark of various size instead. Photomicrograph and SEM photos of the specimens' surface and cross section before and after laser loading experiments are shown in figure 3. laser pulses with duration of 0.3ms heated a depth of approximately 2um within the spot size, only several layers at the top were set on reaction, leaving a burning mark of metallic luster. 0.5ms width pulses reached a depth of 6um, what left around the burning mark after the foils' combustion expanded and coiled outward forming a crown-like ring of different height and width. The ring is actually made up with many wavery thin layers of reaction products as you can tell from the SEM pictures. EDX test shows the reaction products in this area is pure carbon, which is the result of carbonization cause by elevated temperature. There followed a ring of metallic luster the same as ones loaded with 0.3ms pulses. Lamination also occurred from top layer to the bottom indicating that reactant in this area were more or less consumed in reaction.
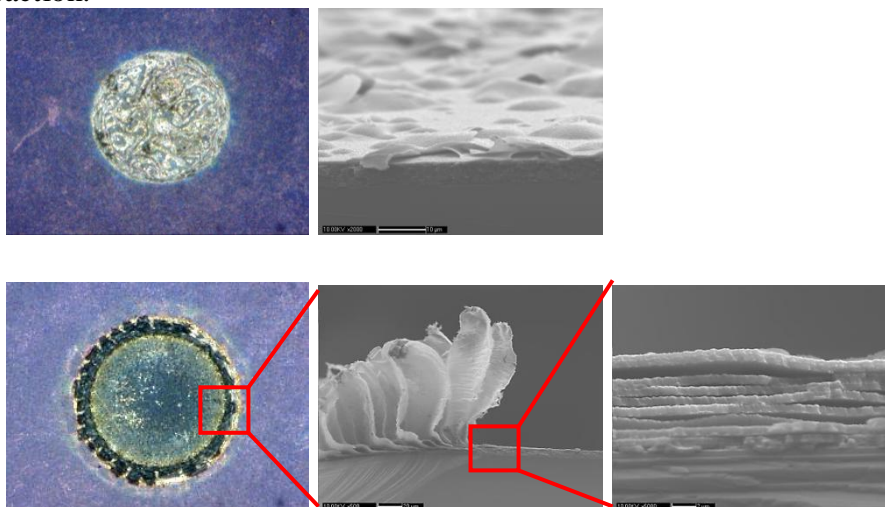
Figure 1 burning mark and their section SEM images after experiment

Burning mark diameter (the diameter of metallic lustering ring) was used to compare represent the extension of reaction, since specimens with different structures got burning marks of different size. The measurement results were organized and presented in figure 4. The chart shows clearly that the reacted zone expands with the width of laser pulsed increases. In the meanwhile, very short pulses, even with high power(0.1ms,5kW), had not been able to set the specimens into reaction. These two experiment results showed that the duration of laser pulse had a obvious lager influence on the ignition of Al/PTFE, compared to the power, indicating that heating effect is the one dominated the laser ignition of Al/PTFE multilayer foils, at lease in these experiments included here.
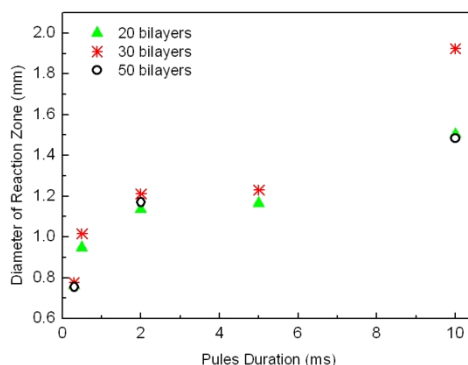
Figure 2 Diameter of reaction zone VS pulse duration from specimens with different structure

The chart can further tell that specimen B (bilayer thickness of 170nm and ratio of 1/2) has the largest reaction zone than the other two. This is because finer structured foil is more easily set on reaction due to shorter mass transfer distance related with larger specific surface area. Meanwhile specimen C(bilayer thickness of 106nm and ratio of 1/1) got smaller reaction zone compared to specimen B despite its finest structure, because the reaction was limited by the fuel rich component. The conclusions is supported by specimen A, which is the coarsest of all but has the same modulation ratio with specimen B, having the similar size of reaction zone with specimen C.

Conclusions

Experiments were carried out to study the response behaviors of Al/PTFE multilayer foils under single pulsed laser loading. Test results showed that the foil can be set onto reaction by laser pulse, and the heating effect contributes more in ignition, and the spread of reaction will benefit from finer structure of the foil。

Since the refine the structure will contribute to a easier ignition, and a 3D structure of similar scale will provide larger specific surface area, research should be taken in construction and experiments on 3D structured energetic foils. On the other hand, experiments in this paper showed that fuel-rich reaction cannot sustain, but experiments balanced and oxidizer-rich combinations need to be done.

References

[1] Jun Wang, Zhiqiang Qiao, Yuntao Yang, Jinpeng Shen, Zhang Long, Zhaoqian Li, Xudong Cui, and Guangcheng Yang. Core–Shell Al-Polytetrafluoroethylene (PTFE) Configurations to Enhance Reaction Kinetics and Energy Performance for Nanoenergetic Materials. Chem. Eur. J. 2016, 22, 279 – 284

[2] Joel P. McDonald, Yoosuf N Picard, Steven M. Yalisove, David P. Adams. Nanosecond and femtosecond pulsed laser ignition of reactive multilayer foils. Mater. Res. Soc. Symp. Proc. Vol. 1146-NN05-04

[3] Jeffery B. DeLisio, Xiuli Hu, Tao Wu, Garth C. Egan, Gregory Young, and Michael R. Zachariah J. Probing the Reaction Mechanism of Aluminum/Poly(vinylidenefluoride) Composites. Phys. Chem. B 2016, 120, 5534−5542

[4] Eric S. Collins , Brandon R. Skelton , Michelle L. Pantoya a, Fahmida Irin b, Micah J. Green ,

Michael A. Daniels. Ignition sensitivity and electrical conductivity of an aluminum fluoropolymer reactive material with carbon nanofillers. Combustion and Flame 162 (2015) 1417–1421

SYNTHESIS AND STUDY OF THE PROPERTIES OF WS$_2$ SINGLE CRYSTALS GROWN ON A QUARTZ SUBSTRATE BY THE CVD METHOD

A.A. Shaikenova, R.E. Beisenov, D.A. Muratov, B.A. Rakymetov
LLP «Institute of Physics and Technology»
11 Ibragimov St., Almaty, Kazakhstan, e-mail: info@sci.kz

Abstract
WS$_2$ single crystal growth of on quartz substrate by CVD method is introduced. Optical microscope shows formation of triangular shape WS$_2$ domains with single-phase crystal structure at growth temperature 900 ^{O}C. Raman spectroscopy analysis determined that the thickness of WS$_2$ is equal to 6 layers. PL spectroscopy of synthesized WS$_2$ crystal shows semiconductor properties with 1.96 eV band gap.

Introduction

Due to their unique electronic and optical properties, transition metal dichalcogenides (TMDs) are fundamentally and technologically interesting materials [1]. TMDs have isolating, semiconductor, metallic, and even superconducting properties, which depends on atomic layer thickness. New properties could be observed by reducing of TMDs atomic layers which induced by quantum limitation [2]. Multilayered two-dimensional (2D) TMDs nanostructures can be obtained similar as graphene. There are two methods: top-down means mechanical exfoliation and bottom-up by chemical vapor deposition (CVD) method [3]. A purpose of CVD synthesis is obtaining one or few atomic layers of single crystal structured TMDs. Attempts to control the properties of atomic layers and to obtain a single-crystal structure will improve performance in comparison with their polycrystalline structure, thereby improving their application in many devices.

2H-WS$_2$ synthetic crystal have been grown by chemical vapour transport (CVT) method, and then mechanically exfoliated and deposited on quartz SiO$_2$/Si substrates [4]. The evolution of electronic structure of thin WS$_2$ sheet is studied. New heterostructures based on it may have unique optoelectronic, electro catalytic and photo catalytic functionalities [4-6]. However, obtained films were not atomic thickness, so several CVD methods have been developed.

Monocrystalline TMD layers or dimension is still relatively small compared with the single-crystal graphene layers. So, CVD deposition of single crystal TMDs further investigation is required. Nevertheless, some progress have been achieved in the CVD deposition of larger sizes monocrystalline 2D TMD in recent years. The main solution is reducing nucleation density to

produce large domains/grains, also controllable growth process to obtain individual domains which has less shape or without interaction at boundaries.

Main part

The synthesis of individual WS_2 crystals carried out by sulfurization of tungsten oxide thin layer on quartz substrate. Thin tungsten oxide (WO_3) layers were synthesized on a quartz substrate (SiO_2), where metallic tungsten with 10 nm thickness oxidized in tubular reactor at 500^0C temperature in oxygen atmosphere. Structural analysis of WO_3 films shows the formation of polycrystalline structure with 5-7 nm grain sizes which determined by the Scherer equation.
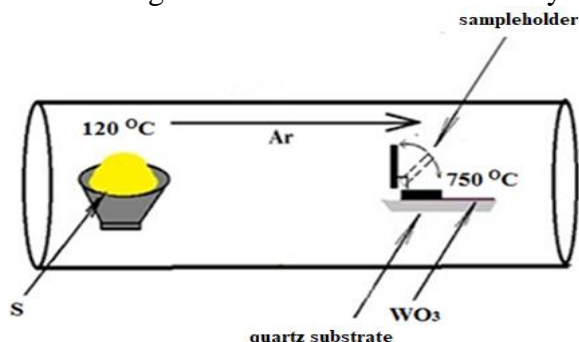
Figure 1- Schematic presentation of CVD system

CVD synthesis of WS_2 single crystals on a quartz substrate carried out in a vacuum quartz reactor located in three zone tubular furnace. A corundum boat with sulphur powder placed in the first heating zone. Sample of WO_3 / SiO_2 placed in the second zone. Synthesis of WS_2 was carried out at temperatures of SiO2 substrate 800-1000 ° C, carrier gas flow (argon) 500 sccm. During the synthesis, the sulphur heating zone (S) was held at 120 °C to produce vapours. Buffer gas argon provided transportation of sulphur vapour by a flow path into the reaction zone.

Monocrystalline WS_2 grains larger than 20 μm were grown during the sulfurization process of the oxide layer at 900 °C temperature (Fig. 2). It is determined that the growth of the individual grains WS_2 by CVD occurs on substrate edge and which is away from maximum temperature area. Granular formed and partly destroyed the substrate.
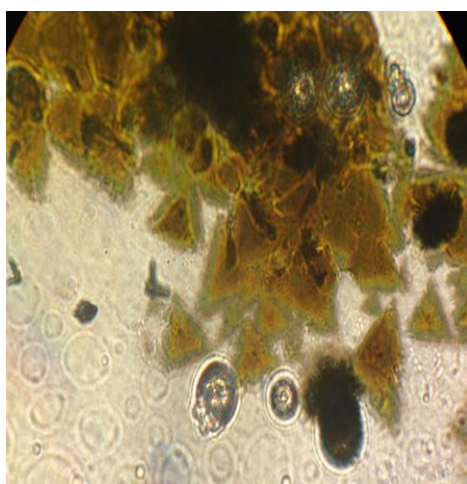
Figure 2- Optical microscope image of obtained WS_2 grains

Atomic force microscopy analysis of synthesized WS_2 layer showed relatively smooth surface with 3 nm roughness (Fig. 3). In 2D picture of AFM, orientated carbon structure is observed.
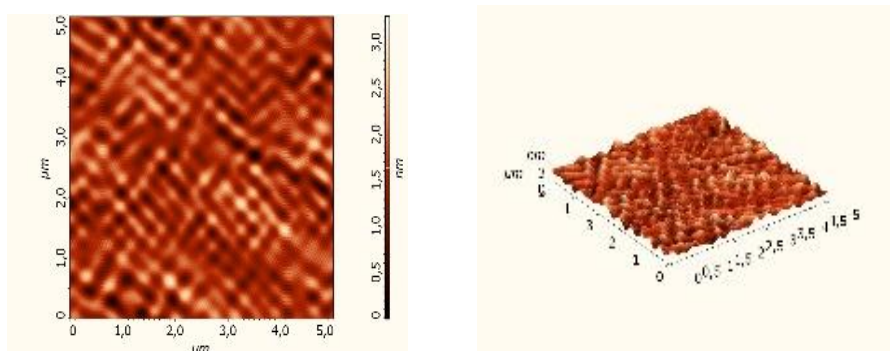
Figure 3– (AFM) The surface of WS_2 grown layer at 900 °C

Photoluminescence spectroscopy is shown on Figure 4, which revealed a strong peak between 600-660 nm, typically for a monolayer WS_2 crystal, where the band gap is equal to 1.96 eV.
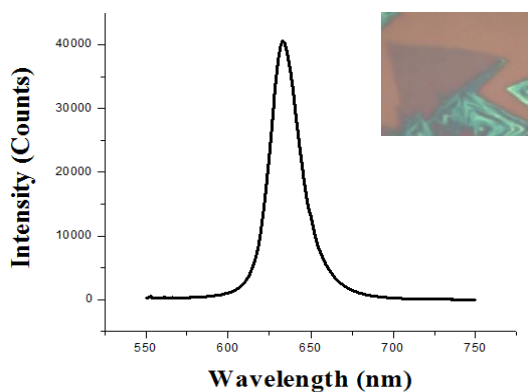
Figure 4 – Photoluminescence spectrum for produced WS_2 single crystals
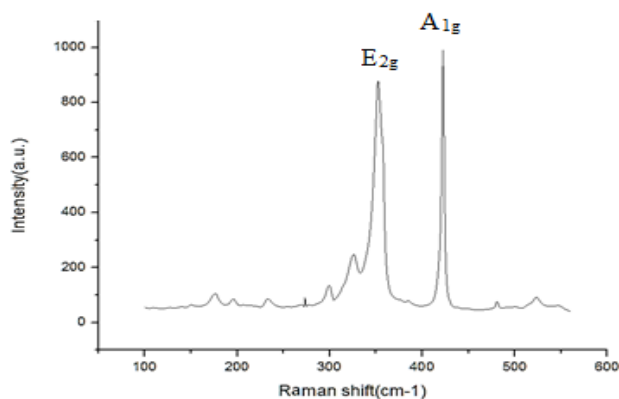
Figure 5 - Raman spectra of obtained WS_2 crystals

Obtained WS_2 triangle shape single crystals confirmed by Raman spectroscopy. He:Ne laser with a wavelength of 632.8 nm was used as a radiation source. Figure 5 demonstrates the

characteristics in-plane E_{2g} mode and the out-of-plane A_{1g} mode respectively at ~350 and ~420 cm^{-1} for WS_2 crystalline structure. The intensity of the peaks is almost the same. According to the position of the mode peaks, it is assumed that the thickness of the grown WS_2 is 6 layers.

Conclusion

WS_2 single crystals were obtained by CVD method thru sulfurization of tungsten oxide thin layer on quartz substrate. Synthesis of WS_2 was carried out at 800-1000 ° C in CVD system. The sulphur vapour is transported by argon gas (500 sccm). Optical microscope analysis demonstrated that triangular WS_2 domains with single phase crystal structure are formed. The thickness of WS_2 is 6 layers, which determined by Raman spectroscopy. PL spectroscopy shows that the band gap is equal to1.96 eV for WS_2 crystals.

References

1. S. Z. Butler, S. M. Hollen, L. Cao, Y. Cui, J. A. Gupta, H. R. Gutierrez, T. F. Heinz, S. S. Hong, J. Huang, A. F. Ismach, E. Johnston-Halperin, M. Kuno, V. V. Plashnitsa, R. D. Robinson, R. S. Ruoff, S. Salahuddin, J. Shan, L. Shi, M. G. Spencer, M. Terrones, W. Windl and J. E. Goldberger, Progress, Challenges, and Opportunities in Two-Dimensional Materials Beyond Graphene, ACS Nano, 2013, 7, 2898–2926.

2. M. Chhowalla, H. S. Shin, G. Eda, L. Li, K. P. Loh and H. Zhang, The chemistry of two-dimensional layered transition metal dichalcogenide nanosheets, Nat. Chem., 2013, 5, 263–275.

3. J.N.Coleman,M.Lotya,A.O'Neill,S.D.Bergin,P.J.King,U.Khan,K.Young,A.Gaucher,S.De,R.J.Smith, I. V. Shvets, S. K. Arora, G. Stanton, H. Kim, K. Lee, G. T. Kim, G. S. Duesberg, T. Hallam, J. J. Boland,

4. W. Zhao, Z. Ghorannevis, L. Chu, M. Toh, C. Kloc, P. Tan andG. Eda, Evolution of Electronic Structure in Atomically Thin Sheets of WS2 and WSe2, ACS Nano, 2013, 7, 791–797.

5. Q. H. Wang, K. Kalantar-Zadeh, A. Kis, J. N. Coleman and M. S. Strano, Electronics and optoelectronics of two-dimensional transition metal dichalcogenides, Nat. Nanotechnol., 2012, 7, 699–712.

6. M. Bernardi, M. Palummo and J. C. Grossman, Extraordinary Sunlight Absorption and One Nanometer Thick Photovoltaics Using Two-Dimensional Monolayer Materials, Nano Lett., 2013, 13, 3664–3670.

Uncertainty Quantification in Chemical Modeling

N.A. Slavinskaya, JM.Abbasi, .H.Starcke, A.Mirzayeva,
German Aerospace Center (DLR), Institute of Combustion Technology, 70569, Stuttgart, Germany

W. Li, M. Frenklach,
Mechanical Engineering, University of California at Berkeley, Berkeley, CA 94563, USA

The Bound-to-Bound Data Collaboration (B2B-DC) module of the automated data-centric infrastructure of PrIMe was used for the systematic uncertainty and data consistency analyses of the H_2/CO reaction model (73/17). For this purpose, a dataset was constructed that included a total of 167 experimental targets (ignition delay time and laminar flame speed) and 55 active model parameters (pre-exponent factors in the Arrhenius form of the reaction rate coefficients). Consistency analysis of the composed dataset revealed disagreement between models and data. Two consistency measures were applied to identify the quality of experimental targets (Quantities of Interest, QoI): a newly-developed method of computing the vector consistency measure (VCM), which determines the minimal bound changes, each bound by its own extent; and scalar consistency measure, which quantifies how much the constraints can be tightened while still ensuring the existence of a set of the model parameter values whose associated model predictions match (within the bounds) the experimental QoI. The analysis suggested that removing 45 experimental targets, 8 of which were self-inconsistent, would lead to a consistent dataset. After that the feasible parameter set was constructed through decrease uncertainty parameters for several reaction rate coefficients. This dataset was subjected for the B2B-DC framework model optimization and analysis on. Forth methods of parameter optimization were applied, some of them unique to the B2BDC framework. The optimized models demonstrated improved agreement with experiments, as compared to the initially-assembled model, and their predictions for experiments not included in the initial dataset were investigated. The results demonstrate benefits of applying the B2BDC methodology for developing predictive kinetic models

I. Introduction

To reliably develop predictive reaction models for complex chemical systems requires integration of large amounts of theoretical, computational, and experimental data collected by numerous researchers. The integration entails assessment of the consistency of the data, validation of models, and quantification of uncertainties for model predictions. This approach to the development of mechanistic reaction models consists of conjecturing the reaction mechanism and comparing the predictions of the constructed model to available experimental observations. Typically, such comparisons result in mixed outcomes: some show a reasonably close agreement and some do not. In the latter case, the apparent inconsistency obtained between the model and the experiment is argued to imply either that the model is inadequate or that the experiment (or, rather, its interpretation) is incorrect.

Bound-to-Bound Data Collaboration, abbreviated hereafter as B2B-DC, is an optimization-based framework for combining models and experimental data from multiple sources to explore their collective information content. The methodology tests consistency among data and models, explores sources of inconsistency, discriminates among differing models, makes model interval predictions, and analyzes sensitivity of uncertainty propagation.[1-8]

The general setting is as follows. We consider a physical process that can be represented by a numerical model, $M(x)$, with parametric dependence on unknown/uncertain physical parameters, x. There is prior knowledge/assumptions on the domain of parameters, thus constraining each x to an interval $[x_{min}, x_{max}]$ and all together to a hypercube $x \in H$. We also have a collection of experimental observations, referred hereafter as Quantities of Interest (QoI), with respective uncertainties, assessed as lower and upper bounds on the observed QoI values, i.e., L_e and U_e for each e-th QoI. The computational models must produce outputs that are consistent with the experimentally observed bounds in the experimental reports. Hence additional constraints that the true parameters must satisfy are

$$L_e \leq M(x) \leq U_e \quad \text{for all } e. \tag{1}$$

The subset of H satisfying (1) is called the *feasible set*, Φ, of parameters. Φ is simply all parameter values that jointly satisfy all of the prior information and are consistent with all experiment prediction models and actual observed outcomes. A parameter value that is not in Φ is at odds with at least one of these constraints. The mathematical methodology B2B-DC is invoke constrained optimization over the feasible set Φ,

$$\left[\min_{x \in F} f(x) \quad \max_{x \in F} f(x) \right]$$

where f is a function of interest, and the computed *min* and *max* constitute the "to-bound" aspect of the nomenclature. In short, the bounds that describe the prior information and the bounds on experimental observations are mapped into bounds on prediction. Two common instances are described next.

Dataset consistency. The feasible set is a representation of the complete collaborative information contained in a dataset, and questions in the B2B-DC framework are posed as optimization problems over the feasible set. This naturally raises the question of dataset consistency. To assess it numerically, a consistency measure was introduced[8] that answers the question "What is the largest percentage of uncertainty reduction such that there exists a feasible parameter vector?" Associated with a given dataset $\mathbf{D}$, it is notated C_D and posed as an optimization problem,

$$C_D = \max_{\gamma, x \in F} \gamma, \quad \text{subject to (for all } e):$$

$$(1-\gamma)\frac{L_e - U_e}{2} \leq M_e(x) - \frac{U_e + L_e}{2}$$

$$M_e(x) - \frac{U_e + L_e}{2} \leq (1-\gamma)\frac{U_e - L_e}{2}.$$

(2)

In this definition, the original constraints $L_e \leq M_e(x) \leq U_e$ are augmented with a scalar γ, where positive values of γ imply tightening of the constraint, and negative values imply loosening. The consistency measure quantifies how much the constraints can be tightened while still ensuring the existence of a set of parameter values whose associated model predictions match (within the bounds) the experimental QoI. The dataset is consistent if the consistency measure is nonnegative, and is inconsistent otherwise.

To continue with the analysis, we employed a newly-developed method of computing the vector consistency measure (VCM), similar to eq 2, but with original constraints augmented with individual relaxations γe for each bound[10]. The VCM method determines the minimal bound changes, each bound by its own extent, that result in dataset consistency.

Model prediction. Consider a physical configuration (set of conditions) not exercised experimentally but with a property P predicted by model M_P. A natural and perhaps the ultimate question of scientific inquiry is "what is the range of values this model exhibits over the domain of feasible parameter values?" In other words, what is the prediction interval for property P that is consistent with all of the model/observation pairs in the dataset? We refer to this as model prediction.

The B2B-DC computation expresses this question into two optimization problems for the lower and upper interval endpoints, L_P and U_P,

$$L_P := \min_{x \in F} M_P(x)$$

$$U_P := \max_{x \in F} M_P(x)$$

(3)

The length $U_P - L_P$ quantifies the amount of uncertainty in M_P's value conditioned on the fact that the true parameter vector is contained in the feasible set Φ.

The results of the proposed analysis suggest a sequential procedure with step-by-step identification of outliers and inspection of the causes. The analysis identifies a specific direction to follow for improving dataset consistency and provides an estimate of the extent of possible improvement. Altogether, this numerical approach offers a tool for assessing experimental observations and model building and improvement.

In the present paper Data Collaboration module of PrIme[1] was applied to the H_2/CO sub-system of the kinetic model[9] to
1) test the numerical algorithms, modules and user interface of the PrIMe;
2) investigate an algorithm of the consistent dataset construction;
3) test the different chemical kinetic model optimization strategies.

II. PrIMe DataSet

A. Reaction Model

The H_2/CO sub-model (6 elements, 17 species, 73 reactions) of C_1-C_2 reaction mechanism[9] with improvements performed on the data followed from the studies [11-21] was used to perform systematic uncertainty and consistency analyses with the Data Collaboration module of PrIme to obtain the feasible set sampling for the base H_2/CO chemistry of DLR reaction data base. The reaction rate coefficients in the examined sub-model were reviewed with further attention to the pressure depending and multichannel reactions.

The uncertainty factors for rate coefficients were assumed equal to the proposed ones in the sources or evaluated from statistical treatment of the different data:

$$f_u(T) = \frac{k_{upper}(T)}{k_0(T)}$$

$$\tag{4}$$

$$f_l(T) = \frac{k_0(T)}{k_{low}(T)} \quad ,$$

where k_0 is the nominal rate coefficient, k_{low} and k_{upper} are lower and upper bounds.

The active parameters were identified via sensitivity analysis accomplished with uncertainties, represented by the lower and upper bounds. They were assumed equal to those proposed in literature sources or evaluated from a statistical treatment of the literature data.

B. Ignition-delay-time QoI

Quantification of uncertainties in the shock tube is ultimately needed prior to undertaking any tuning of the kinetic parameters to match ignition targets. If some active phenomena in the shock tube experiments cannot be described by assuming homogeneous conditions (constant V, U system) behind the reflected shock, they are classified as "non-idealities" in the shock tube experiments.[22-31] Both, facility-dependent effects and energy-release phenomena can increase the non-idealities and influence the instrument readings, thus adding to the uncertainty of experimental data. For the syngas mixtures, the two regimes of ignition should be recognized: weak ignition - the non-uniform and distributed ignition and strong ignition- initiated by auto ignition at the end wall of the shock-tube and propagating through the mixture.[27]

Although, the non-idealities present in shock tubes have been well-discussed, [22-31] the quantitative evaluation of their effects on the reported ignition delay data is a very crucial problem. To evaluate the uncertainty bounds of the measured observations included in the dataset, the empirical algorithm is proposed. For that, the most strong non-ideality phenomena[22-31] were determined across the investigations and the facility-related and fuel-related factors, which affect these phenomena, have been identified.

It was found that experimental data obtained by using large diameter shock tubes (~ 10cm), dilute fuel/oxidizer mixtures in monoatomic gases, and short test times (less than about 500 μs) have the lowest uncertainty level. A correspondence with the diameter of the shock-tube and weak ignition is found: the larger diameter leading to an ignition delay close to that of a homogeneous reactor.

It was assumed, that in the best case (strong ignition, diluted mixture, t_{meas} = 50ms – 500ms, shock tube diameter > 10 cm, length of driven-section > 8m) the uncertainty can be assumed ~15%. Deviations from these conditions are evaluated by adding a 5% uncertainty for each criterion not satisfied to the ideal case. For measured ignition delay time longer as 1000 μs 5% uncertainty is added per every 1000 μs. Radical impurities were evaluated as extra 5% uncertainty to the ideal case.

We selected 122 ignition delay targets with obtained uncertainty evaluation from the shock tube experiments [32-39] for the dataset.

C. Laminar-flame-velocity QoI

Syngas flame velocities at 0.1-0.5 MPa have been investigated by using almost all known techniques.[40-41] The flame velocity data at high pressures are relatively sparse. Experimentalists consider the current uncertainties of laminar flame speed measurements to be in a range of about 5–10%, but also indicating its increase with pressure (>0.5 MPa) and fuel-air ratio (φ>2). [40-41]

Uncertainty bounds of experimental data were evaluated from studies [40-41] and analysis of the current syngas atmospheric laminar flame speed data distribution, which can be found in [41]. From the data analysis following from [37-44], the uncertainty of available data can be assumed to be 10% for φ< 2, 15% for 2 < φ< 3, and 20% for φ>3. The uncertainties for experimental data measured at higher pressure have been evaluated by adding 5%.

The 45 laminar flame speed data included in the dataset are taken from studies [19, 36,40,42-50]. They are selected to cover as optimal as possible the full range of operating conditions available in the literature.

A preferred key (or PrIMe ID) was prescribed to each structural element in the reaction model and each experimental target. In this way, each structural element has a "pointer" to the referenced information and/or file. All the experimental and model data were documented in the PrIMe Data Warehouse.[1] Selected for analysis experimental QoI are described in the dataAttribute files of the PrIMe data collection.[1] These QoI together with the corresponding model $M_c(x)$ and the experimental and parameter bounds form a dataset. The complete model and experimental data are available in the PrIMe Data Warehouse.[1]

III. General Results

The ignition delay times and laminar flame speeds were modeled with numerical tools of PrIMe,[1] numerical packages CHEMKIN II[51] and Chemical Workbench.[52] The ignition delay time was computationally defined by the peak in the OH or OH* concentration, temperature, or pressure. It is pointed in the attribute files of PrIMe Warehouse. The thermal diffusion model was applied for calculation of one-dimensional freely propagating laminar premixed flame using CHEMKIN II with over 1000 grid points for each condition.

A. Dataset Consistency (Data Quality)

We began the analysis by employing eq 2 with the initial dataset, which included all 167 QoI (122 ignition delays

Table 1. The 8 Self-inconsistent QoI

p_5 (atm)		ϕ	target PrIMe ID	estimated uncertainty (%)	ref
1263	1.1	0.5	a00000309	30	[32]
1695	1.6	0.5	a00000352	30	[36]
2004	1.6	0.5	a00000355	25	[36]
1975	1.6	0.5	a00000358	25	[36]
1436	1.6	0.5	a00000359	25	[36]
1027	1.6	0.5	a00000360	35	[36]
1883	1.6	0.5	a00000503	30	[38]
1008	1.6	0.5	a00000504	50	[38]

and 45 laminar-flame speeds) and 55 active parameters. The results indicated a massive inconsistency. Eight QoI, those listed in Table 1, were found to be self-inconsistent. These were the ignition delay times that were not able to be reproduced within their respective uncertainty bounds by the model employing rate coefficients within their respective uncertainty bounds, H. These eight self-inconsistent QoI were removed from the initially-constructed dataset. The latter, however, still remained an inconsistent dataset.
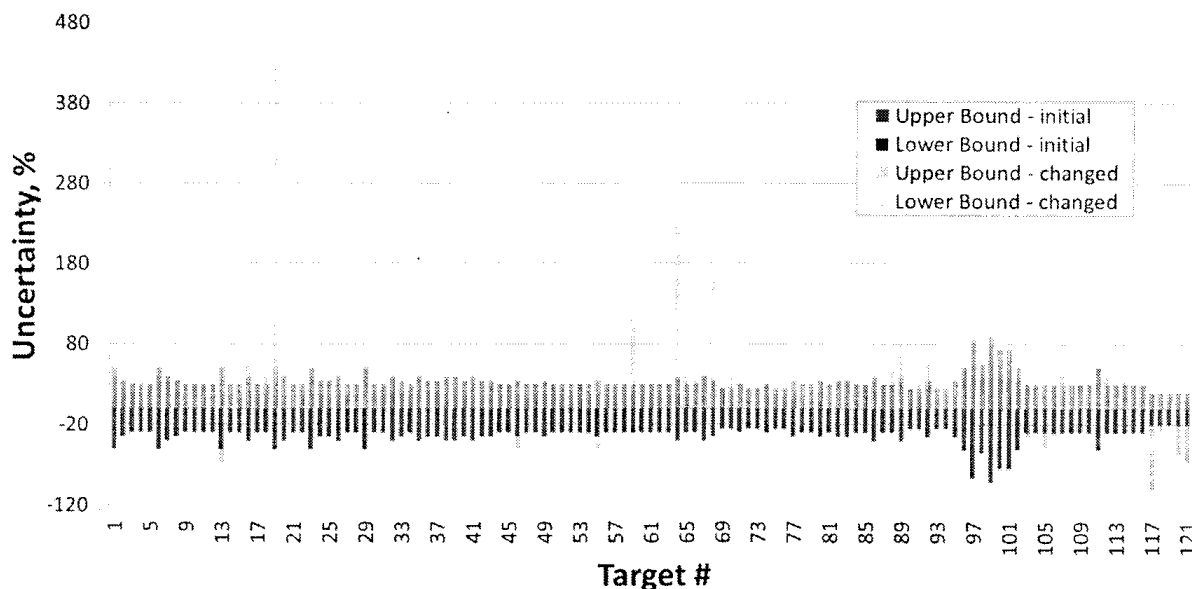
Figure 1. Bound Changes of the Ignition QoI Suggested by VCM, DLR-SynG 1 dataset.

To continue with the analysis, we employed a newly-developed method of computing the *vector consistency measure* (VCM), similar to eq 2, but with original constraints augmented with *individual* relaxations y_c for each
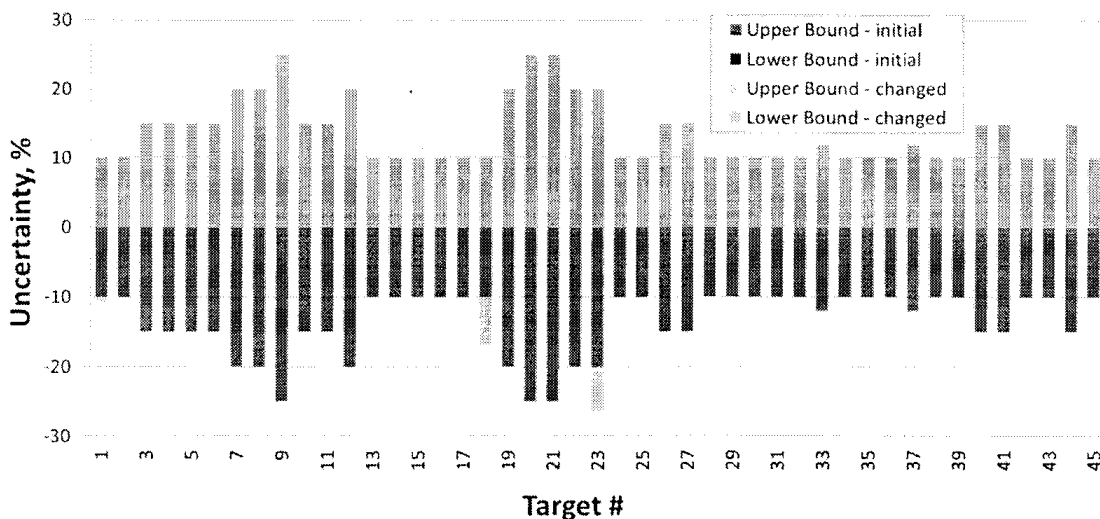
Figure 2. Bound Changes of the Laminar-flame-speed QoI Suggested by VCM, DLR-SynG 1 dataset.

bound.[10] The VCM method determines the minimal bound changes, each bound by its own extent, that result in dataset consistency. Its application identified such a dataset-consistency point by changing 30 ignition delay times and 7 laminar flame speeds, shown in Figures 1 and 2, respectively. We emphasize that the VCM-identified feasible

parameter set is a *single point* in H. As this point possesses some optimal attributes, we compare the model predictions obtained with this set of parameters, *DLR-SynG 1 dataset*, to the optimization results.

To proceed with further features of the B2BDC framework, we created a new dataset by removing the 37 QoI identified by VCM, thus forming the DLR-SynG 2 dataset contacting 122 QoI. This latter dataset is consistent, meaning that all its 122 QoI are consistent with each other and with the 55 active parameters.

B. Feasible set construction

While **H** designates prior information, feasible set **Φ** summarizes *posterior* information: all parameter value combinations that satisfy their own bounds and also the QoI bounds. The size and shape of **Φ** compared to those of **H** represent information gained as a result of the B2B-DC analysis.

Projection of **Φ** on each of the x's yields the posterior range of the parameter uncertainty.[3] Those that changed are reported in Figure 3. For the rest of the parameters, the posterior ranges were the same as the prior ones, indicating that the experimental data included in the present analysis did not aid in narrowing down the uncertainty ranges of these parameters individually. However, such an outcome does not necessarily imply no information gain for a given parameter: while the extreme parameter values (bounds) may not change, the feasible set may, and usually does, eliminates some combinations of these parameters with others, which is addressed next.

	HO2+H→H2+O2	CO+OH→CO2+H	CO+O(+M)→CO2(+M)	H+O→OH	H2+O→OH+H	HO2+OH→H2O+O2	H2+OH→H2O+H	O2+H→OH+O
▇ Prior Lower bound	-0,69	-0,22	-0,69	-1,61	-0,46	-1,14	-0,43	-0,22
▨ Posterior lower bound	-0,57	-0,22	-0,69	-0,036	-0,21	-0,93	-0,43	-0,11
▇ Prior upper bound	0,69	0,23	0,69	1,61	0,46	1,15	0,49	0,23
▨ Posterior upper bound	0,69	0,078	0,68	1,61	0,46	1,15	0,42	0,23
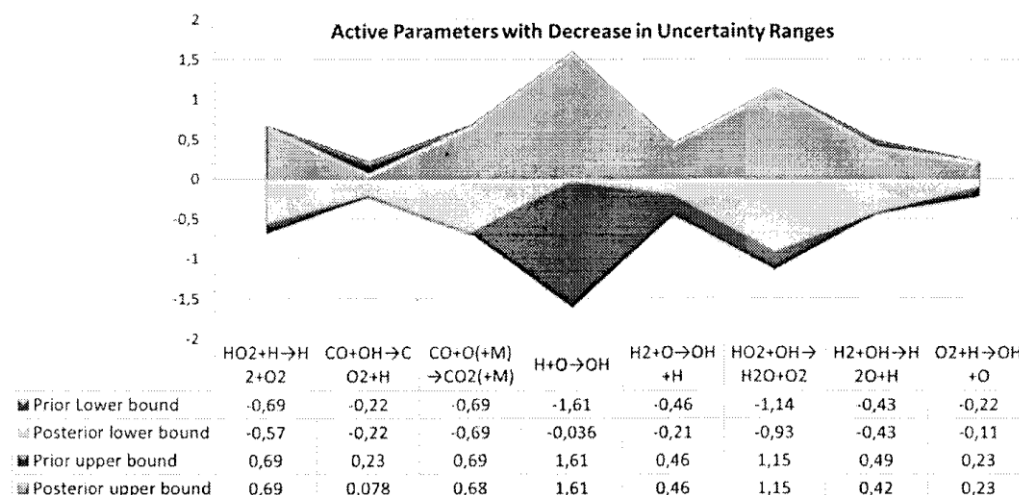
Figure 3. Active Parameters with Decrease in Uncertainty Ranges at feasible set construction.

IV. Parameter optimization

While the primary focus of the B2B-DC framework is on prediction over the feasible set, it also supports parameter optimization.[53] Four sets of optimized model parameters were investigated and inter-compared in the present study. The first approach is LS-H, a (weighted) least-squared fit constraining parameter values to their initially assessed uncertainty ranges, **H**. This is now a common approach.[6, 8, 53] B2B-DC supports two more refined methods of optimization,[53] LS-F and 1N-F, where the objective is minimized with x's being constrained to the feasible set **Φ**. The three problems are easily expressed as mathematical optimizations. The LS methods minimize the familiar sum of weighted least-squared deviations between the surrogate model prediction and the reported measured value, y_e. The difference lies in where the search takes place: LS-H considers all of H while LS-F restricts the search to F,

$$\text{LS-H}: \quad \min_{x \in H} \sum_e w_e \left[M_e(x) - y_e \right]^2$$

$$\text{LS-F}: \quad \min_{x \in F} \sum_e w_e \left[M_e(x) - y_e \right]^2$$
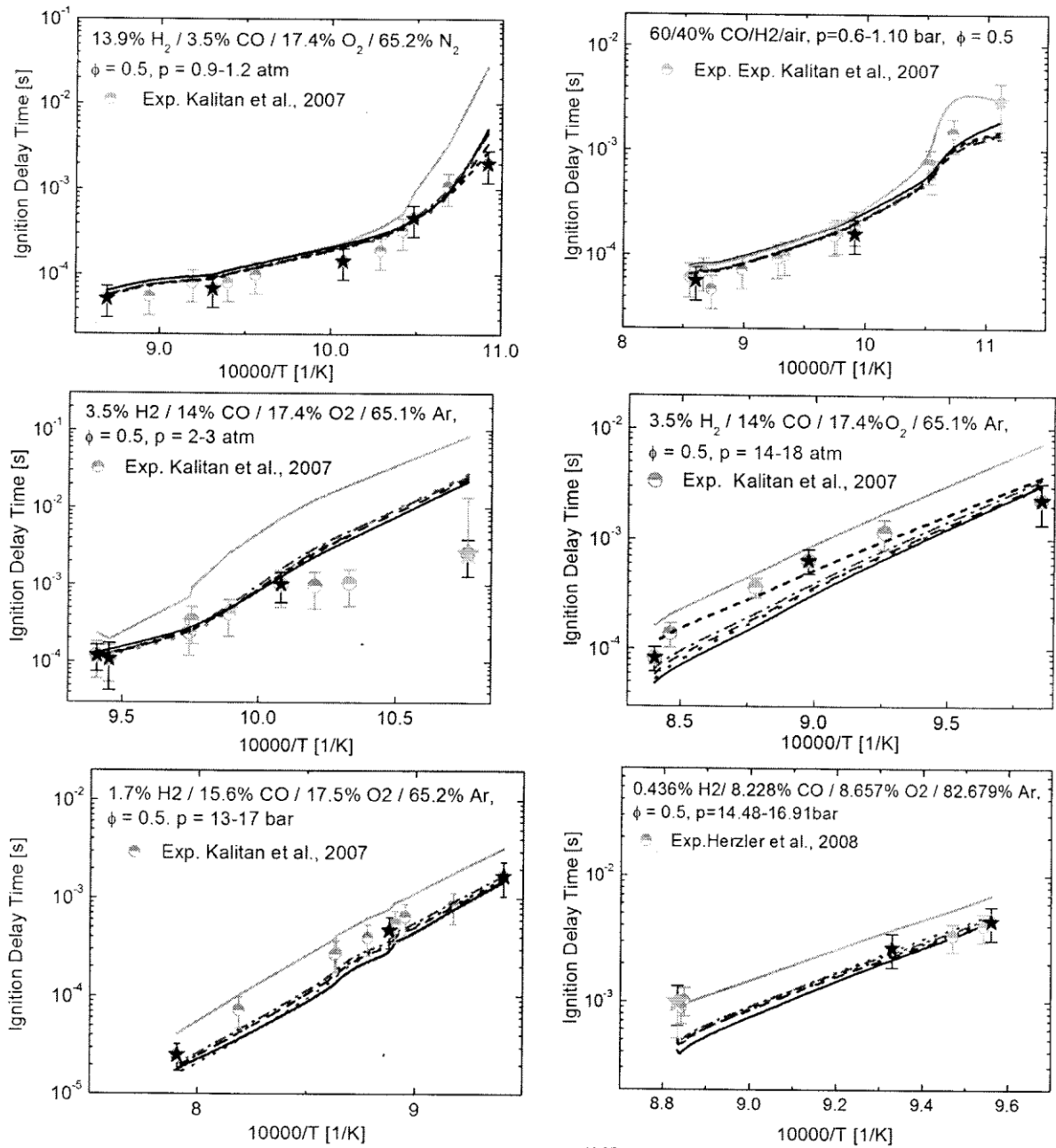
Figure 4. Ignition delay times: symbols, experimental data;[32,35] initial model, black line; Varga et al.[54] model, gray line; LS-H, red dotted line; VCM, red dash-dotted line; LS-F, blue dashed line; 1N-F, blue short-dash line. Black stars are targets of DLR-SynG 2 dataset; green stars are targets deleted from DLR-SynG 1 dataset.
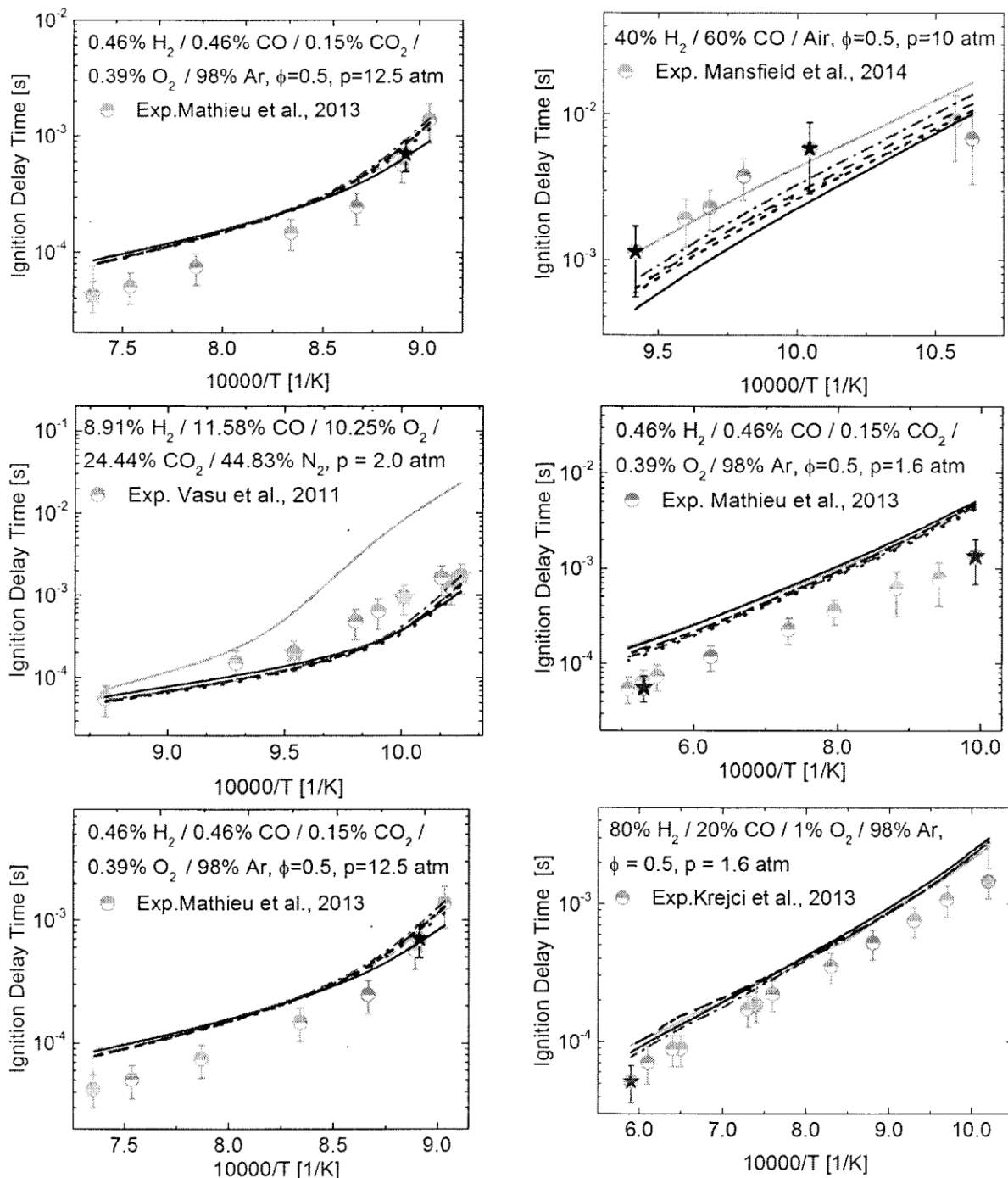
Figure 5. Ignition delay times: symbols, experimental data;[36-39] initial model, black line; Varga et al.[54] model, gray line; LS-H, red dotted line; VCM, red dash-dotted line; LS-F, blue dashed line; 1N-F, blue short-dash line. Black stars are targets of DLR-SynG 2 dataset; red stars are self-inconsistent targets; green stars are targets deleted from DLR-SynG 1 dataset.
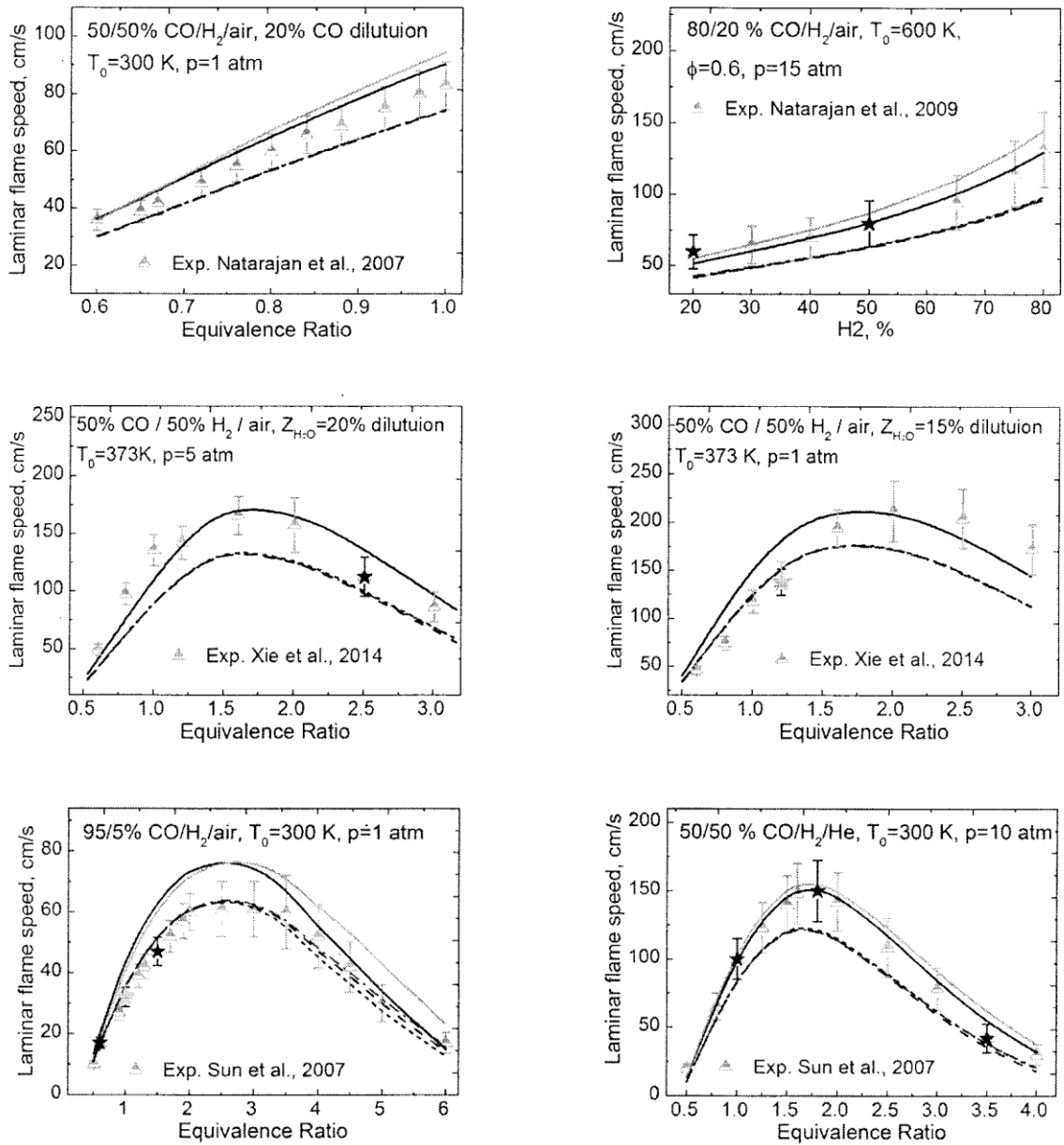
Figure 6.Laminar flame speeds: symbols, experimental data;[19,42,44,47] initial model, black line; Varga et al.[54] model, gray line; LS-H, red dotted line; VCM, red dash-dotted line; LS-F, blue dash line; 1N-F, blue short dash line.

By contrast, the 1N-F problem treats the nominal parameter vector, the starting set of parameter values ($x_0 = 0$), as "preferred". As we have shown in previsions sections, this parameter set lies outside the feasible region Φ. The goal of the 1N-F method is to find with least number of changes to x_0 a parameter vector that is feasible. Mathematically, the one-norm is a well-known approximation to enforce such sparsity, i.e.,

$$1N\text{-}F: \quad \min_{x \in F} \|x - x_0\|_1$$

The LS-F and 1N-F optimizations were performed with the final dataset, as the two methods are designed to work with an existing feasible set. Inspection of the results highlights several features. All optimization methods

result in parameter sets that produce a better agreement with experiment than the original set, composed of literature recommendations. The LS-H optimization, constrained only to the prior uncertainty ranges of parameters, results in the lowest average deviation, as expected, but at the expense of violating uncertainty bounds of 13 experimental QoI.

The average deviation produced by LS-F is larger but not significantly than that of LS-H. The 1N-F method gives a larger average deviation, yet it changes the least number of variables. The LS-F and 1N-F optimization methods, with additional constraints to the QoI uncertainties, do not violate any of the QoI bounds by design unlike to the LS-*H*. That demonstrates the main difference between two approaches: LS-H optimization can be identified rater as a fitting.

Some of the individual comparisons are shown in Figures 4-6, with the inclusion of the most recent literature model.[54] Experimental targets of the DLR-SynG dataset in these figures are designated by a star, the 8 self-inconsistent QoI (excluded from the dataset, Table 3) are colored red and those excluded with VCM (Figures 1 and 2) are colored green.

The visual observation is that all the optimized models seem to perform with about the same overall quality: some models do better for one set of conditions, while other are closer to other experimental data. The shock-tube ignition delay times show a larger variation between different models. The problem here could lie with the incomplete instrumental model used in the simulation of ignition phenomena, as it does not capture the "non-idealities" of shock-tube experiments with sufficient detail, or the development of a mild-ignition regime, which is not entirely driven by chemistry. These factors are especially under suspicion in the inconsistent ignition-delay targets. Generally, the laminar flame speeds are predicted better by all models, with all simulations falling within the uncertainties bounds of experimental observations, reflecting perhaps the higher experimental accuracy of the measurements.

Figures 4-6 demonstrate the benefits of optimization methods LS-F and 1N-F and generally of the B2B-DC methodology in comparison to the "conventional" optimization, LS-H, or performed in study [54].

V. Conclusions

An optimization-based framework B2B-DC of an automated data-centric infrastructure, Process Informatics Model (PrIMe) was applied to the syngas reaction mechanism analysis. For this purpose, a dataset was constructed based on pertinent experimental observations, chemical-kinetics model, and the associated uncertainties. The experimental Quantities of Interest (QoI) were selected through evaluation of ignition delay time and laminar flame speed uncertainties. The composed dataset was subjected to consistency analysis. One outcome of the analysis was identification of a set of experimental QoI that were most difficult or impossible to match with the model; they were removed from the dataset for future investigation. The final consistent dataset with 122 experimental QoI and 55 active variables was used for model optimization on the feasible parameter set. The optimized syngas models produced with B2B-DC framework demonstrated an improved agreement with the dataset QoI. The results of the present study, however, demonstrate that the LS-H optimization may miss some critical information of the model-data system. Only parameter optimization performed on the feasible set produces a reaction model which describes the experimental measurements not included in the analysis as well as experimental targets from used dataset. The obtained optimized parameter values indicated parameter inadequacy, and the correlation analysis highlighted the direction of possible parameter modifications and model improvement.

References

[1] Frenklach, M., "PrIMe," URL: http://primekinetics.org.

[2] Feeley, R., Seiler, P., Packard, A., and Frenklach, M., "Consistency of a Reaction Dataset," *The Journal of Physical Chemistry A*, Vol. 108, No. 44, 2004, pp. 9573–9583.

[3]Frenklach, M., Packard, A., Seiler, P., and Feeley, R., "Collaborative Data Processing in Developing Predictive Models of Complex Reaction Systems," *International Journal of Chemical Kinetics*, Vol. 36, No. 1, 2004, pp. 57–66.

[4]Russi, T., Packard, A., Feeley, R., and Frenklach, M., "Sensitivity Analysis of Uncertainty in Model Prediction," *The journal of physical chemistry. A*, Vol. 112, No. 12, 2008, pp. 2579–2588.

[5]Russi, T., Packard, A., and Frenklach, M., "Uncertainty Quantification: Making Predictions of Complex Reaction Systems Reliable," *Chemical Physics Letters*, Vol. 499, 1-3, 2010, pp. 1–8.

[6]Frenklach, M., Packard, A., and Feeley, R., "Optimization of Reaction Models with Solution Mapping," *Modeling of Chemical Reactions*, edited by R. W. Carr, 1st ed., Elsevier, Amsterdam, 2007, pp. 243-293.

[7]Seiler, P., Frenklach, M., Packard, A., and Feeley, R., "Numerical Approaches for Collaborative Data Processing," *Optimization and Engineering*, Vol. 7, No. 4, 2006, pp. 459–478.

[8]Frenklach, M., "Transforming Data into Knowledge—Process Informatics for Combustion Chemistry," *Proceedings of the Combustion Institute*, Vol. 31, No. 1, 2007, pp. 125–140.

[9]Slavinskaya, N. A., Riedel, U., Dworkin, S. B., and Thomson, M. J., "Detailed Numerical Modeling of PAH Formation and Growth in Non-premixed Ethylene and Ethane Flames," *Combustion and Flame*, Vol. 159, No. 3, 2012, pp. 979–995.

[10] Hedge, A.; Li, W.; Oreluk, J.; Packard, A.; Frenklach, M., Consistency analysis for massively inconsistent datasets in Bound-to-Bound Data Collaboration. In preparation.

[11]Atkinson, R., Baulch, D. L., Cox, R. A., Crowley, J. N., Hampson, R. F., Hynes, R. G., Jenkin, M. E., Rossi, M. J., and Troe, J., "Evaluated kinetic and photochemical data for atmospheric chemistry: Volume I - gas phase reactions of O_x, HO_x, NO_x and SO_x species," *Atmospheric Chemistry and Physics*, Vol. 4, 2004, pp. 1461–1738.

[12]Wang, H., You, X., Joshi, A. V., Davis, S. G., Laskin, A., Egolfopoulos, F., and Law, C. K., "USC Mech Version II. High-Temperature Combustion Reaction Model of H_2/CO/C1-C4 Compounds," URL: http://ignis.usc.edu/USC_Mech_II.htm.

[13]Miller, J. A., and Melius, C. F., "Kinetic and Thermodynamic Issues in the Formation of Aromatic Compounds in Flames of Aliphatic Fuels," *Combustion and Flame*, Vol. 91, No. 1, 1992, pp. 21–39.

[14]Kathrotia, T., Fikri, M., Bozkurt, M., Hartmann, M., Riedel, U., and Schulz, C., "Study of the H+O+M Reaction Forming OH*: Kinetics of OH* Chemiluminescence in Hydrogen Combustion Systems," *Combustion and Flame*, Vol. 157, No. 7, 2010, pp. 1261–1273.

[15]Baulch, D. L., "Evaluated Kinetic Data for Combustion Modeling: Supplement II," *Journal of Physical and Chemical Reference Data*, Vol. 34, No. 3, 2005, p. 757.

[16]Troe, J. Proc. Combust. Inst., 2000, 28, 1463–1469.

[17]Cohen, N.; Westberg, K. R. J. Phys. Chem. Ref. Data, 1983, 12, 531.

[18]Zsély, I. G.; Zádor, J.; Turányi, T. Proc. Combust. Inst., 2005, 30, 1273–1281.

[19]Sun, H., Yang, S. I., Jomaas, G., and Law, C. K., "High-pressure Laminar Flame Speeds and Kinetic Modeling of Carbon Monoxide/Hydrogen Combustion," Proceedings of the Combustion Institute, Vol. 31, No. 1, 2007, pp. 439–446

[20]Troe, J. J. Phys. Chem. 1975, 83, 114.

[21] Li, J., Zhao, Z., Kazakov, A., Chaos, M., Dryer, F. L., and Scire, J. J., "A Comprehensive Kinetic Mechanism for CO, CH_2O, and CH_3OH Combustion," *International Journal of Chemical Kinetics*, Vol. 39, No. 3, 2007, pp. 109–136.

[22] Davidson, D. F., and Hanson, R. K., "Interpreting Shock Tube Ignition Data," *WSSCI Fall 2003 Meeting*, University of California at Los Angeles, 2003.

[23] Petersen, E. L., and Hanson, R. K., "Nonideal Effects Behind Reflected Shock Waves in a High-pressure Shock Tube," *Shock Waves*, Vol. 10, No. 6, 2001, pp. 405–420.

[24] Petersen, E. L., Rickard, M. J. A., Crofton, M. W., Abbey, E. D., Traum, M. J., and Kalitan, D. M., "A Facility for Gas- and Condensed-phase Measurements Behind Shock Waves," *Measurement Science and Technology*, Vol. 16, No. 9, 2005, pp. 1716–1729.

[25] Petersen, E. L., and Hanson, R. K., "Measurement of Reflected-shock Bifurcation Over a Wide Range of Gas Composition and Pressure," *Shock Waves*, Vol. 15, No. 5, 2006, pp. 333–340.

[26] Dryer, F. L., and Chaos, M., "Ignition of Syngas/Air and Hydrogen/Air Mixtures at Low Temperatures and High Pressures: Experimental Data Interpretation and Kinetic Modeling Implications," *Combustion and Flame*, Vol. 152, 1-2, 2008, pp. 293–299.

[27] Davidson, D. F., and Hanson, R. K., "Recent Advances in Shock Tube/Laser Diagnostic Methods for Improved Chemical Kinetics Measurements," *Shock Waves*, Vol. 19, No. 4, 2009, pp. 271–283.

[28] Ihme, M., "On the Role of Turbulence and Compositional Fluctuations in Rapid Compression Machines: Autoignition of Syngas Mixtures," *Combustion and Flame*, Vol. 159, No. 4, 2012, pp. 1592–1604.

[29] Urzay, J., Kseib, N., Davidson, D. F., Iaccarino, G., and Hanson, R. K., "Uncertainty-quantification Analysis of the Effects of Residual Impurities on Hydrogen–oxygen Ignition in Shock Tubes," *Combustion and Flame*, Vol. 161, No. 1, 2014, pp. 1–15.

[30] Mansfield, A. B., and Wooldridge, M. S., "High-pressure Low-temperature Ignition Behavior of Syngas Mixtures," *Combustion and Flame*, Vol. 161, No. 9, 2014, pp. 2242–2251.

[31] Grogan, K. P., and Ihme, M., "Weak and Strong Ignition of Hydrogen/Oxygen Mixtures in Shock-tube Systems," *Proceedings of the Combustion Institute*, Vol. 35, No. 2, 2015, pp. 2181–2189.

[32] Kalitan, D. M., Mertens, J. D., Crofton, M. W., and Petersen, E. L., "Ignition and Oxidation of Lean CO/H2 Fuel Blends in Air," Journal of Propulsion and Power, Vol. 23, No. 6, 2007, pp. 1291–1301.

[33] Petersen, E. L., Kalitan, D. M., Barrett, A. B., Reehal, S. C., Mertens, J. D., Beerer, D. J., Hack, R. L., and McDonell, V. G., "New Syngas/Air Ignition Data at Lower Temperature and Elevated Pressure and Comparison to Current Kinetics Models," Combustion and Flame, Vol. 149, 1-2, 2007, pp. 244–247.

[34] Mertens, J. D., Kalitan, D. M., Barrett, A. B., and Petersen, E. L., "Determination of the Rate of $H+O_2+M \rightarrow HO_2+M$ (M=N2, Ar, H2O) from Ignition of Syngas at Practical Conditions," Proceedings of the Combustion Institute, Vol. 32, No. 1, 2009, pp. 295–303.

[35] Herzler, J., and Naumann, C., "Shock Tube Study of the Ignition of Lean CO/H2 Fuel Blends at Intermediate Temperatures and High Pressure," Combustion Science and Technology, Vol. 180, 10-11, 2008, pp. 2015–2028.

[36] Krejci, M. C.; Mathieu, O.; Vissotski, A. J.; Ravi, S.; Sikes, T. G.; Petersen, E. L.; Kérmonès, A.; Metcalfe, W.; Curran, H. J., Laminar flame speed and ignition delay time data for the kinetic modeling of hydrogen and syngas fuel blends. J. Eng. Gas Turbines Power 2013, 135, (2), 021503. 10.1115/1.4007737.

[37] Mansfield, A. B.; Wooldridge, M. S., High-pressure low-temperature ignition behavior of syngas mixtures. Combust. Flame 2014, 161, (9), 2242-2251. 10.1016/j.combustflame.2014.03.001.

[38] Mathieu, O.; Kopp, M. M.; Petersen, E. L., Shock-tube study of the ignition of multi-component syngas mixtures with and without ammonia impurities. Proc. Combust. Inst. 2013, 34, (2), 3211-3218. 10.1016/j.proci.2012.05.008.

[39] Vasu, S. S.; Davidson, D. F.; Hanson, R. K., Shock tube study of syngas ignition in rich CO2 mixtures and determination of the rate of $H + O_2 + CO_2 \rightarrow HO_2 + CO_2$. Energy Fuels 2011, 25, (3), 990-997. 10.1021/ef1015928.

[40] Goswami, M., Derks, S. C., Coumans, K., Slikker, W. J., Andrade Oliveira, M. H. de, Bastiaans, R. J., Luijten, C. C., Goey, L. P. H. de, and Konnov, A. A., "The Effect of Elevated Pressures on the Laminar Burning Velocity of Methane+Air Mixtures," *Combustion and Flame*, Vol. 160, No. 9, 2013, pp. 1627–1635.

[41] Egolfopoulos, F. N., Hansen, N., Ju, Y., Kohse-Höinghaus, K., Law, C. K., and Qi, F., "Advances and Challenges in Laminar Flame Experiments and Implications for Combustion Chemistry," *Progress in Energy and Combustion Science*, Vol. 43, 2014, pp. 36–67.

[42] Natarajan, J., Lieuwen, T., and Seitzman, J., "Laminar Flame Speeds of H_2/CO Mixtures: Effect of CO_2 Dilution, Preheat Temperature, and Pressure," *Combustion and Flame*, Vol. 151, 1-2, 2007, pp. 104–119.

[43] Hassan, M. I., Aung, K. T., and Faeth, G. M., "Properties of Laminar Premixed CO/H/Air Flames at Various Pressures," *Journal of Propulsion and Power*, Vol. 13, No. 2, 1997, pp. 239–245.

[44] Natarajan, J., Kochar, Y., Lieuwen, T., and Seitzman, J., "Pressure and Preheat Dependence of Laminar Flame Speeds of H_2/CO/CO_2/O_2/He Mixtures," *Proceedings of the Combustion Institute*, Vol. 32, No. 1, 2009, pp. 1261–1268.

[45] Sun, S.; Meng, S.; Zhao, Y.; Xu, H.; Guo, Y.; Qin, Y., Experimental and theoretical studies of laminar flame speed of CO/H2 in O2/H2O atmosphere. Int. J. Hydrogen Energy 2016, 41, (4), 3272-3283. 10.1016/j.ijhydene.2015.11.120.

[46] Lapalme, D.; Seers, P., Influence of CO2, CH4, and initial temperature on H2/CO laminar flame speed. Int. J. Hydrogen Energy 2014, 39, (7), 3477-3486. 10.1016/j.ijhydene.2013.12.109.

[47] Xie, Y.; Wang, J.; Xu, N.; Yu, S.; Huang, Z., Comparative study on the effect of CO2 and H2O dilution on laminar burning characteristics of CO/H2/air mixtures. Int. J. Hydrogen Energy 2014, 39, (7), 3450-3458. 10.1016/j.ijhydene.2013.12.037.

[48] Weng, W. B.; Wang, Z. H.; He, Y.; Whiddon, R.; Zhou, Y. J.; Li, Z. S.; Cen, K. F., Effect of N2/CO2 dilution on laminar burning velocity of H2–CO–O2 oxy-fuel premixed flame. Int. J. Hydrogen Energy 2015, 40, (2), 1203-1211. 10.1016/j.ijhydene.2014.11.056.

[49] Zhang, Y.; Shen, W.; Fan, M.; Zhang, H.; Li, S., Laminar flame speed studies of lean premixed H2/CO/air flames. Combust. Flame 2014, 161, (10), 2492-2495. 10.1016/j.combustflame.2014.03.016.

[50] Xie, Y.; Wang, J.; Xu, N.; Yu, S.; Zhang, M.; Huang, Z., Thermal and chemical effects of water addition on laminar burning velocity of syngas. Energy Fuels 2014, 28, (5), 3391-3398. 10.1021/ef4020586.

[51] Kee, R. J., Rupley, F. M., and Miller, J. A., "CHEMKIN-II: A FORTRAN chemical kinetics package for the analysis of gas-phase chemical kinetics," SAND89-8009B, UC-706; Sandia National Laboratories: Albuquerque, NM, 1993.

[52]Kintech Lab Ltd., "Chemical Workbench®," Software Package, URL: http://www.kintechlab.com/.

[53]You, X., Russi, T., Packard, A., and Frenklach, M., "Optimization of Combustion Kinetic Models on a Feasible Set," *Proceedings of the Combustion Institute*, Vol. 33, No. 1, 2011, pp. 509–516.

[54] Varga, T.; Olm, C.; Nagy, T.; Zsély, I. G.; Valkó, É.; Pálvölgyi, R.; Curran, H. J.; Turányi, T., Development of a joint hydrogen and syngas combustion mechanism based on an optimization approach. Int. J. Chem. Kinet. 2016, 48, (8), 407-422. 10.1002/kin.21006.

FLASH PYROLYSIS OF SHUBARKOL COAL IN A CFB REACTOR FOR SEMI-COKE PRODUCTION

Diyar Tokmurzin, Kalkaman Suleymenov, Berik Aiymbetov, Yerbol Sarbassov, Myung Won Seo, Desmond Adair

Abstract

Fast pyrolysis characteristics of Shubarkol coal for semi-coke production are investigated using laboratory scale wire mesh reactor (WMR) and circulating fluidized bed reactor (CFB) experiments. Evolved gas from the WMR experiments at 400^OC, 600^OC, 800^OC, 1000^OC was analyzed using gas chromatography. Gases evolved at 1000^OC has composition consisting of 53.0% CO, 17.4% CH_4, 4.35% C_2H_4 and 1.74% C_2H_6. For CFB experiments, a 6 meters high laboratory scale atmospheric CFB reactor was constructed. CFB experiments were conducted at the range between 750 and 1000^OC. Semi-coke samples have volatiles content below V^{ar}=5%.

Introduction

Kazakhstan has the 8th largest coal reserves in the world, but coal export is limited due to the coals high ash content and unavailability of sea routes. The coal industry however fully satisfies the local coke demand in metallurgy. Almost all coal is mined in open pit coal mines, except coking coals from Karagandy, and Shubarkol coal is mined from open pit mines located in Central Kazakhstan. Shubarkol coal is used as a fuel for household heating, in industrial processes, in metallurgy, and is also exported. Currently most of the coke for metallurgy throughout the world is produced using coke oven batteries and semi-coke production for ferroalloy plants in Kazakhstan is also produced this way. Despite low ash and moisture, Shubarkol coal doesn't have caking properties like Karagandy coal. Caking and sintering of coal can cause defluidization in fluidized bed boilers, and therefore Karagandy coal, unlike Shubarkol coal, can't be processed to semi-coke in CFB reactors. Semi-coke for Aksu and Aktobe Ferroalloy plants can theoretically be produced alternatively, using CFB flash pyrolysis. This study examines the possibility of producing semi-coke in CFB installations, including a series of experiments to determine the release of volatile gases using wire mesh reactor experiments and CFB reactor experiments.

Experiment

Before the WMR and CFB reactor experiments, Shubarkol coal samples were ground using a mill (RM 200 series, Retsch, Germany) and then sieved through a 200 micrometer sieve using an automatic sieve (AS200, Retsch, Germany). Then the coal samples were analyzed using an proximate analyzer (5E-MAC IV, CKIC, China), elemental CHNSO analyzer (5E-CHN2200, CKIC, China), automatic calorimeter (5E-CS500, CKIC, China) and ash fusion determinator (5E-AF400, CKIC, China).

The wire mesh reactor used in this research previously has been used by H.W.Ra *et al*. [1]. Figure 1 illustrates the WMR involved in the flash pyrolysis experiments with Shubarkol coal. The

WMR uses electric current to heat the sample to a necessary temperature, and the apparatus consists of four main blocks: power supply, mass flow controller, wire mesh reactor, and a system for collection of gas and tar samples. The Shubarkol coal sample was first ground and then sieved through 200-micrometre sieve.
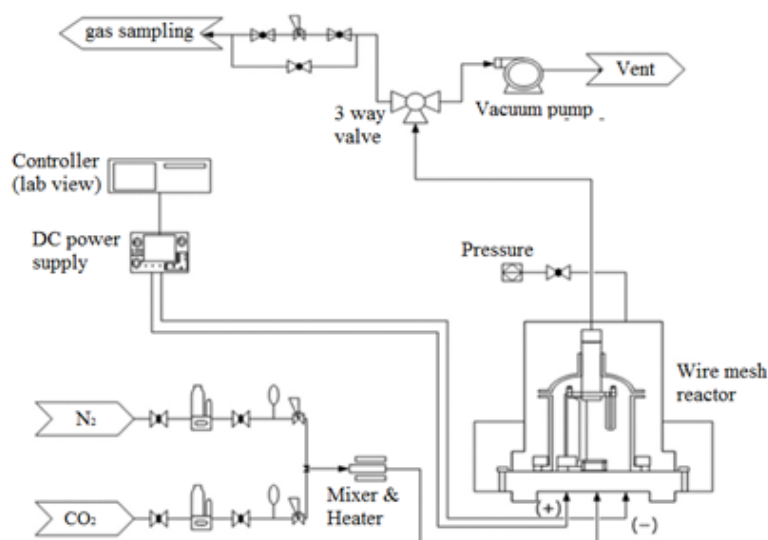
Figure 3. Wire mesh reactor [6].

The steel wire mesh, glass wool tar trap, and sample itself were weighed as well as ~20 mg of a coal sample which was located between two layers of wire mesh wrap. Wire mesh has a square shape with size 76 mm to 20 mm and mesh open size 75 micron, mesh is made of SS 316L steel which is most widely used in such experiments [2][3][4][5].The wire mesh with the coal sample was put on a copper sample holder which also serves as electric clamp. After the experimental apparatus assembled, nitrogen was purged inside in order to displace air from the chamber and nitrogen is filled into the cooling jacket.

Once the air was removed, a constant flow of nitrogen necessary for the experiment was purged inside (3 Lmin^{-1} or 0.08 m/s). During repeated experiments the wire mesh was heated to 400 ^{o}C, 600 ^{o}C, 800 ^{o}C, and 1000 ^{o}C. Nitrogen sweep gas cooled the sample and transported the evolved gases to the gas outlet where it passed through the tar trap glass wool and went into the gas sampling bag.

Collected gas samples were analyzed using a gas chromatograph, Agilent GC7890, that has flame ionization detector (FID) and thermal conductivity detector (TCD). Glass wool was weighed before and after the experiment to determine the amount of tar captured. The wire mesh and coal weighed separately before the experiment and wire mesh with ash-char particles weighed after the experiment. For accurate measurements high precision scales with 0.01 mg resolution, model XP205 Mettler Toledo, was used.

The CFB reactor involved in the research is depicted on the figure 2. The CFB unit has a 6 m high riser section with 160 mm inner diameter. Fast fluidized bed occurs in the riser section. Riser section is then continued with a cyclone for particle-gas separation, cyclone down-comer takes the circulating material particles down to the loop seal. The loop seal consists of two chambers with a bubbling fluidized bed.

Coal and inert materials are supplied to the riser using two screw feeders, and preheated air, steam, and oxygen are supplied to the riser bottom. The main fluidizing gas, air, comes from the bubble caps located in the bottom of the riser. Secondary air for the bubbling fluidized bed in the loop seal is also injected through bubble caps located at the bottom.
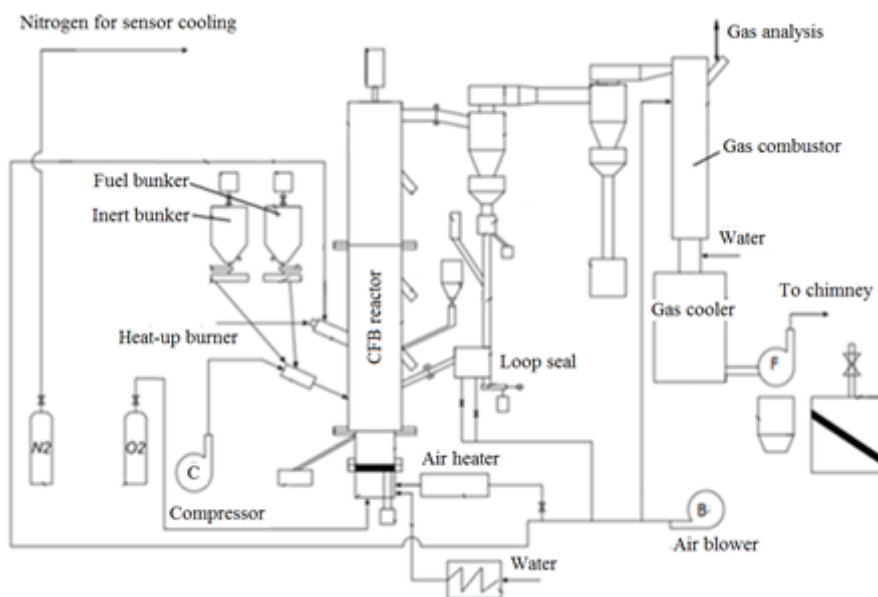
Figure 4 Circulating fluidized bed reactor located at Nazarbayev University

Results and discussion

Figure 3 presents results of gas chromatography analysis of evolved gases from the WMR reactor experiments at 400, 600, 800, 1000°C. Gas chromatography analysis demonstrates that pyrolysis of Shubarkol coal at lower temperatures (400°C, 600°C) produce nearly CO_2 only, whilst at higher temperatures (800°C, 1000°C) CO, CH_4, C_2H_4, C_2H_6 gases were detected in considerable concentrations. With an increase of temperature, products such as gas, volatiles and tar has a tendency to rise. Counter to this the amount of char decrease.
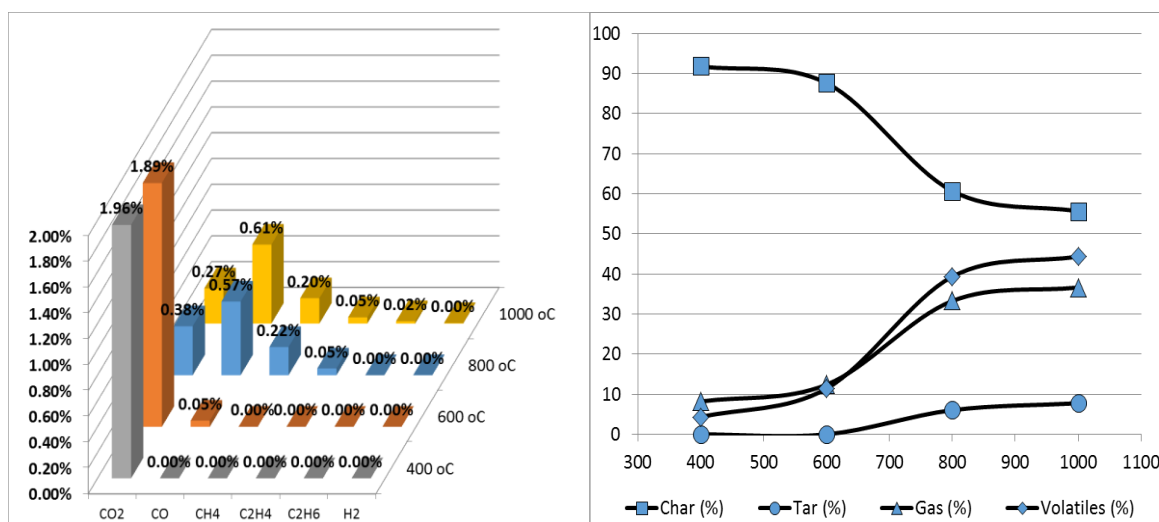
Figure 5. WMR evolved gases concentrations (left), mass balance of WMR products (right)

Figure 4 demonstrates volatiles concentrations of char samples extracted from the riser and from the loop seal by manually opening a ball valve and using a screw feeder. In general, with an increase of the bed temperature, volatiles concentration fells to acceptable levels above 900°C.
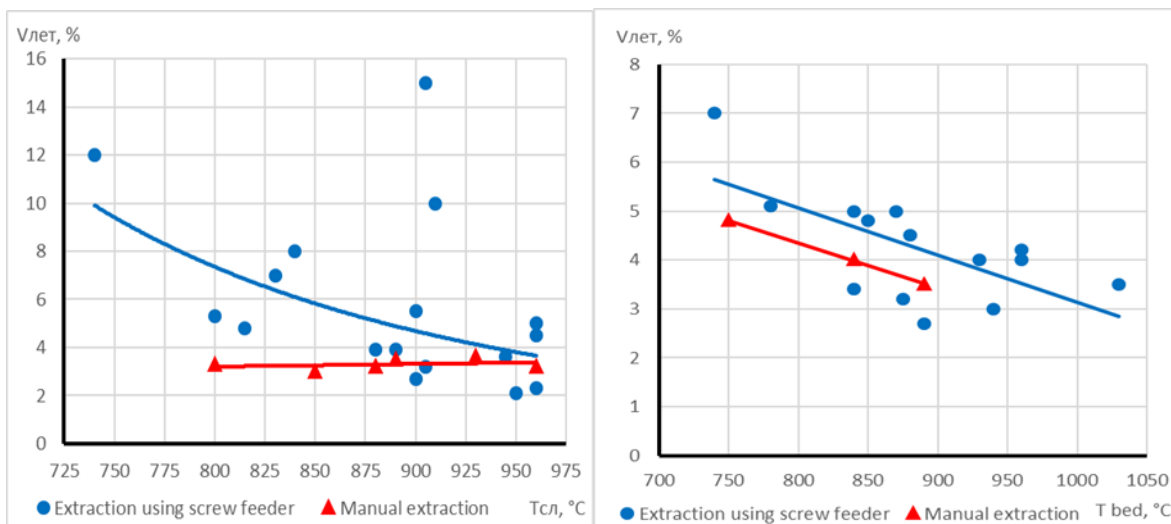
Figure 6. CFB experiments results. Dependence of volatiles concentrations to temperature in char extracted from the riser (left) and from the loop seal (right)

Conclusion

The WMR reactor experiment char yield demonstrates that flash pyrolysis of Shubarkol coal can produce semi-coke for metallurgical applications. The WMR experiments also indicate that keeping temperatures above 800°C is beneficial due to higher yield of combustible gases and volatiles. CFB experiments demonstrate that this technology is feasible for production of semi-coke with volatiles mass concentrations below 4% at temperatures above 900 ^{o}C. However, additional experiments involving gas analysis are required to estimate opportunities to integrate downstream processes for energy production

References

1. Ho Won Ra, Myung Won Seo, Sang Jun Yoon, Sung Min Yoon, Jae Kwon Kim, Jae Goo Lee, Seung Bin Park. Korean Journal of Chemical Engineering. September 2014, Volume 31, Issue 9, pp 1570–1576
2. D.B. Anthony, J.B. Howard, H.C. Hottel, and H.P.Meissner. Fuel, 55, 121 (1976)
3. S.Niksa, W.B.Russell, and D.A.Saville, Fuel, 61, 1207 (1982)
4. C.Sathe, J.I. Hayashi and C.Z.Li, Fuel, 81, 1171 (2002),
5. J.R.Gibbins, R.A.V.King, R.J.Woods, and R.Kandiyoti. Review of scientific instruments, 60, 1129 (1989)
6. Ra, H.W., Seo, M.W., Yoon, S.J. et al. Korean J. Chem. Eng. (2014) 31: 1570. doi:10.1007/s11814-014-0061-z

NANOPOROUS NI ANODE AND YSZ ELECTROLYTE FOR SOLID OXIDE FUEL CELLS

A.G. Umirzakov, A.L. Mereke, R.E. Beisenov, D.A. Muratov, B.A. Rakymetov

Laboratory of EPR Spectroscopy, LLP 'Institute of Physics and Technology', 11 Ibragimova st., Almaty, Kazakhstan, info@sci.kz

Abstract

The process of obtaining a porous nickel anode by pressing nickel and aluminum powders is shown. Further sintering of the samples and etching of aluminum from the obtained anode structure. The electrolyte is sputtered by pulsed laser deposition. SEM and EDS analysis were obtained.

Introduction

Solid oxide fuel cells (SOFCs) have the potential to be one of the cleanest and most efficient energy technologies for direct conversion of chemical fuels to electricity. Economically competitive SOFC systems appear poised for commercialization, but widespread market penetration will require continuous innovation of materials and fabrication processes to enhance system lifetime and reduce cost [1]. As the operating temperature decreases, the phase-to-phase polarization between the electrolyte and the electrodes increases dramatically [2]. Thus, the development of new electrode materials with unique porous structure close to the nanometer level is one of the most important issues in the development of a new generation SOFC's. The method of selective etching of additional material in a nickel anode is simple and effective
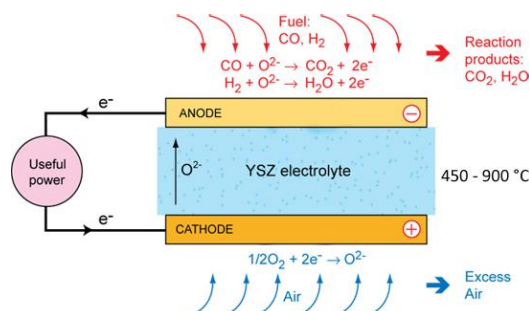
Figure 1. Scheme of an SOFC illustrating also the working principle

Solid oxide fuel cells (SOFCs) convert chemical energy with high efficiency directly into electricity and heat. It can operate on a variety of fuels such as natural gas or hydrogen [2, 4]. As shown in fig. 1, the fuel supplying H_2 is fed into the anode compartment where it is oxidized, and the electrons released as a result are conducted to an external circuit [3, 7]. The reaction products on the anode side of an SOFC are mainly water and CO_2. Air enters on the cathode side and oxygen is reduced here to O_{2-} by reaction with electrons from the external circuit. The O_{2-} ions can travel through the ion-conducting and gas-tight electrolyte, which separates the anode compartment from the cathode compartment [5, 6].

Main part

The porous nickel anode is fabricated using a Ni and Al powders mixing method followed by pressing and heat treatment. Very pure Ni and Al powders of 99.99% purity were used in the work. The ratio Ni and Al components was 60: 40%. The anode basis possesses a high porosity which is required for efficient delivery of fuel to the cell. Hot pressing method was used for obtaining tablet from nickel and aluminum powders. Next two steps was sintering of the sample and etching out aluminum from the anode structure. The mixing and grinding of the smallest powder with uniform dispersion is achieved by means of a grinding process in a SPEX SamplePre 8000M ball mill.

Full experimental process of fabrication a porous nickel anode with a flat nanoporous surface shown in fig. 2a, by thoroughly mixing commercial nickel powder (particle size between 0,5-1 μm) with an aluminum (particle size of from 100 to 300 nm) proppant. The mixing of the two components must be thorough; therefore, it is typically performed by mechanical mixing and ball milling procedures. The resulting mixture (nickel powder and proppant) is then pressed into a parallel faced ≈1 mm thick square tablet at 5000 psi (see figure 2b). The tablets pressed into round shape form as shown in insert of figure 2b. The tablet of pressed nickel powder/proppant is then loaded into a high temperature tubular furnace and sintered at 800 °C for 2 h in an ambient hydrogen atmosphere.

Next step of research was electrochemical dealloying of aluminum from the alloy of Ni-Al powders, as the potential increased, the amount of etched Al also increased. Passivation of nickel occurs with an increase in time, which contributes to the formation of NiO. The etching was carried out in a 30% KOH solution at room temperature. The process was carried out in two electrode cells, and under the action of ultrasound. A sample of Ni-Al alloy is used as a working electrode.
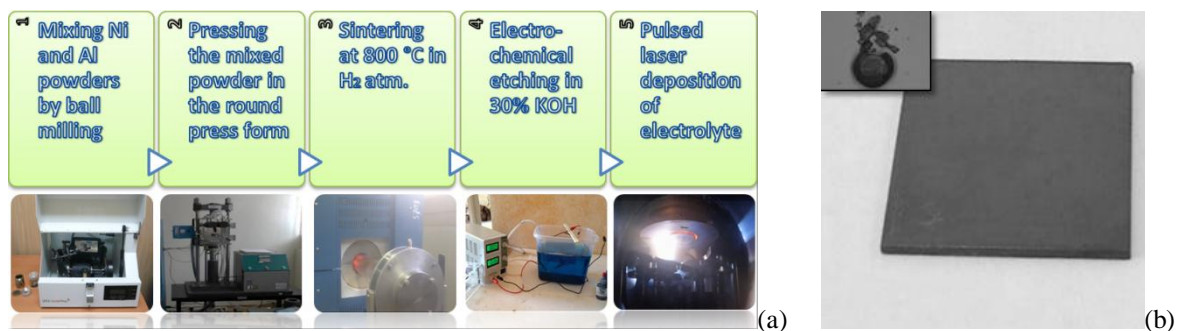
Figure 2. a) Schematic diagram for the porous nickel anode fabrication process,
b) The fabricated porous nickel anode 10x10 mm.

Surface SEM images were carried out for the fabricated porous nickel anode after sintering (figure 3a,b). These images show clearly the surface and bulk porous structure of the nickel anode, with pore sizes of 100 nm − 1 μm. This large pore size allows the fuel to readily reach the anode/electrolyte interface.
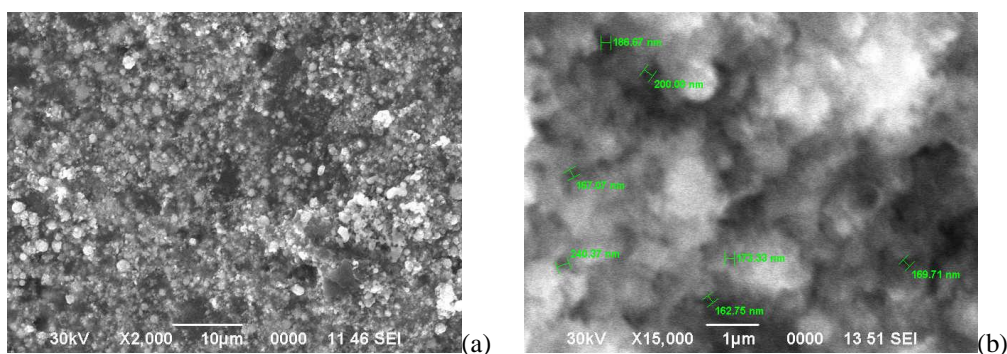
Figure 3. SEM images of the fabricated porous nickel anode.
a) Anode surface directly after sintering at 800 °C for 2 h.;
b) Anode surface after electrochemical etching;

The nickel surface treatments were applied to produce not only a flat surface, but also a surface with small pores (size < 500 nm) (see figure 4a,b) such that a continuous thin film electrolyte could be deposited and exhibit both gas and electrical hermeticity. The now smooth surface of the fabricated nickel anode will permit the deposition of a 3 μm thick smooth, continuous electrolyte yttria-stabilized zirconia (YSZ) film, which is not only an electrolyte layer, but one that effectively blocks hydrogen from reaching the SOFC cathode.

A 248 nm KrF Excimer laser at 7 Hz and 380 mJ was used to deposit the electrolyte layer on the porous nickel anode surface [2]. In this work, a dense YSZ electrolyte layer (about 1-2 μm thick) deposited at 150 mTorr and 650 °C in an atmosphere of 96% argon, 4% hydrogen to avoid nickel oxidation.

Surface and cross-sectional SEM images were carried out for the fabricated porous nickel anode after pulsed laser deposition (figure 4a,b). As we can see from images the deposition of a thin (0.5–3 μm), smooth, and pore free electrolyte will not allow the diffusion of both fuel and air.
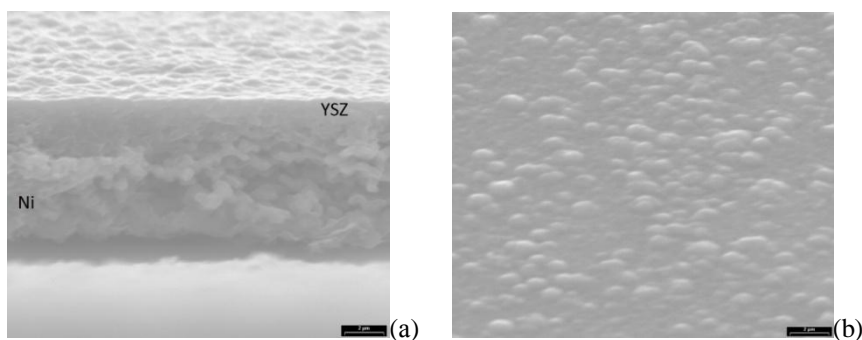
Figure 4. SEM cross-section images of the fabricated porous nickel anode with electrolyte layer,
a) Anode cross-section after electrolyte deposition b) Electrolyte surface after deposition.

Memo	O	Al	Ni	Total(mass%)
6	6.62	39.94	53.44	100
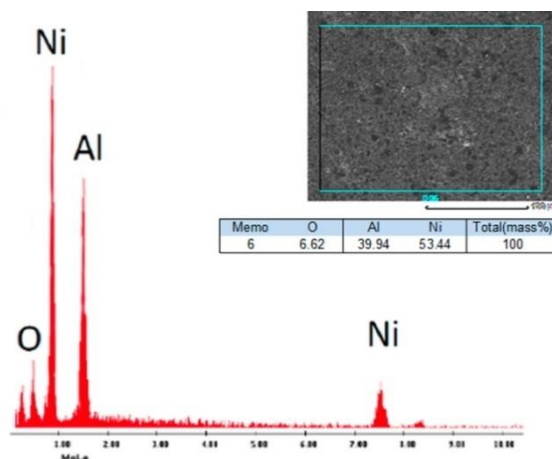
Figure 5. EDS analysis of anode after sintering

Conclusion

The porous nickel anode obtained by process of pressing nickel and aluminum powders, sintering and etching of aluminum from the obtained anode structure. The pore size between 100 – 500 nm, which allows for the H_2 to passage thru the anode to YSZ electrolyte layer. The thin YSZ electrolyte layer is sputtered by pulsed laser deposition. SEM and EDS analysis were obtained.

Analysis shows the deposition of a thin (0.5–3 μm), smooth, and pore free electrolyte which will not allow the diffusion of both fuel and air. EDS analysis shows the correct ratio of the material after annealing in the furnace at 800˚C, the presence of oxygen due to the interactions after discharge from the furnace.

References

1. S.C. Singhal, K. Kendall, High Temperature Solid Oxide Fuel Cells: Fundamentals, Design and Applications, Elsevier Advanced Technology, Oxford, UK, 2003.;

2. R. Ebrahim,* M. Yeleuov, A. Ignatiev, 3D Porous Nickel Anode for Low Temperature Thin Solid Oxide Fuel Cell Applications // Advanced Materials Technologies, 2017;

3. Fergus B., Jeffrey W. Oxide anode materials for solid oxide fuel cells // Solid State Ionics, 2006. – Vol. 177(17-18). – P.1529-1541.;

4. Agarwal M., Kumar V., Malladi S., Balasubramaniam R. and Balani K. Effect of current density on the pulsed co-electrodeposition of nanocrystalline nickel-copper alloys // JOM, 2010.–Vol. 62. – No. 6. – P. 88-92.;

5. Lipilin AS, Neuimin AD, Palguev SF Investigation of hydrogen electrodes made by hot pressing in circuits with oxide solid electrolyte // IB "PPTEEE and TE". - 1975. - Issue. 2 (64). - P. 69-81.;

6. Korovin N.V. Fuel cells and electrochemical power plants. // M .: publishing house MPEI, 2005. 280 p.;

7. Lynd L.R., Cushman J.H., Nichols R.J., Wyman C.E. Fuel ethanol from cellulosic biomass // Science, 1991. – Vol. 25. –P. 1318–1323.

FABRICATION OF YSZ TARGETS BY HOT PRESSING METHOD FOR PULSED LASER DEPOSIT INSTALLATION

A.G. Umirzakov[1], A.L. Mereke[1], R.E. Beisenov[1], R. Ibrahim[2], D.A. Muratov[1], B.A. Rakymetov[1]

[1]Laboratory of EPR Spectroscopy, LLP 'Institute of Physics and Technology', 11 Ibragimova st., Almaty, Kazakhstan, info@sci.kz;
[2]Center for Advanced Materials University of Houston, Houston, Texas 77204, rebrahim@Central.uh.edu

Abstract
The article describes a technique of the hot pressing yttrium stabilized zirconium target for use in a pulsed laser deposition of the electrolyte layer for solid oxide fuel cells. It is shown analytical studies and the results of the research (SEM, AFM, EDX).

1. Introduction

Our choice of epitaxial thin-film formation of YSZ electrolyte film is due to the fact that traditional powder technologies (pressing with subsequent high-temperature sintering) make it possible to form layers with a thickness of 10 μm and above therefore it can't be used in developments in minimizing the thickness of functional FC layers [1, 3]. The pulsed laser deposition (PLD) is one of the most acceptable methods for depositing thin films because of process stability, the possibility of independent control of the main parameters of the depositing process,

and as a result, it possible to obtain homogeneous layer with required structural and operational characteristics, larger area [2]. An important role in the formation of the electrolytic layer during deposition process depends from fulfillment of all conditions in process of production of the target with all the technological cycles and the necessary parameters [4].

Treatment of ceramic materials by hot pressing is increasingly rises in laboratories and production, the reason that equipment and accessories become more affordable and cheaper [5]. In addition, the method of hot pressing has become widespread due to the development of nanotechnology and nanoindustry. Simultaneous influence of pressure and temperature on nanopowders allows for obtaining samples with a high density which close to maximum [6].

2. Main part

Hot pressing technology includes the following stages: 1 - Grinding; 2- Calcination; 3 - Sintering.

We've took Y_2O_3 and ZrO_2 powders with high purity (99.99%) from Aldrich Chemistry. For 1 tablet of the target it took 30 grams of ZrO_2 and Y_2O_3 (92:8%). For preparation of a fine-grained and uniform powder it was conducted grinding processes. Grinding was performed before and after each of calcination, three times for each of the samples. The grinding process was carried out on a spherical planetary mill SPEX SamplePre 8000M to obtain a small size powder.

Calcination

The process of calcination of the material below its melting point is performed to achieve specific reactions, such as changes in physical and chemical characteristics. Each sample passes calcination three times for 17-20 hours, at a temperature of 1100 °C in an oxygen atmosphere.

Sintering

Hot pressing is simultaneous application of the high temperature and compressive stress on material for combining fine-grained powders into partially or completely sintered structures [4]. The pressure increases the driving force of compaction, reducing the processing temperature which required for the sintering process. In addition, the hot pressing process results on overall grain sizes, for more precise control, of the microstructure and the flexibility of the functionality ceramic layer.

The ground mixture of Y_2O_3 and ZrO_2 powders placed in a mold, then into a hot pressing chamber, where the chamber is evacuated till a vacuum of 10-6 Torr. Heating was carried out in 3 stages:

1 – Heating up to 1200 °C with heating rate 25 degrees per minute (only 40 minutes);

2 - Holding the temperature 1200 °C (within 60 minutes);

3 - Cooling 5 °C per second (to room temperature).

After calcination and grinding (three times), the process of hot pressing was carried out. This is the process of compressing the powder into a special form, followed by heating up to 1200-1400°C. The product is a solid oxide target (Figure 1). Yttria stabilized zirconia (YSZ) was sintered under a pressure of 2 tons, at a temperature of 1200 °C, sintering time was 60 minutes.

In addition of good ionic conductivity, the YSZ target should have a high micro hardness, resistance to corrosion, low thermal conductivity, and chemical stability at high temperatures [5].

Figure 2a shows the surface of the YSZ layer deposited via the pressed YSZ target on the Si (100) substrate at 35 Hz and 600 °C. The high frequency of the laser pulses leads to the formation of a surface with inhomogeneous particle sizes on the surface.
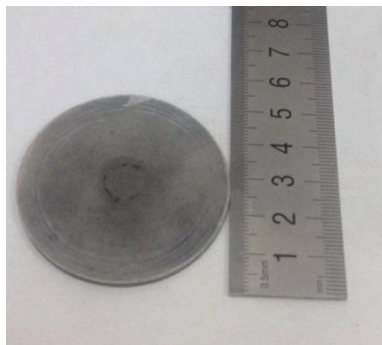
Figure 1 - Solid oxide target for pulsed laser deposition
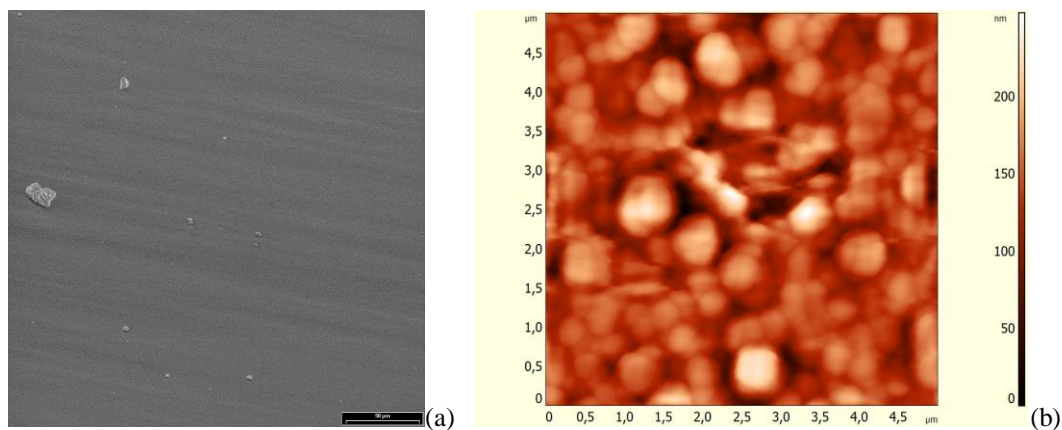
Figure 2 - a) SEM image of the YSZ layer deposited by the PLD, b) The AFM image of the YSZ layer

The surface and dimensions of the crystallites on deposited YSZ layer was analyzed with the Solver PRO M atomic force microscope (NT MDT) (Figure 2b). Due to the high roughness, the specimen was analyzed by the contact method. Scanning surface 5x5 µm has shown the formation of quasispherical particles of large diameter.

The EDX analysis (Figure 3) shows the correct ratio of components, which was originally set for the target. The content of 8% yttria in comparison with other components in the YSZ layer shows the possibilities of varying the properties of the electrolyte by changing the concentration of the main components.

3. Conclusion

The YSZ target was obtained by hot pressing at 1200 °C and a pressure of 2 tons. Powders of Y_2O_3 and ZrO_2 with a ratio of 8:92% were milled on a ball mill. The layers of thin-film electrolyte YSZ were deposited on silicon substrates at a temperature of 500-700 ° C, with a laser frequency of 35 Hz, and energy of 270-560 mJ. Morphology of the electrolytic layer was investigated by SEM and AFM. It shows formation of a rough surface with a large number of submicron particles, the formation of which is explained by the high frequency of the pulses of laser radiation. Elemental analysis of the deposited YSZ electrolyte layer revealed 8% of yttrium content in the structure, and zirconium is half the expected value, it can be explained by insufficiency of the energy for achieving the zirconium particles on the sample surface.
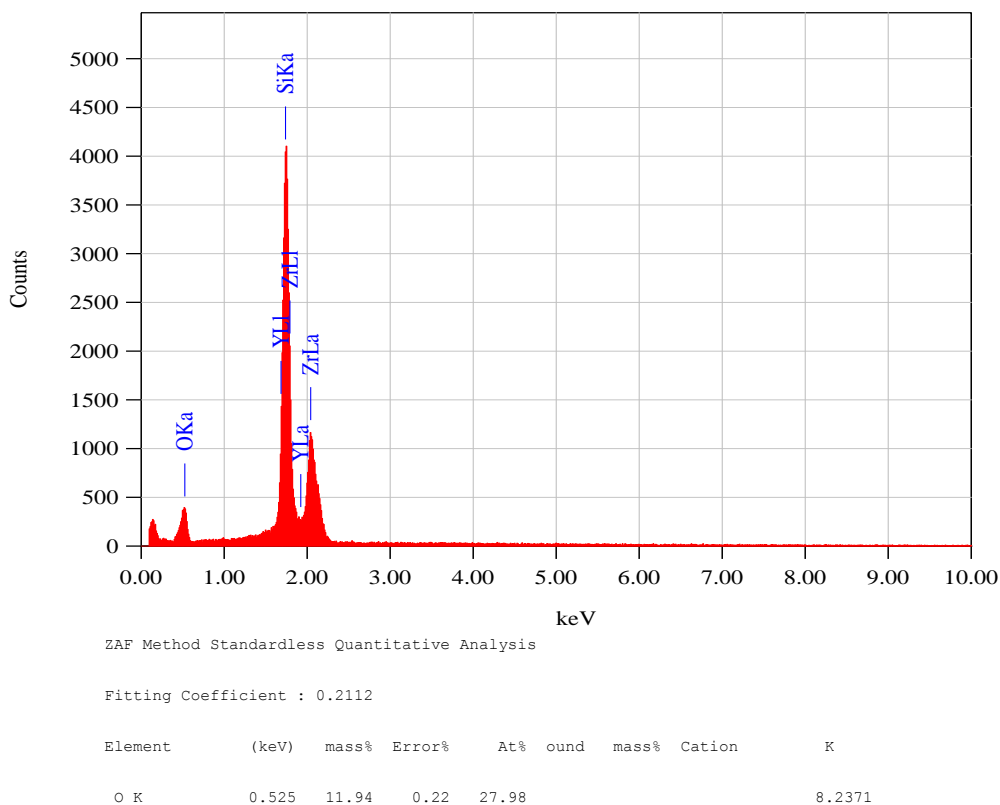
Figure 3 - EDX analysis of the YSZ layer deposited by the PLD

References

1 Lynd LR, Cushman JH, Nichols RJ, Wyman CE: Fuel ethanol from cellulosic biomass // Science - 1991, 25:1318–1323.

2 Wang MQ, Huang HS: A full fuel-cycle analysis of energy and emissions impacts of transportation fuels produced from natural gas. 1999.

3 Kordesch KV, Simader GR: Environmental impact of fuel cell technology. Chem Rev 1995, 95(1):191–207.

4 (Eon Woo Park, Hwan Moon, Moon-soo Park, Sang Hoon Hyun Fabrication and characterization of Cu–Ni–YSZ SOFC anodes for direct use of methane via Cu-electroplating, International journal of hydrogen energy 34 (2009) 5537–5545).

5 R. Ebrahim,* M. Yeleuov, A. Ignatiev, 3D Porous Nickel Anode for Low Temperature Thin Solid Oxide Fuel Cell Applications // Advanced Materials Technologies, 2017;

6 Lipilin AS, Neuimin AD, Palguev SF Investigation of hydrogen electrodes made by hot pressing in circuits with oxide solid electrolyte // Issue. 2 (64). - P. 69-81.;

2-D NUMERICAL INVESTIGATION OF THE INFLUENCE OF FLYER THICKNESS ON FLYER VELOCITY DRIVEN BY ELECTRIC EXPLOSION

Wanjun Wang, Mingshui Zhu, Junjun Lv, Qiubo Fu, Yao Wang.

Institute of chemical materials, Chinese Academy of Engineering Physics. wangwanjun@caep.cn. No. 64. Mianshan Rd, Mianyang City, Sichuan Province, China

Abstract
By dividing the electrical explosion process into two stages, a 2-D simulation model is established to study the influence of the flyer thickness on the flyer velocity, and the mechanism is analyzed tentatively.

1. Introduction

High speed flyer driven by electric explosion has been used widely in the field of detonator and high pressure loading device. Under the condition that the structure parameters and materials are unchanged, the acceleration curve of the flyer mainly depends on the specific internal energy of the explosive product. For different circuit, the change law of the specific internal energy of explosive products is significantly different, inevitably leading to a completely different acceleration curve of the flyer. At an earlier time, the Gurney energy is introduced to calculate the acceleration curve of the flyer[1], in this model, all the energy is given to the explosive product instantaneously as initial condition, which leading to an acceleration curve significantly steeper than the experimental results. Schmit made an important modification to this model, and a more accurate result is obtained by introducing a modified, time-dependent energy deposition term[2], a disadvantage of the modified model is that this model is 1-D and the assumptions used in the model were not validated.

A "two-stage" flyer driven model is proposed, the influence of the flyer thickness on flyer velocity were studied using AUTODYN code, which can provide reference and guidance for the design of exploding foil initiation device.

2. Physical model

The physical model is shown in figure 1.

This model believe that although the internal energy begins to increase simultaneously at the moment the circuit is closed, but the internal energy deposited at the initial stage($t<t_c$) can only be used for raising the temperature of the exploding foil, melting, raising the temperature of the meilted exploding foil, while the volume of exploding foil remains constant until the specific internal energy per unit volume is accumulated to a critical level E_0 at $t=t_c$. The energy E_0 is released instantaneously at t_c and the flyer is violently pushed by shock wave and exploding product.
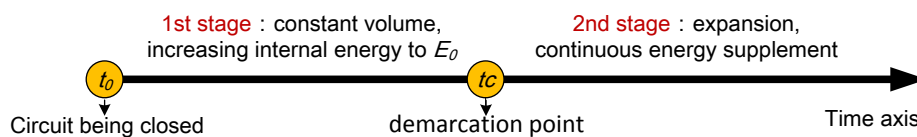

Fig.1 Schematic diagram of physical model

When t>t_c, additional energy is continuously deposited into the explosive product(expressed as $Q(t)$), helping resist the pressure attenuation and driving the flyer accelerate continuely, and the velocity curve is relatively gentle. Therefore, a inflection point can be finded in the velocity curve of the flyer driven by electric explosion.

The energy release at t_c is described by the CJ detonation model, The product is described by JWL equation of state, as shown in Equation 1.

$$P = A\left(1 - \frac{\omega}{R_1 V}\right)e^{-R_1 V} + B\left(1 - \frac{\omega}{R_2 V}\right)e^{-R_2 V} + \frac{\omega E}{V} \tag{1}$$

3. Numerical model

In this paper, the numerical simulation is carried out using AUTODYN, a 2-D axisymmetric model is established. The numerical model consists of backplane, exploding foil, flyer and barrel, as shown in figure 2. The material of the backplane is ceramic and has a thickness of 1 mm ; the material of the explosive foil is copper and has a thickness of 5 μm, the exploding foil is a circle with a diameter of 0.46mm; the material of the barrel is titanium alloy with a diameter of 0.6 mm; the material of flyer is polycarb and the thickness is set to be 20μm, 30μm and 40μm respectively.
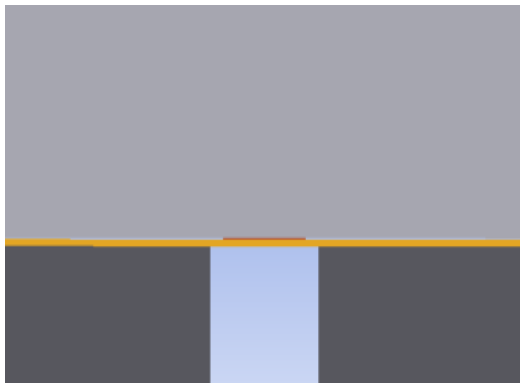
Fig.2 Simulation Model   Fig.3 Calculated and experimental velocity of the flyer
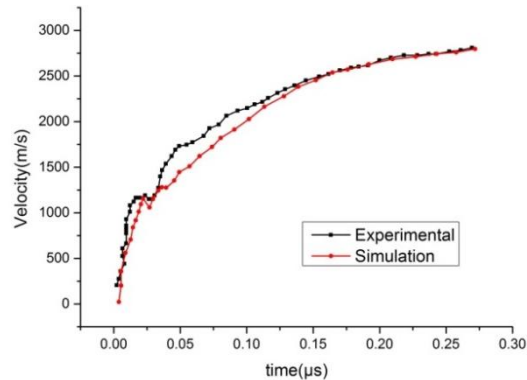
The JWL equation of state is adopeted for the exploding foil, and the parameters of the EOS are shown in table 1.

Table 1 Parameters of JWL EOS for exploding foil

ρ_0(g/cm³)	A(MBar)	B(MBar)	R1	R2	ω	E₀(MBar)	Pj(MBar)	D(m/s)
8.9	5.2423	0.17678	6.2	1.5	0.67	0.13	0.2431	2991

For the additional energy $Q(t)$ *after* t_c, "constant power" model is used as shown in formular(3), The parameters of this model are shown in Table 2

$$\frac{dQ(t)}{d(t)} = C_0 \tag{3}$$

Table 2 parameters of the model for additional energy

Q(J/Kg)	Begine time(μs)	End time(μs)
1.85E7	t_c	0.4

The comparison between the calculated and experimental velocity[3] of the flyer with the thickness of 30μm is shown in figure 3. As can be seen from the figure, the calculated results are in agreement with the experimental results before 0.03μs, but during 0.03μs~0.15μs, the error between numerical and experimental results is much more obvious. This is because the acceleration of the flyer after the velocity jump is mainly determined by the additional energy $Q(t)$. In a real electrical explosion, $dQ(t)/dt$ shows a trend of decreasing rapidly with time, so the acceleration also decreases with time correspondingly, while the "constant power" adopted in numerical simulation will certainly leads to an acceleration which is almost constant. In summary, the main reason for this error is that the additional energy $Q(t)$ added to the explosion product in numerical simulation is different from that in a real situation, and a modified $Q(t)$ can significantly improve the accuracy of the numerical result.

Flyer velocity with different thickness is shown in figure 16, the flyer velocity is 3195m/s, 2740m/s, 2599m/s at 0.25μs respectively, and the kinetic energy ratio is 1 : 1.10 : 1.32, that is, the kinetic energy increases with the increase of flyer thickness.
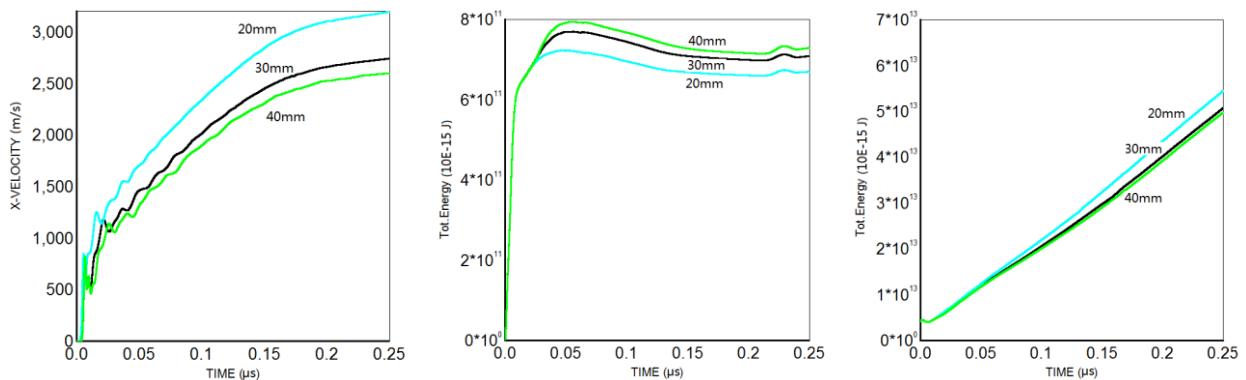
Fig.4 Flyer velocity Fig.5 Total energy of the backplane Fig. 6 Total energy of exploding foil

It can be seen from Fig. 5 and Fig. 6 that the total energy of the backplane increases with the increase of flyer thickness, while the total energy of the explosive foil decreases. This is due to the fact that more energy is needed for explosive product to push the flyer travelling for specific distance when the flyer is thicker, resulting in a smaller total energy of the explosive foil and a larger total energy of the backplane, which is very similar to the influence of the density of the flyer. Although the energy efficiency increases with the increase of flyer thickness, the increase amplitude decreases gradually. In the design of slapper detonator, make sure that the flyer thickness selected can achieve a balance between the transmitted wave pressure and the pulse width.

4. Conclusion

A 2-D simulation model is established to study the influence of flyer thickness on the flyer velocity. The conclusions are as follows:

1) This model can be used for numerical simulation of flyer driven by electric explosion, the calculated flyer velocity are consistent with the experiment results;

2) Increasing flyer thickness can help improve energy efficiency.

5. Reference

[1] Tucker T J, Stanton P L. 1975. Electrical gurney energy: new conception in modeling of energy transfer from electrically exploded conductors. SAND-75-0244 [R]. Albuquerque: Sandia National Lab.

[2] Schmidt S C, Seitz W L, Wackerle J. 1977. An empirical model to compute the velocity histories of flyers driven by electrically exploding foils, LA-6809 [R]. Los Alamos: Los Alamos Scientific Lab.

[3] Li Tao, Weng Jidong, Wang Zhiping, Zhang Jun. 2012. Velocity measurement of small flyers driven by electric explosion[C]. The 4th academic conference on explosion mechanics experiment technology.

NANOSCALE SnO$_2$ WITH WELL-DEFINED FACETS IMPROVING COMBUSTION PERFORMANCE OF ENERGETIC MATERIALS

Wen-gang Qu, Feng-qi Zhao, Hong-xu Gao

National Key Lab of Science and Technology on Combustion and Explosion, Xi'an Modern Chemistry Research Institute, East ZhangbaRoad 168, Xi'an 71065, Shaanxi Province, China
Email: cihswd@126.com

Abstract: Catalytic activity of SnO$_2$ nanocrystals with different percentages of the exposed [221] facets for the thermal decomposition of RDX was investigated. An enhancement in the catalytic activity was observed for the SnO$_2$ nanocrystals with a higher percentage of the exposed [221] facets.

Introduction

Energetic materials (EMs) contain and release a large amount of stored energy due to their chemical composition and molecular structure, as a result, are widely used in propellants, explosives, and pyrotechnics[1-3]. One of the most important impacts on the combustion process of EMs is the thermal decomposition process. Accordingly, a variety of catalysts have been studied for enhancing the thermal decomposition efficiency of the energetic materials[4-7]. For the traditional EMs, such as RDX, HMX and ammonium perchlorate (AP) et al., the primary exothermic process is the oxidation reaction in the gas phase, meaning that the gas-sensing semiconductor catalysts based on the oxidation–reduction reaction occurring on the semiconductor surface might exhibit excellent catalytic performance.

As the best known gas-sensing material, tin dioxide (SnO$_2$), has been widely used in photocatalytic, photovoltaic devices, gas sensing, and so on[8-12]. However, few works focus on the catalytic activity of SnO$_2$ for the thermal decomposition of EMs. In addition, according to the viewpoint of chemical activity, metal oxide nanocrystals with particular exposed crystal planes, such as high-index facets, may have good catalytic properties, due to the high densities of atom steps, ledges, kinks, and dangling bonds of high-index facets which exhibiting much higher chemical activity[13-16]. Recently, SnO$_2$ nanoparticles with exposed high-index facets have been prepared, and the correlation between exposed facets and photocatalytic/gas sensing properties has also been investigated[17]. Therefore, a good understanding of the correction between the exposed facets of SnO$_2$ and catalytic activity for RDX decomposition is essential to further enhance the catalytic performance.

In current work, we investigated the thermal decomposition process of RDX with different SnO$_2$ and propose a catalytic mechanism by studying the decomposition of RDX, in the presence of

SnO_2 additives. Further, we explored the application of nanostructured SnO_2 with well-defined facets in solid rocket propellant.

Result and discussion

Three kinds of SnO_2 nanostructures with different exposed facets have been synthesized using HCl as the face-controlling agent. SEM images of the as-prepared samples are shown in Figure 1 (a-c). It can be seen that the addition of HCl is crucial for the morphology of SnO2. Figure 1a shows the SnO_2 nanoparticles synthesized without adding HCl, exhibiting no regular morphology. When the volume ratio of HCl/solution is 1:15, the formed SnO_2 particles evolve into tetragonal nanorods with two pytamidal tips (Figure 1b). When the volume ratio of HCl/solution reaches to 1:10, the SnO_2 particles exhibit well-defined octahedral shape with with an edge-to-edge width of about 200 nm, and an apex-to-apex length around 300 nm (Figure 1c). Thus, the apex angle between two side surfaces can be calculated at 65.8°, which agree well with the model of octahedral SnO_2 enclosed by [221] facets projected along the [110] direction[17-19]. Figure 1d shows a typical powder X–ray diffraction (XRD) pattern of the as-prepared product, product can be indexed to the rutile phase of bulk SnO_2.
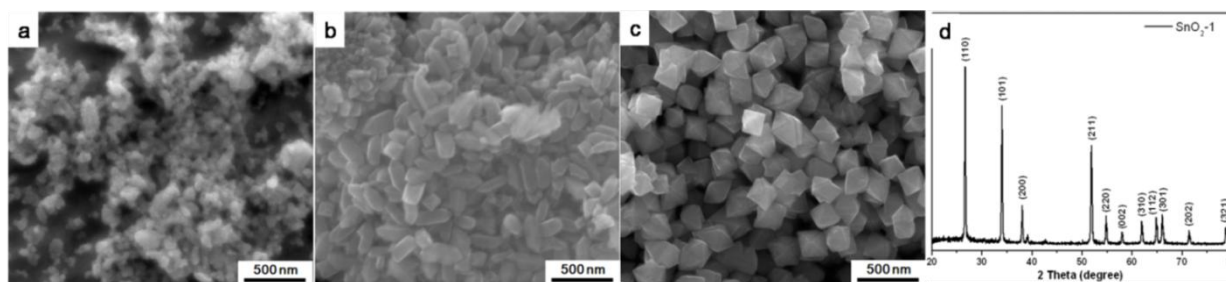
Figure 1 SEM images of the SnO_2 nanoparticles (a), nanorods (b), octahedral nanoparticles (c) and corresponding XRD patterns (d).

The effect of each SnO_2 additive on the thermal decomposition of RDX was studied by DSC analysis, carried out at 10 °C min^{-1} in sample pans with lids under a flow of argon. Samples of pure RDX and RDX mixed with each additive on a 2:1 by mass basis were prepared by grinding the powders with a mortar and pestle until homogeneous. Representative DSC curves of both pure RDX and the mixture of RDX with different SnO_2 additives are shown in Figure 2.
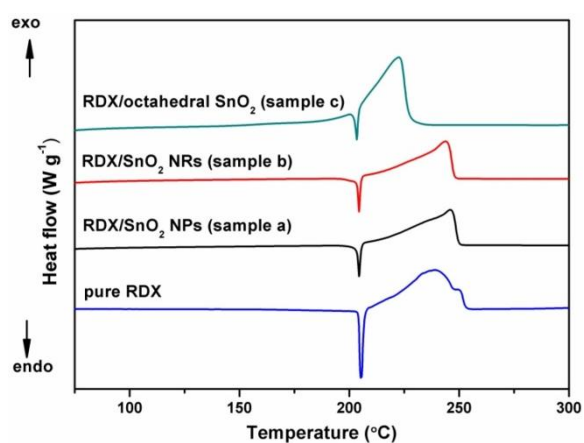
Figure 2 DSC curves for the decomposition of pure RDX and RDX with three kinds of SnO_2 additives.

All the four curves exhibit two thermal signals. The first endothermic peak at 204 °C is similar for each curve, which is due to the melting process of RDX[20]. A significant difference

between the additives observed on the decomposition is the obvious reduction of the decomposition temperature. The pure RDX exhibits two decomposition peaks: the liquid phase decomposition peak and gaseous decomposition. In the presence of SnO_2 nanoparticles, the liquid phase decomposition peak decreased and the gaseous decomposition temperature is reduced by 5 °C, 7 °C, and 28 °C. These results suggest that the SnO_2 catalyst can greatly promote the thermal decomposition of RDX, and Sample c with a higher percentage of exposed [221] facets shows much better catalytic activity for thermal decomposition of RDX than Sample a and b.

Given the enhanced activity of SnO_2 toward RDX decomposition, one could expect that it would also enhance the burning properties of solid rocket propellant. Figure 4 shows the burning rate curves for propellants with each catalysts, as calculated from three propellant strands burned throughout the pressure range. The green line belongs to the control propellants contained no catalysts. All three catalysts increased the burning rates relative to the control sample, and the propellants containing octahedral SnO_2 exhibited a broad burning rate plateau zone: the pressure exponent was 0.19 from 2–22 MPa. The plateau effect is a desirable feature for high burning-rate propellants. Typical propellant formulations that achieve a high burning rate by increasing the value of the pressure exponent are unstable due to their oversensitivity to pressure variations, which can lead to catastrophic failure. The octahedral SnO_2 provides the propellant with a high burning rate and broad plateau effect. The plateau observed may indicate that the surface reaction is rate-limiting but not diffusion-limited at pressures from 2–22 MPa, which should originate from the high active [221] facets of octahedral SnO_2.
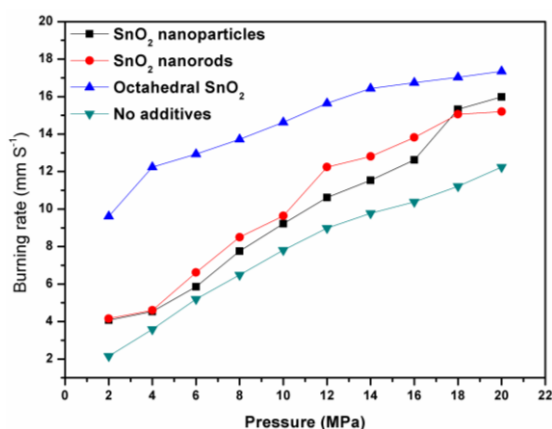
Figure 4. Curves of solid propellant burning rates vs pressure

Conclusion

In this study, SnO_2 nanocrystals with different percentages of the exposed [221] facets were applied in promoting the thermal decomposition of RDX. An enhancement in the catalytic activity for RDX decomposition was observed for SnO_2 nanocrystals with a higher percentage of the exposed [221] facets. Moreover, in the presence of octahedral SnO_2, the decomposition temperature of RDX was reduced by 28 °C. It is also confirmed by first-principles calculations that such highly exposed [221] facets can facilitate the formation of active oxygen which can lead to the oxidation reaction of RDX more completely in the catalytic decomposition process.

Our results emphasize that, through control over structure, the properties of SnO_2 can be made favorable for new and promising applications. Further work may lead to additives for safer and more efficient solid rocket propulsion or the ability to meet application-specific propellant requirements through the tailoring of additive structure on the nanoscale.

References
[1] Yen, N. H.; Wang, L. Y. *Propellants, Explosives, Pyrotechnics* **2012**, 37, 143.

[2]   Dreizin, E. L. *Prog. Energy Combust.* **2009**, 141, 35.
[3]   Slocik, J. M.; Crouse, C. A.; Jonathan E.; et al., *Nano. Lett.* **2013**, 13, 2535.
[4]   Xu, H.; Wang, X. B.; Zhang, L. Z. *Perchlorate. Powder Technol.* **2008**, 185, 176.
[5]   Li, L. P.; Sun, X. F.; Qiu, X. Q.; Xu, J. X.; Li, G. S. *Inorg. Chem.* **2008**, 47, 8839.
[6]   Wang, Y. P.; Zhu, J. W.; Yang, X. J.; Lu, L. D.; Wang, X. *Thermochim. Acta* **2005**, 437, 106.
[7]   Reid, D. L.; Russo, A. E.; Carro, R. V.; Stephens, M. A.; LePage, A. R.; Spalding, T. C.; Petersen, E. L.; Seal, S. *Nano Lett.* **2007**, 7, 2157.
[8]   Manjula P.; Satyanarayana, L.; Swarnalatha, Y.; et al., *Sens. Actuators* B **2009**, 138, 28.
[9]   Korotcenkov, G.; Cho, B. K.; Gulina, L.; Tolstoy, V. *Sens. Actuators B* **2009**, 138, 512.
[10]   Kumar, V.; Sen, S.; Muthe, K. P.; et al., *Sens. Actuators B* **2009**, 138, 587.
[11]   Chen, A. F.; Bai, S. L.; Shi, B. J.; et al., *Sens. Actuators B* **2008**, 135, 7.
[12]   Chen, Y. J.; Zhu, C. L.; Wang, L. J.; et al., *Nanotechnology* **2009**,20, 045502.
[13]   Zhao, L.; Chen, X.; Wang, X.; et al., *Adv. Mater.* **2010**, 22, 3317.
[14]   Tian, N.; Zhou, Z. Y.; Sun, S. G.; et al., *Science* **2007**, 316, 732;
[15]   Xie, X.W.; Li, Y.; Liu, Z. Q.; et al., *Nature* **2009**, 458, 746;
[16]   Hu, L. H.; Peng, Q.; Y. D. Li, *J. Am. Chem. Soc.* **2008**, 130, 16136.
[17]   Han, X. G.; Jin, M. S.; Xie, S. F.; et al., *Angew. Chem. Int. Ed.* **2009** , *48* , 9180 .
[18]   Ma, Y. Y.; Kuang, Q.; Jiang, Z. Y.; et al., *Angew. Chem. Int. Ed.* **2008**, 47, 8901;
[19]   Liao, H. G.; Jiang, Y. X.; Zhou, Z. Y. et al., *Angew. Chem. Int. Ed.* **2008,** 47, 9100.
[20]   Long, G. T.; Vyazovkin, S.; Brems, B. A.;Wight, C. A. *J. Phys. Chem. B* **2000,** *104*, 2570.
[21]   Kohl, D. *Sens. Actuators* **1989**, 18, 71.
[22]   Kinkawa, T.; Sakai, G.; Tamaki, J.; et al., *J. Mol. Catal.* A **2000**, 155, 193.

DIATOMITE: AN EMERGING BIOMATERIAL WITH HIERARCHICAL POROUS STRUCTURE IN NANOTECHNOLOGY AND ITS APPLICATION IN SYNTHESIS OF MULTIWALLED CARBON NANOTUBES BY CHEMICAL VAPOR DEPOSITION METHOD

[1,2]Zhalgasbaikyzy A., [2]Zhaparova A., [1]Nurgain A., [1,2]Nazhipkyzy M., [1,2]Mansurov Z.A.

1. Institute of Combustion Problems, 050012, Kazakhstan, Almaty, Str. Bogenbai Batyr, 172
2. Al - Farabi Kazakh National University, Kazakhstan, Almaty, Ave. al - Farabi, 71

Abstract
In this current work, MWCNTs was synthesized on catalyst system that prepared from natural biomaterial generated from single cell algae, called diatomite with unique nanoscaled morphologies and patterns and by immobilization of Ni, Co particles on to diatomite substrate. A new approach for obtaining MWCNTs by using silica diatomite with natural pores structure has been developed and employed.

Introduction

Nature has developed the unique biomolecular mechanism and process of assembly of biocompatibility capable to generate a set of biomaterials with unprecedented complexity and a set of the functionality and properties surpassing artificial production technologies[1,2]. This natural molecular process of self-assembly developed from millions of years of evolution is capable to create these unique biological structures with high precision and reproducibility in soft conditions

of the environment and lower consumption of energy. These biological materials attracted huge interests not only to a biomimetic of new nanostructural materials with difficult architecture and unique properties, but also as a source of the inexpensive natural materials ready to use with the minimum processing. The majority of live organisms, such as bacteria, seaweed, insects, plants, animals and people (bones), are capable to fabricate these types of inorganic structures or their organic composites into difficult architecture with ordered micro nanoscales features which it is impossible to reproduce by existing engineering or chemical synthetic processes[2,3]. Among them the exoskeletons of amorphous silicon dioxide (frustule) of one-chained seaweed called diatomite are one of the most impressive examples of biologically received nanostructural materials [4]. Each of the estimated 100 000 types of diatom and it has the special three-dimensional cover from silicon dioxide called by a frustule with the characteristic form decorated with the unique drawing of nanodimensional signs, such as time, ridges, thorns [5].

Recently the new term called by diatomite nanotechnology has been developed for the description of the new developing area for a research of these outstanding materials and their applications on various disciplines, including molecular biology, materials science, biotechnology, nanotechnology and photonics[6].

A number of potential applications for diatomite (dioxide of silicon) including optics, photonics, a catalysis, biosensors, delivery of drugs, molecular division, filtration, adsorption, bioencapsulation and immunoisolation and matrix synthesis nanomaterials have been offered and investigated[7,8].

It should be noted that diatomic dioxide of silicon can be received by cultivation the diatoms of seaweed in significant amounts, but their huge quantities from inexpensive fossilized the diatoms of the seaweed called by the diatomaceous earth, the white mineral powder consisting from clean diatomic frustules are available in thousands of tons from the mining industry.

So, in this current work, diatomite was applied as catalyst carrier for the synthesis of MWCNTs, because of high surface area of pores that could retention capacity of the deposited catalyst. MWCNTs were synthesized on catalyst system that prepared from natural diatomite with unique nanoscaled morphologies and patterns by immobilization of Ni, Co particles on to diatomite substrate. A new method for obtaining MWCNTs by using silica diatomite with natural pores structure has been developed and employed.

Experimental part

Diatomite earth sample was obtained from Aktobinsk region in western Kazakhstan. The raw diatomite powdered to 35 micron and used directly without any further purification. In the next step, catalyst solution from $NiNO_3 \cdot 6H_2O$ and $Co(NO_3)_2 \cdot 6H_2O$ salts with 0.5 M concentration were prepared and applied for further precipitation of Ni, Co particles on to diatomite substrate. After this step we fabricated support system with catalyst based on diatomaceous earth, which continuously applied to synthesis of multiwalled carbon nanotube via Chemical vapor deposition method.

While synthesis process, firstly argon gas supplied with $160 cm^3$/min yield at the 400 ^{0}C temperature and second propane was supplied at 800 ^{0}C with 55 cm^3/min inlet, after placing prepared catalyst system in boat.

Result and discussion

Raman spectroscopy is considered to be a very good method for CNTs presence; in addition it is used to characterize CNTs more precisely. The spectra of all the samples indicate the presence of carbon nanostructures of sp^2 hybridization with some degree of ordering.

The CNT samples obtained on a diatomite with a cobalt catalyst contain a certain fraction of the amorphous carbon phase, as indicated by the large width of the peaks, in comparison with the spectra of the remaining samples.

The position G of the peak in the range 1570-1580 cm^{-1} is characteristic for carbon nanostructures of the graphite group, and the shift to the low-frequency region is most characteristic of carbon nanotubes. The increase in the intensity of the 2D peak in the region 2710-2715 cm^{-1} indicates an increase in the orderliness of the structure of the material. While the peaks D at 1350-1360 cm^{-1} and G + D in the region of 2940 cm^{-1} arise as a result of the disorder of the structure.

The samples obtained on nickel practically do not contain an amorphous phase, which is expressed in the small width of the main Raman peaks. In addition, the ratio of the intensities of the peaks I (2D) / I (G) is much higher, compared with the spectra of the samples on cobalt, which indicates a fairly high degree of ordering of the sp^2 carbon structure under investigation. Analysis of the Raman spectra suggests that the samples obtained on the diatomite contain a greater number of multi-walled high-quality carbon nanotubes than in the shungite samples. This is confirmed by the lower intensity of the defective peaks D and D + G (Figure 1).
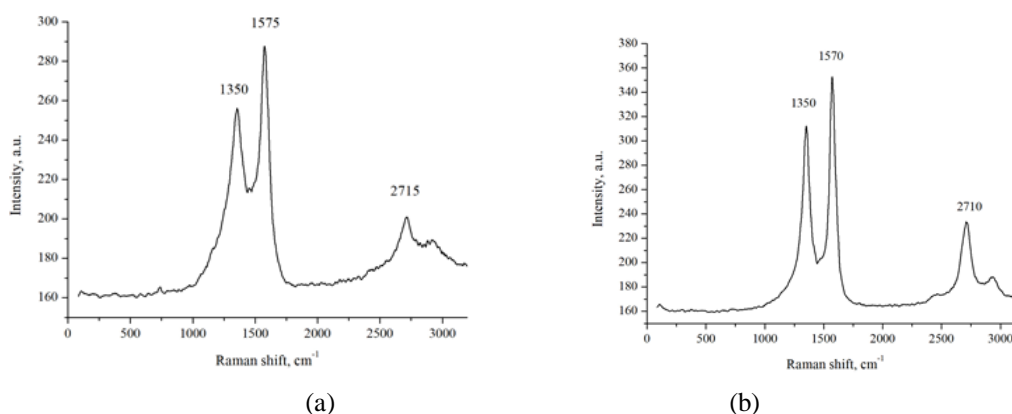

| (a) | (b) |

Figure 1.Raman spectrum of the CNTs prepared on diatomite by using Co based diatomite substrate (a) and Ni based diatomite substrate.

The resulting carbon nanotubes, before that pure natural diatom silica were examined using a scanning electron microscope, exactly Multifunction Scanning Electron Microscope Quanta 3D 200i. The SEM photographs with different magnification of remarkable pore morphologies and channels architectures of diatomite can be seen in Figure 2(a), (b). As you see, the diatomite earth has open pores in some structures, while some structures show us deep, several hierarchical pores. This variety of shapes and ordered porous structures demonstrate precision and uniqueness of natural design at the micro- and nano size, providing enormous opportunity to use this material for catalyst support function as it can be seen in figure 2 (c). Here, the growth of carbon nanotubes on diatom holes can be seen.

Conclusion

In this work, a novel approach was developed for one step synthesis CNTs on diatomite supported catalytic system by CVD method. The result of Raman spectroscopy revealed that the synthesized CNTs on both Co, Ni precipitated samples are multiwalled material, however the ratio of the intensities of the peaks I (2D) / I (G) is much higher, compared with the spectra of the samples on cobalt, which indicates a fairly high degree of ordering of the sp2 carbon structure under investigation. Similarly, obtained CNTs on Ni catalyst system shows better result than Co catalyst supported system.

Nowadays, we are working on improving, furthermore enhancing the quality and amount of CNTs on diatomite support. As well as, we are planning to investigate magnetic properties of CNTs on diatomite and then use in heavy metal removing.
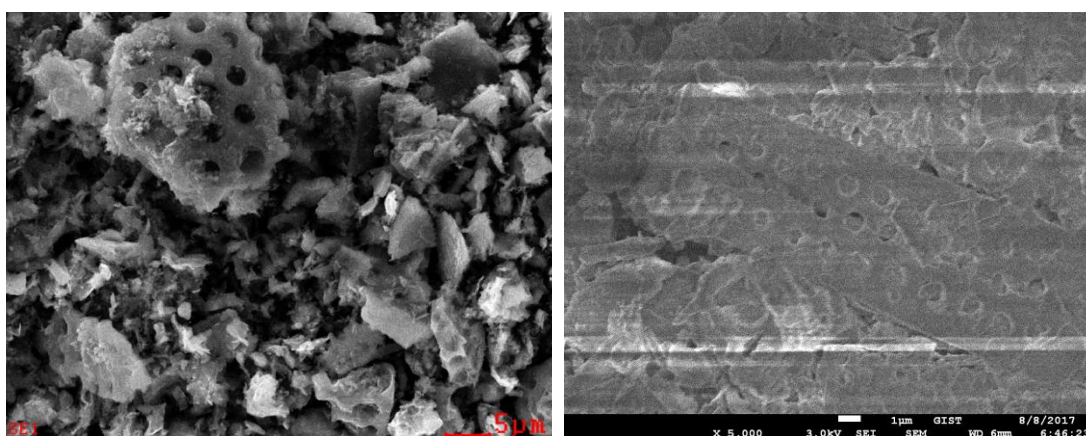
(a)

(b)

a,b – SEM pictures of natural diatomite
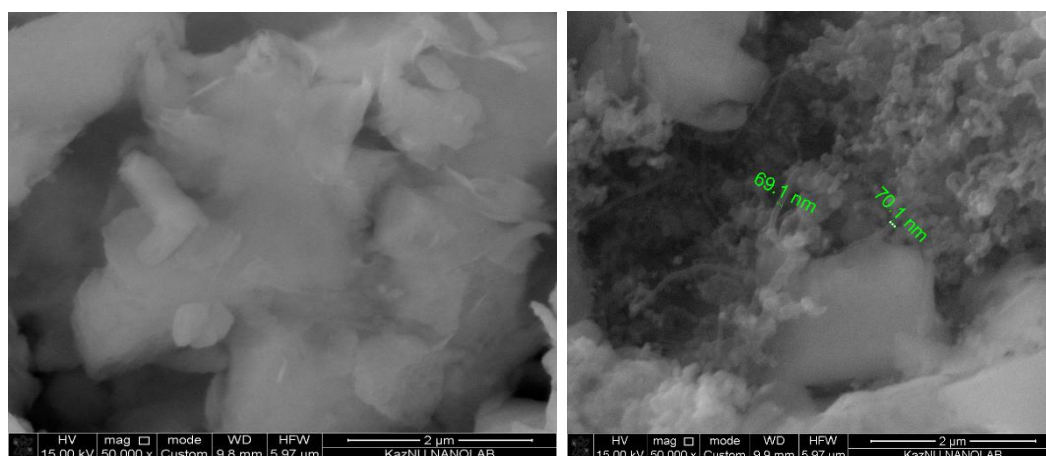
(c) Ni based diatomite substrate with CNTs
Figure 2. SEM images of samples

References

1. M. W. Tibbitt, J. E. Dahlman and R. Langer, J. Am. Chem. Soc., 2016, 138, 704–717.
2. Y. Wang, A. Santos, A. Evdokiou and D. Losic, J. Mater. Chem. B, 2015, 3, 7153–7172.
3. S. Maher, T. Kumeria, Y. Wang, G. Kaur, D. Fathalla, G. Fetih, A. Santos, F. Habib, A. Evdokiou and D. Losic, Adv. Healthcare Mater., 2016, 5, 2667–2678.
4. M. S. Aw, S. Simovic, J. Addai-Mensah and D. Losic, Nanomedicine, 2011, 6, 1159–1173.
5. S. Maher, M. Alsawat, T. Kumeria, D. Fathalla, G. Fetih, A. Santos, F. Habib and D. Losic, Adv. Funct. Mater., 2015, 25, 5107–5116.
6. D. G. Mann, Phycologia, 1999, 38, 437–495.
7. M. De Stefano and L. De Stefano, J. Nanosci. Nanotechnol., 2005, 5, 15–24.
8. D. Losic, J. G. Mitchell and N. H. Voelcker, Adv. Mater., 2009, 21, 2947–2958.

ИССЛЕДОВАНИЯ СВОЙСТВ ИНТЕРМЕТАЛЛИДНЫХ ПОКРЫТИЙ СИСТЕМЫ Al-Cu, Ta-Cd, W-Cd С ЛЕГИРОВАНИЕМ Cr, Ti, Ag, Nb, Mo

И.К. Аблакатов, Ю.Ж.Тулеушев, М.Б. Исмаилов

АО «Национальный центр космических исследований и технологий»,
г. Алматы, ул. Шевченко 15, m.ismailov@spaceres.kz

Были получены и исследованы свойства интерметаллидных покрытий систем Al-Cu, Al-Cu-Cr , Al-Cu-Ti, Al-Cu-Ag, Ta-Cd-Nb, Ta-Cd-Mo, W-Cd-Nb и W-Cd-Mo полученные путем одновременного магнетронного напыления с последующей термообработкой.

В космосе космический аппарат (КА) подвергается к множеством факторов, особенно не равномерно и периодически нагревается лучами Солнце. Для предотвращения перегрева КА на его поверхность наносят специальные терморегулирующие покрытия, которые обеспечивают необходимый температурный режим между КА и окружающим пространством [1-2]. В качестве терморегулирующего покрытия интерес вызывают интерметаллидные покрытия. Интерметаллиды – это устойчивое соединение двух или более металлов между собой и отличаются высокой твердостью, коррозионной стойкостью и электропроводностью [3]. Целью данной работы является синтез интерметаллидных покрытий, полученные путем одновременного напыления компонентов с легированием третьего элемента. Покрытия получали на магнетронной установке с далнейшим отжигом для синтеза с аморфного состояния в интерметаллидное. Фазовый состав, микротвердость, коэффиценты поглащения и излучения, электропроводность и снимки поверхости покрытия определялись соответственно в следующих исследовательских оборудованиях: дифрактометр D8 ADVANCE, микротвердомер ПМТ-3, спектрофотометр UV-3600 (Shimadzu) в диапазоне длин волн 240-2400 нм и пирометр UT302B при длине волны 800-1400 нм, прибор DT830B, электронно-зондовый микроанализатор JSM-8230 (JEOL).

Получены покрытия системы алюминий-медь, легированные добавками титана, хрома и серебра, исследована их структура, проведены инициирующие отжиги для синтеза интерметаллидных фаз, исследована структура полученных фаз после отжига. Для получения прототипов «черного» покрытия получены покрытия системы тантал-кадмий и вольфрам-кадмий, исследована их структура, проведены отжиги для получения покрытий на основе пористых тантала и вольфрама, проведено исследование их структуры, получены покрытия систем тантал-кадмий и вольфрам-кадмий, легированных добавками ниобия и молибдена, получены пористые покрытия на их основе и проведены рентгеноструктурные исследования. Проведенные рентгенографические исследования полученных покрытий до и после отжига 400 $^{\circ}$C позволили установить, что в исходном состоянии после напыления покрытия всех составов являются рентгеноаморфными, а после отжига 400 $^{\circ}$C образуются интерметаллидные фазы $CuAl$ и $CuAl_2$. Получены «черные» покрытия на базе пористых тантала и вольфрама путем создания интерметаллидного покрытия состава $TaCd_3$ и WCd_3 и последующего удаления кадмия в вакууме отжигом при температуре 800 $^{\circ}$C.

Были измерена микротвердость покрытий системы Al-Cu (с добавлением Ti, Ag, Cr) до и после ТО на микротвердомере ПМТ-3 с использованием алмазной пирамидки. Все покрытия имеют толщину в пределах 2 мкм. Была использована нагрузка 3,5 г. Установлено, что у образцов системы Al-Cu с легированием третьего элемента микротвердость

возрастает после ТО. В случае покрытия Al-Cu без легирования микротвердость падает после ТО, а до отжига имеет величину 5135 Мпа, что превосходит твердость многих инструментальных сталей.

Проведены исследования спектрофотометрических характеристик «белых» покрытий на спектрофотометре UV-3600 (Shimadzu). Неотожженное аморфное покрытие в видимой части спектра имеет коэффициент отражения 41%. Коэффициент отражения «белых» покрытий приведены на рисунке 1.
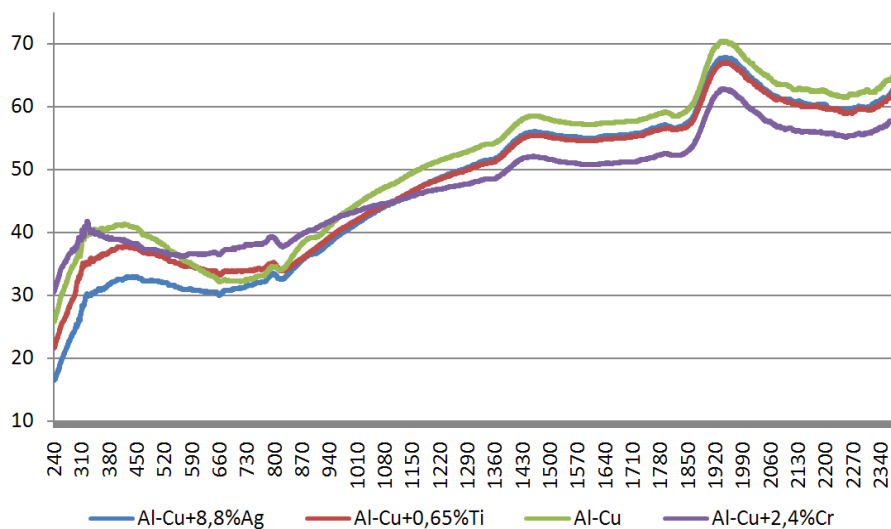

Рисунок 1. Коэффициент отражения «белых» покрытий

Покрытие со сформированной интерметаллидной фазой CuAl в видимой области спектра имеет коэффициент отражения 41 %. Результаты измерения спектрофотометрических характеристик покрытия из интерметаллидной фазы CuAl, легированной добавками серебра, до и после формирующего интерметаллидную фазу отжига показывают, что покрытие в аморфном состоянии имеет в видимой части спектра более высокий коэффициент отражения, чем после отжига. Результаты измерения спектрофотометрических характеристик покрытия из интерметаллидной фазы CuAl, легированной добавками титана, до и после формирующего интерметаллидную фазу отжига позволяют сделать вывод, что в видимой части спектра аморфизованное интерметаллидное покрытие имеет более высокий коэффициент отражения, равный 40 %. Результаты измерения спектрофотометрических характеристик покрытия из интерметаллидной фазы CuAl, легированной добавками хрома, до и после формирующего интерметаллидную фазу отжига дают следующее: из сопоставления кривых коэффициента отражения до и после отжига можно сделать вывод, что аморфизованное интерметаллидное покрытие из интерметаллидной фазы CuAl, легированной добавками хрома во всех интервалах спектра имеет такую же отражательную способность, как и окристаллизованное. Проведенные исследования «черных» покрытий на спектрофотометре UV-3600 показали, что коэффициент отражения этих покрытия изменяется от 5 до 8 %. (минимально – у пористого тантала, легированного ниобием, максимально – у пористого вольфрама без легирующих добавок).

Электронно-микроскопические исследования полученных покрытий систем Ta-Cd и W-Cd, показали, что до отжига покрытия состоят из плотно прижатых друг к другу округлых кристаллитов разной высоты. Коэффициент отражения «черных» покрытий приведены на рисунке 2. После отжига кадмий выпаривается из покрытий и остаются пористые образования из тантала и вольфрама, легированные Nb и Mo. Результаты всех исследований приведены на таблице 1.
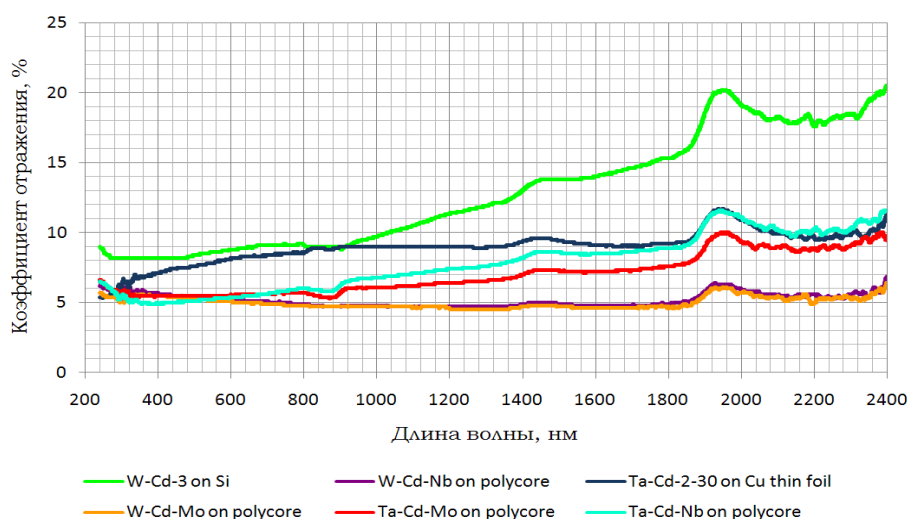
Рисунок 2. Коэффициент отражения «черных» покрытий

Таблица 1. Основные свойства полученных покрытий

№	Система	Образованная фаза		Микротвердость, МПа		Коэф. поглощения (As)		Коэф. излучения (ε)		Пов.сопр., кОм/кв.	
		До ТО	После ТО	До ТО	После ТО	До ТО	После ТО	До ТО	После ТО	До ТО	После ТО
1	Al-Cu-Ti	Аморф	CuAl	3529	4718	0,43	0,35	0,22	0,44	2,6	$3,78 \cdot 10^2$
2	Al-Cu-Ag	Аморф	CuAl, CuAl$_2$	3107	3659	0,33	0,32	0,25	0,42	0,5	$1,86 \cdot 10^2$
3	Al-Cu-Cr	Аморф	CuAl	4106	4240	0,39	0,37	0,22	0,39	1,1	$5,02 \cdot 10^2$
4	Al-Cu	Аморф	CuAl, CuAl$_2$	5135	3919	0,36	0,29	0,20	0,38	4,8	$0,72 \cdot 10^2$
5	W-Cd+Nb	Аморф	W	-	-	-	0,94	0,78	0,89	-	$9,74 \cdot 10^4$
6	W-Cd+Mo	Аморф	W	-	-	-	0,94	0,78	0,87	-	$4,17 \cdot 10^4$
7	Ta-Cd+Nb	Аморф	Ta	-	-	-	0,88	0,80	0,93	-	$3,99 \cdot 10^2$
8	Ta-Cd+Mo	Аморф	Ta	-	-	-	0,90	0,81	0,92	-	$0,12 \cdot 10^3$

Заключение

- Получены образцы «белых» интерметальных покрытий на базе CuAl, легированные Ti, Cr, Ag. Показано, что легирование добавками ухудшает потребительские свойства ТРП.

- Получены образцы «черных» покрытий из пористых тантала и вольфрама, легированных ниобием и молибденом. Показано, что легирование третьим и четвертым компонентом понижает коэффициент отражения.

- Установлено, что полученные ТРП обладают хорошей проводимостью

Литература

1   Новиков Л.С. Модель Космоса. Т. 2: Воздействие космической среды на материалы на оборудования космических аппаратов. – М. : КДУ, 2007. – 1144 с.
2   Королев С.И.. Системы обеспечения теплового режима космических аппаратов // Учебное пособие, СПб, Балтийский гос.тех.университет «Военмех», 2006. - 100 с.

3 Интерметаллиды-Химическая энциклопедия [Электронный ресурс]. http://www.xumuk.ru/encyklopedia/1712.html (дата обращения 25.07.2017)

КАТАЛИТИЧЕСКОЕ ОКИСЛЕНИЕ ТЯЖЕЛЫХ НЕФТЯНЫХ ОСТАТКОВ

Е.А.Акказин, Е.К.Онгарбаев, Е.Тилеуберди, З.А.Мансуров
КазНУ им. аль-Фараби, Институт проблем горения, Erdos.Ongarbaev@kaznu.kz

Изучен химизм процесса каталитического окисления Каражанбасской нефти, ее мазута и мазута Павлодарского нефтехимического завода.

The process of catalytic oxidation of fuel oil black oil refineries of the Republic of Kazakhstan was studied.

В настоящее время существуют различные методы повышения эффективности окисления, в частности, увеличение поверхности контакта фаз за счет совершенствования устройств подачи воздуха, использования диспергаторов воздушного потока. Оптимизация параметров технологического процесса и подбор оптимального состава сырья также оказывают положительное воздействие. Одним из путей совершенствования процесса получения битумов является применение катализаторов окисления и специально вводимых в систему окислителей.

По литературным и предыдущим экспериментальным данным самыми активными оказались и за рубежом в производство внедрены хлорид железа (III) и фосфорная кислота, которые были выбраны в качестве катализатора. Исследовалось влияние этих веществ на процесс окисления Каражанбасской нефти и мазутов НПЗ РК. При этом была сделана попытка оценить химизм каталитического окисления нефти и мазутов для получения битумов.

Суть процесса окисления заключается в увеличении содержания ароматических и кислородсодержащих соединений в битуме, функциональные группы которых вступают в связь с минеральными материалами в составе асфальтобетонных смесей. Для установления химических превращений в составе нефти и ее мазута во время их окисления проводился ИК-спектроскопический анализ Каражанбасской нефти, мазута Павлодарского нефтехимического завода и продуктов их окисления, результаты которого представлены в таблице 1. Наибольшие изменения интенсивностей полос поглощения наблюдаются в интервале 1500-1700 см$^{-1}$, где поглощают ароматические и кислородсодержащие соединения. Поэтому, об изменениях, происходящих при окислении, судили по волновым числам: 720 см$^{-1}$ - маятниковые колебания метиленовых групп -CH_2 в длинных цепях углеводородов; 1600 см$^{-1}$ - валентные колебания ароматических C=C-связей; 1720 см$^{-1}$ - валентные колебания карбонильной группы. По отношениям $K_{C=O}=D_{1720}/D_{720}$ и $K_{C=C}=D_{1600}/D_{720}$ оценивали степень окисленности и ароматичности сырья и продуктов (здесь D - оптическая плотность при соответствующих волновых числах). Сравнивая значения приведенных оптических плотностей $K_{C=C}$ и $K_{C=O}$ для сырья и продуктов его окисления и отношений $K_N^{C=C}/K_{сырье}^{C=C}$ и $K_N^{C=O}/K_{сырье}^{C=O}$, которые показывают во сколько раз увеличивается содержание этих соединений в продуктах окисления по сравнению с исходным сырьем, можно сделать заключение о том, что при переходе от нефти к мазуту количество как ароматических, так и кислородсодержащих соединений изменяется незначительно, тогда как при переходе от